2018-01-01

A New Approach To Multiplanar, Real-Time Simulation Of Physiological Knee Loads And Synthetic Knee Components Augmented By Local Composition Control In Fused Filament Fabrication

Joshua Taylor Green
University of Texas at El Paso, joshtgreen@gmail.com

A NEW APPROACH TO MULTIPLANAR, REAL-TIME SIMULATION OF PHYSIOLOGICAL KNEE LOADS AND SYNTHETIC KNEE COMPONENTS AUGMENTED BY LOCAL COMPOSITION CONTROL IN FUSED FILAMENT FABRICATION

JOSHUA TAYLOR GREEN

Doctoral Program in Materials Science and Engineering

APPROVED:

Roger V. Gonzalez, Ph.D., Chair

Stephen W. Stafford, Ph.D.

C. Brandon Broome, M.D.

Charles Ambler, Ph.D.
Dean of the Graduate School

Dedication

I would like to dedicate this work and pursuit of a doctorate in philosophy to my father, mother, wife, and Lord, Jesus Christ. I am forever grateful to my parents, Donald and Pamela Green, who have supported me in all my endeavors and have instilled in me a great respect for hard work and excellence. My wife, Stephanie Green, has eased life's burdens and greatly enriched it as she has consistently and warmly stood by me. Jesus Christ has redeemed me as only He can, and to Him, I dedicate the entirety of myself – body, mind, and spirit.

A NEW APPROACH TO MULTIPLANAR, REAL-TIME SIMULATION OF PHYSIOLOGICAL KNEE LOADS AND SYNTHETIC KNEE COMPONENTS AUGMENTED BY LOCAL COMPOSITION CONTROL IN FUSED FILAMENT FABRICATION

by

JOSHUA TAYLOR GREEN, B.S.

DISSERTATION

Presented to the Faculty of the Graduate School of

The University of Texas at El Paso

in Partial Fulfillment

of the Requirements

for the Degree of

DOCTOR OF PHILOSOPHY

Department of Metallurgical, Materials and Biomedical Engineering

THE UNIVERSITY OF TEXAS AT EL PASO

December 2018

Acknowledgements

I could not have completed this work without my committee, a group of optimistic, patient, and esteemed professionals. I give my sincere thanks to both Dr. Stephen W. Stafford and Dr. C. Brandon Broome, who have been welcoming and encouraging while guiding me into their fields of expertise. I am especially grateful for my supervisor, Dr. Roger V. Gonzalez, who, with his trust and guidance for many years, has given me a great opportunity to participate in a successful and promising professional path.

I am thankful to my colleagues: Rena Hale, Addison Wood, Paul Power, Jonathan Slager, Ángel Torrado, Mauricio Lopez, Edel Arrieta, and Stephen Wilson. I have greatly benefited from their intellectual contributions and collaborative support. I admire their hard work and dedication to authentically contribute to their respective fields.

I would also like to thank the many undergraduate students who have touched this project and its various aspects: Xavier Villareal, Herman Cordero, Crystal Barrera, Daniel O'brien, Jad Aboud, Scott Wilkins, and many more. Thank you all for your long hours and your willingness to learn alongside me. It has been an honor to share this experience with you and continue the tradition of academic mentorship that has made me who I am today.

Funding for this work was provided by NSF grant BES 0966398, The University of Texas STARS Funding, and ADVANCED Motion Controls University Outreach Program.

Abstract

Despite numerous advances in biomedical engineering, few developments in surgical simulation have been made outside of computational models. Cadavers remain the primary media on which surgical research and simulation is conducted. Most attempts to quantify the effects of orthopedic surgical methods fail to achieve statistical significance due to limited quantities of cadaver specimen, large variations among the cadaver population, and a lack of repeatability among measurement techniques. The general purpose of the research covered in this dissertation is to develop repeatable simulation of physiological loads and develop techniques to fabricate a synthetic-based replacement of cadaver specimens. Future work applying this study's methods and technology is expected to produce a synthetic human joint that can assist in isolating the effects of surgical techniques by supporting repeatable measurement and response to physiological loads.

This dissertation consists of three aims that collectively provide novel advancements in biomechanics, rapid prototyping, and materials science. Aim 1 of this dissertation is the development of the University of Texas Joint Load Simulator (UTJLS), which can apply physiological loads with synchronous application of ground reaction forces, joint kinematics, and muscle forces. Aim 2 advances technology and methods for Local Composition Control (LCC) in Fused Filament Fabrication (FFF) and investigates the viability of commercially available filaments for application as synthetic tissue. Aim 3 produced a synthetic femoral anterior cruciate ligament (ACL) tibial complex (FATC) using aim 2's techniques and characterized its mechanical response to tensile loads applied in two different directions.

Aim 1 includes a description of the design, configuration, capabilities, accuracy, and repeatability of the UTJLS during physiological loads applied to four cadaver knee specimens. The UTJLS is a musculoskeletal simulator consisting of two robotic manipulators and eight musculotendon actuators. Sensors include eight tension load cells, two force/torque systems, nine absolute encoders, and eight incremental encoders. A custom control system determines command output for position, force, and hybrid control and collects data at 2000 Hz. Controller configuration

performed forward-dynamic control for all knee degrees of freedom except knee flexion. Actuator placement and specimen potting techniques uniquely replicate muscle paths. Real-time tests included 47 heel and toe squat maneuvers with and without musculotendon forces. Accuracy and repeatability standard deviations across specimen during squat simulations were equal or less than 8 N and 5 N for musculotendon actuators, 30 N and 13 N for ground reaction forces, and 4.4 N m and 1.9 N m for ground reaction moments. The UTJLS is the first of its design type. Controller flexibility and physical design supports axis constraints to match traditional testing rigs, absolute motion, and synchronous real-time simulation of multiplanar kinematics, ground reaction forces, and musculotendon forces. System degrees of freedom, range of motion, and speed support future testing of faster maneuvers, various joints, and kinetic chains of two connected joints.

In pursuit of Aim 2, a series of FFF printers with a hotend containing an actuated element for LCC were developed. Printing functions were supported by custom software, custom slicer configurations, and custom firmware. Aim 2 not only provided the means of fabricating synthetic tissue but also provided insight into synthetic tissue design. Eight blends of high-temperature polylactic acid (HTPLA) and Ninjaflex® (NF), a thermoplastic elastomer, were characterized through standard D638 tensile tests and custom interface bond strength tests. Tests determined material properties including modulus of elasticity (E), Poisson's ratio, yield stress (σ_Y), percent elongation at yield ($EL\%_Y$), ultimate tensile stress (UTS), and percent elongation at failure ($EL\%_F$). Ranges of material properties for E, σ_Y, and UTS were 17.3 to 3483 MPa, 0.53 to 52.0 MPa, and 23.7 to 66.8 MPa respectively. These compositions encompass a wide range of material stiffness overlapping the reported stiffness of biological tissues including trabecular bone, subchondral bone, tendon, ligaments, and some articular cartilage. Results from these tests provide insight into synthetic tissue design by informing the designer of the synthetic materials properties from which tissue composition can be selected. Bond strength tests revealed potential increases in synthetic tissue strength by providing insight into the benefits of including functional gradients in the tissue design. When comparing a binary interface between the softest and hardest material to a configuration of seven incremental interfaces, σ_{IBS} is expected to effectively increase by 25% to

95%. Strength of such an interface may be further increased by relief of stress concentrators due to incremental changes in stiffness.

Aim 3 tested the methods of aim 2 for synthetic tissue design and fabrication. A series of synthetic knee designs were developed from magnetic resonance images (MRI) of a single human left knee. A model of an FATC with functional gradients at the ACL's insertion sites was developed and configured for tensile testing along the Tibia's mechanical axis and the ACL's anatomical axis. A method for designing and implementing soluble and insoluble support structures was developed to support fabrication. The ACL component of printed specimen were assigned a composition of 22% HTPLA and 78% NF, which was shown in aim 2 to have an E equal to 290 MPa. Synthetic FATC stiffness and ultimate load ranged between 265 to 330 N and 41 to 70.5 N/mm, respectively. The largest stiffness and ultimate load of FATC specimen during tensile tests was no more than 39% and 50% of what was reported during *in vitro* tests with identical loading conditions respectively. Failure of these specimen to perform closer to the corresponding biological system was primarily attributed to anisotropy and bending loads introduced by tensile load direction and knee flexion. The methods of aim 2 provide numerous opportunities to improve upon these results through design modification utilizing the mixing printer's control over geometry and local composition.

Table of Contents

List of Tables

List of Figures

Chapter 1: Introduction

Despite numerous advances in biomedical engineering, few developments in surgical simulation have been made outside of computational models. Cadavers remain the primary media on which surgical research and simulation is conducted. Existing synthetic knees fail to mechanically respond as cadaveric knee specimens, and as such, they are not effective for investigation of human biomechanics, quantification of orthopedic surgical methods, or controller optimization for joint load simulators. Nonetheless, cadaver knee specimens also have their own limitations including availability and variance among geometry and mechanical properties. Most attempts to quantify the effects of orthopedic surgical methods fail to achieve statistical significance due to limited quantities of cadaver specimen, large variations among the cadaver population, and a lack of repeatability among measurement techniques. In contrast, a synthetic knee could provide repeatable results more closely emulating knee biomechanics including the effects of even minor alterations such as variation of surgical procedures or changes in geometry and material properties. Introduction of such a means of quantifying joint kinetics and kinematics is likely to not only revolutionize research methods but also how orthopedic surgeons are trained.

The primary purpose of this study is the development of methods and techniques to support development of such a synthetic knee. Three specific aims were selected to provide novel advancements in biomechanics, rapid prototyping, and materials science that are necessary to support these aims. Aim 1 of this dissertation is the development of The University of Texas Joint Load Simulator (UTJLS), which can apply physiological loads with synchronous application of ground reaction forces, joint kinematics, and muscle forces. Aim 2 advances technology and methods for local composition control (LCC) in fused filament fabrication (FFF) and investigates the viability of commercially available filaments for application as synthetic tissue. Aim 3 produced a synthetic femoral anterior cruciate ligament (ACL) tibial complex (FATC) using aim 2's techniques and characterized its mechanical response to tensile loads applied in two different directions.

Aim 1 developed and characterized the UTJLS, which is a musculoskeletal simulator capable of repeatable and accurate simulation of physiological loads. Included in the design are numerous sensors, actuators, and a custom control system for position, force, and hybrid control. Unique control of musculotendon force includes actuator placement to simulate muscle origins and specimen potting techniques that allow muscle paths to follow near to a specimen's bone. Real-time tests including 47 heel and toe squat maneuvers with and without musculotendon forces were applied to determine simulator accuracy and repeatability. The UTJLS is the first of its design type. Its controller and physical design allow for axes to be constrained to match traditional testing rigs, to follow kinematics in absolute motion, and perform synchronous real-time simulation of multiplanar kinematics, ground reaction forces, and musculotendon forces. System degrees of freedom, range of motion, and speed support future testing of faster maneuvers, various joints, and kinetic chains of two connected joints and can be used to test both cadavers and synthetic knees with the same load profiles.

Aim 2 not only provided the means of fabricating synthetic tissue but also provides insight into synthetic tissue design by providing tensile properties of materials produced by this technique. Eight blends of high-temperature polylactic acid (HTPLA) and Ninjaflex® (NF), a thermoplastic elastomer, were characterized through standard D638 tensile tests and custom interface bond strength tests. Results from these tests provide insight into synthetic tissue design by providing properties of synthetic materials by which an informed selection of composition can be made. Bond strength tests revealed potential increases in synthetic tissue strength by providing insight into the benefits of including functional gradients in the design.

Aim 3 tested the methods of aim 2 for synthetic tissue design and fabrication. A series of synthetic knee designs were developed from MRI of a single human left knee. A model of an FATC with functional gradients at the ACL's insertion sites was developed and configured for tensile testing along the tibia's mechanical axis and the ACL's anatomical axis. A method for designing and implementing soluble and insoluble support structures was developed to support fabrication. The synthetic FATC specimens deviated from the reported properties of their

biological counterparts and appeared to underperform the tensile test results of aim 2. Potential sources of these variations were discussed include bending loads, anisotropy, and printer defects.

Chapter 2: Objectives

This dissertation addresses the following three aims:

AIM 1: Advance the state-of-the-art of musculoskeletal joint-load simulators to recreate physiological loading through synchronous application of joint kinematics, ground reaction forces, and tendon forces in real time.

AIM 2: Broaden characterization of LCC in FFF using a custom hotend with an actuated element to fabricate tensile specimen of blended compositions for mechanical testing composed of blended filaments.

AIM 3: Investigate use of methods from aim 2 for printing synthetic tissue. Test a synthetic FATC following the methods described by Woo et al., 1991 and provide a comparison between synthetic and biological results.

2.1 Specific Aim 1

The simulator developed in support of aim 1 is known as the UTJLS and has demonstrated synchronous control of joint kinematics, ground reaction forces, and musculotendon forces in real-time during *in vitro*, squat maneuver testing. The UTJLS consists of two robotic manipulators with eight musculotendon actuators and utilizes eight tension load cells, two force/torque systems, nine absolute encoders, eight incremental encoders, and a custom control system operating at 2000 Hz. Having a unique design type, the UTJLS is the first in vitro joint simulator capable of absolute motion and has a uniquely flexible architecture capable of adjusting control schemes to mimic other simulator designs (e.g. oxford rig or robotic arm). Another unique advantage is the layout of the musculotendon actuators which, in combination with a novel method for specimen alignment and casting, provide anatomical muscle paths.

2.2 Specific Aim 2

Due to the complexity of human tissue, traditional manufacturing methods are not readily suitable for synthetic knee development. Rather, LCC is necessary to mimic the various tissues within the knee joint to promote strong interfacial strength between dissimilar materials. The only

fabrication method capable of such control is additive manufacturing (AM) – commonly known as 3D printing. For this reason, a series of custom mixing printers were developed to blend flexible and rigid thermoplastic filament and provide a range of available mechanical properties during printing. Eight compositions were formed by blending filament during tensile specimen printing, which underwent tensile testing following D638 standards. Specialized tensile specimens were printed with a curved, bi-material interface to determine interface strength between compositions. Specimen that failed underwent failure analysis to determine suitability as synthetic tissue.

2.3 Specific Aim 3

Aim 3 tested the methods of aim 2 for synthetic tissue design and fabrication. A detailed design is necessary for synthetic knee fabrication. A series of synthetic knee designs were developed from MRIs of a single human left knee. A model of an FATC with functional gradients at the ACL's insertion sites was developed and configured for tensile testing along the tibia's mechanical axis and the ACL's anatomical axis. A method for designing and implementing soluble and insoluble support structures was developed to support fabrication. The synthetic FATC specimens deviated from the reported properties of their biological counterparts and appeared to underperform the tensile test results of aim 2. Potential sources of these variations were discussed include bending loads, anisotropy, and printer defects.

Chapter 3: Aim 1 - In Vitro Joint Load Simulation through Development of a Reconfigurable Multiplanar Simulator

The content of this chapter was published in the Journal of Biomechanical Engineering by Green et al. (Green et al. 2017). Additional information related to the squat studies described here have been published in the Journal of Biomechanics by Hale et al. (Hale et al. 2018).

3.1 Introduction

Joint diseases and disorders, either due to aging or injury, are among the most prevalent, debilitating, and painful medical conditions (Neogi 2013; Bagge et al. 1992; Gillam et al. 2013; Mills et al. 2013; Suri et al. 2010; Hortobágyi et al. 2005). Although tremendous advances have been made in biomedical engineering, potential breakthroughs are hindered by limitations in acquiring reliable *in vivo* measurements such as joint contact forces and soft tissue deformations (Lanyon et al. 1975; Burr et al. 1996). Although hip and knee joint contact forces have been measured using instrumented implants (Bergmann et al. 2014; Arami et al. 2011; S. J. G. Taylor et al. 1998), these devices are typically implanted in older patients; and the motions collected are limited to relatively slow motions such as gait, stair climbing, and slow jogging. In addition, the behavior may not be representative of what happens in a native joint since geometries and material properties have been altered.

To circumvent these significant barriers related to *in vivo* studies, investigators have developed computational models and *in vitro* simulators, the latter to perform measurements on cadaveric specimens. Computational models are very versatile since virtually any type of tissue can be simulated, in parallel to applying a variety of kinematic and kinetic conditions. The main drawback of predictive computational modeling is the need for thorough validation, which in turn relies on experimental measurements. Bates et al. has identified 77 ACL-related *in vitro* studies from 2004-2013, which may be categorized as robotic or mechanical-impact tests (Bates, Myer, et al. 2015).

Numerous robotic simulators (Leichtle et al. 2014; Goldsmith et al. 2014; Durairaj, Sivasankar, and Krishnamoorthy 2014; Cassidy et al. 2013; Becke and Schlegl 2011; Noble et al. 2010; S. L. Woo et al. 1991; Anderson et al. 2009; Howard et al. 2007) have been developed to replicate the complexity of *in vivo* joint biomechanics. Many simulations are static or quasi-static (Leichtle et al. 2014; Goldsmith et al. 2014; Durairaj, Sivasankar, and Krishnamoorthy 2014; S. L.-Y. Woo and Fisher 2009; Fujie, Sekito, and Orita 2004), but some have applied time-varying kinetics and kinematics to more accurately apply physiological loading conditions (Cassidy et al. 2013; Becke and Schlegl 2011; Bates, Nesbitt, et al. 2015; Noble et al. 2010; Anderson et al. 2009; Howard et al. 2007; Maletsky and Hillberry 2005b). The physiological accuracy of *in vitro* testing is dependent upon numerous factors. Critical to recreating *in vivo* conditions is the synchronous application of multiplanar joint kinematics, external forces (*e.g.* ground reaction forces), and musculotendon forces. In addition to obtaining realistic joint loading conditions, accurate muscle moment arms must also be replicated.

In particular, musculotendon force control varies tremendously between existing *in vitro* simulators: nonexistent musculotendon loading (Goldsmith et al. 2014; Durairaj, Sivasankar, and Krishnamoorthy 2014; Becke and Schlegl 2011; S. L.-Y. Woo and Fisher 2009; Howard et al. 2007; Fujie, Sekito, and Orita 2004), grouped knee flexor and extensor musculotendon loading (Cassidy et al. 2013; Anderson et al. 2009; Maletsky and Hillberry 2005b), and individual musculotendon force control (Leichtle et al. 2014; Noble et al. 2010; Dunning et al. 2003). Since each individual musculotendon crossing a specific joint uniquely contributes to its stability and therefore internal loading condition (Wünschel et al. 2011), grouping individual muscle forces or failing to represent muscle forces altogether can negatively influence the joint kinematics and introduce measurement errors regarding contact forces, ligament strains, and relative joint movement. Musculotendon force application is also affected by muscle moment arms. Since joint kinematics are governed by optimized muscle forces balanced between agonist and antagonist muscles, differences in muscle moment arms will alter these precisely tuned loading patterns and thus any further measurements performed.

Few simulators attempt to apply multiplanar kinematics and kinetics. Full constraint of a single joint requires control of six degrees of freedom (DOF), where a knee consists of a tibiofemoral and a patellofemoral joint. Many simulators limit control to sagittal DOF's (Leichtle et al. 2014; Durairaj, Sivasankar, and Krishnamoorthy 2014; Cassidy et al. 2013; Anderson et al. 2009) and do not fully constrain tibiofemoral DOF's as demonstrated by other simulators (Goldsmith et al. 2014; Becke and Schlegl 2011; Noble et al. 2010; S. L.-Y. Woo and Fisher 2009; Howard et al. 2007; Fujie, Sekito, and Orita 2004; Bates, Nesbitt, et al. 2015).

Bates et al. identified another limitation among *in vitro* simulators. Current methods of reproducing high strain rate loads lack accurate and repeatable control (Bates, Myer, et al. 2015). The recommended solution to this problem is highly-dynamic load introduced through precise robotic manipulation. Cassidy et al. demonstrated high-speed loading but only did so with sagittal DOF's and grouped muscles(Cassidy et al. 2013).

To address the current limitations of existing *in vitro* simulators with the aim of providing improved physiological experimental data, we sought to develop a versatile *in vitro* multi-joint simulator capable of replicating highly-dynamic activities such as running, jump landing, and cutting. As a critical step towards this goal, this chapter introduces the UTJLS and includes an outline of the design, a demonstration of its current configuration, and an assessment of its accuracy and repeatability during real-time squat simulations. From this thorough assessment of simulator performance, opportunities are identified for continued advancements toward simulation of highly-dynamic physiological loads, variable-joints, and kinetic chain testing.

3.2 Methods

A custom, multi-plane simulator was developed with the range of motion (ROM) and component specifications to support variable-joint and kinetic chain testing at high-speeds. The associated controller functions on a real-time operating system and is reconfigurable to support a wide ROM and a variety of human joints. The performance evaluation provided in this study determined the standard deviations of controller accuracy across four specimens during four squat

loading conditions, trial repeatability across four specimen, and specimen repeatability for repeated loading of the same maneuver on the same specimen.

3.2.1 Component Design

UTJLS requirements were determined through analysis of lower extremity kinematics and kinetics during highly-dynamic maneuvers including cutting, braking, and drop jumping. These maneuvers are of clinical relevance as they commonly lead to injury and account for some of the highest accelerations and forces occurring in the human body. Subject kinematic and kinetic data for this analysis was collected during preliminary tests using in-house motion capture and verified through literature (Bates et al. 2013; Wang 2011; Stiles et al. 2011).

Two 6-DOF manipulators were designed into the UTJLS, but the three translations of the lower gantry system were not implemented for this particular study (*Figure 3.1a*). For our knee study and for validation with literature, the UTJLS manipulators were configured as surrogate hip and ankle joints, accommodating a full-length lower-limb. Components of the simulator include various servomotor types (*Table 3.1*), tension load cells (*Table 3.2*), multi-axis load cells (*Table 3.3*), encoders (*Table 3.4*), control computers, data acquisition boards, supplementary electronics, and a custom specimen-mounting fixture.

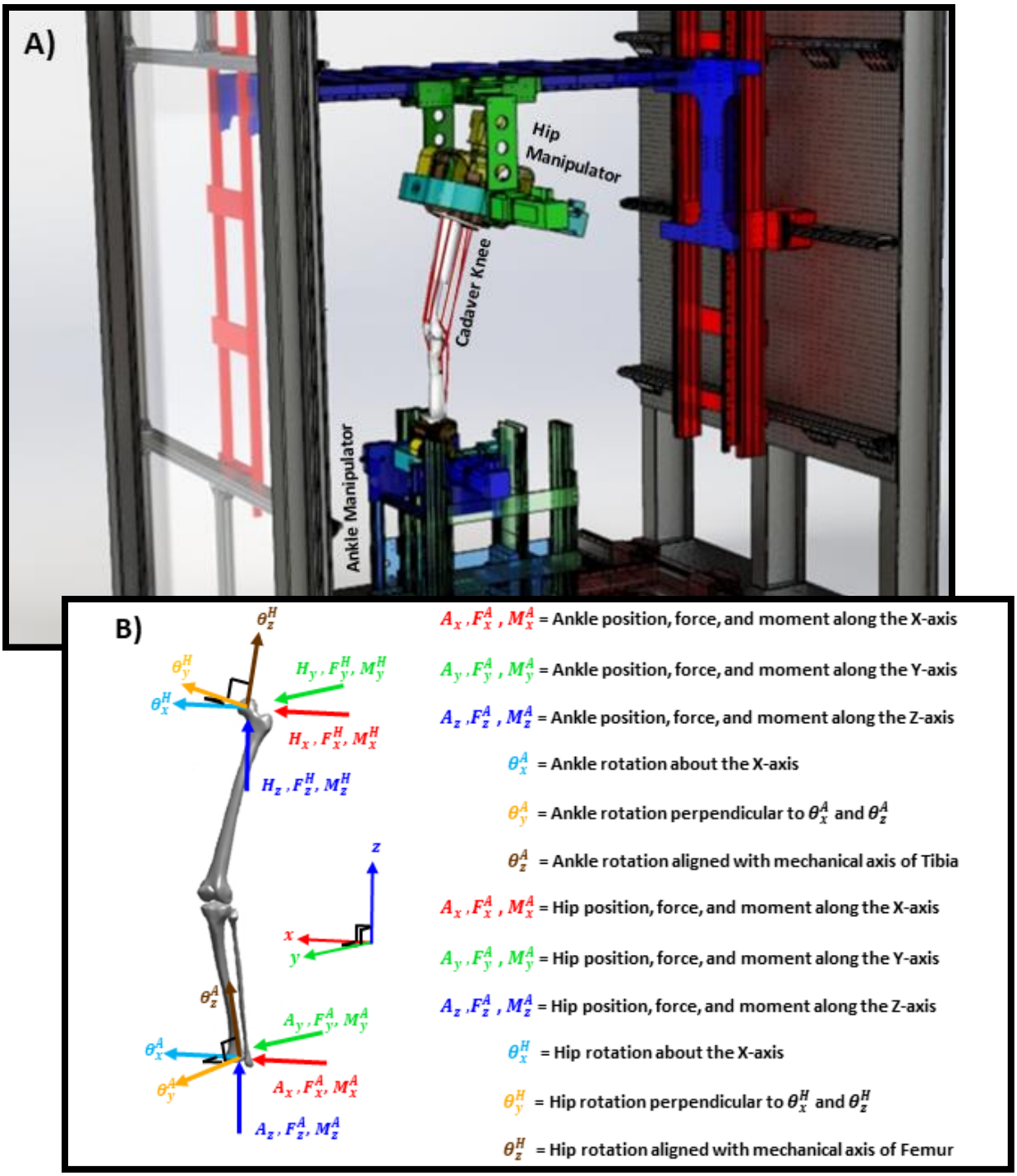

Figure 3.1: (A) Computer rendering of the UTJLS. Transparent components of the lower gantry system have been designed and manufactured but were not implemented for this study. (B) Diagram identifies UTJLS variables and corresponding orientations relative to knee specimen and UTJLS coordinate system. Colors of axes correspond to component colors in (A).

Table 3.1: Simulator Characteristics

Axis	Nearest Anatomical Axis	Range of Motion	Load Capacity	Maximum Velocity	Maximum Acceleration	Servomotor Model	Gearbox Model // Reduction Ratio
Hx	Femur A/P	1000 mm	8194 N	5.99 m/s	21.7 m/s^2	R10-3[b]	[c]
Hy	Femur M/L	1100 mm	5462 N	5.99 m/s	55.4 m/s^2	R10-2[b]	[c]
Hz	Femur D/P	1250 mm	8194 N	5.99 m/s	37.7 m/s^2	R10-3[b]	[c]
θx^H	Femur FE	-30°, +110°	1030 N m	418 deg/s	260 rad/s^2	MPP1003D	AB115 // 60:1
θy^H	Femur Ad/Ab	+28°, -28°	780 N m	330 deg/s	350 rad/s^2	MPP0922D	AB090 // 90:1
θz^H	Femur IE	+40°, -40°	780 N m	330 deg/s	690 rad/s^2	MPP0922D	AB090 // 90:1
θx^A	Tibia FE	+113°, -55°	434 N m	594 deg/s	460 rad/s^2	MPP0922D	AB090 // 50:1
θy^A	Tibia Ad/Ab	+41°, -41°	307 N m	460 deg/s	110 rad/s^2	MPP0921C	AB060 // 70:1
θz^A	Tibia IE	+40°, -40°	307 N m	460 deg/s	780 rad/s^2	MPP0921C	AB060 // 70:1
M1	VM	300 mm	495 N[a]	0.69 m/s	[d]	BE231G	AB042 // 15:1
M2	VL	300 mm	810 N[a]	0.69 m/s	[d]	BE232F	AB042 // 15:1
M3	RF	300 mm	1185 N[a]	0.69 m/s	[d]	BE233F	AB042 // 15:1
M4	BF	300 mm	495 N[a]	0.35 m/s	[d]	BE163F	AB042 // 30:1
M5	SM	300 mm	630 N[a]	0.35 m/s	[d]	BE164F	AB042 // 30:1
M6	ST	300 mm	165 N[a]	1.04 m/s	[d]	BE163F	AB042 // 10:1
M7	GM	300 mm	338 N[a]	0.23 m/s	[d]	BE161F	AB042 // 45:1
M8	GL	300 mm	743 N[a]	0.23 m/s	[d]	BE163F	AB042 // 45:1

[a] Maximum load based on continuous motor torque
[b] Quantity of two
[c] Direct drive
[d] Undetermined

Table 3.2: Miniature load cell specifications

Model	Range	Resolution[a]	Accuracy
XFTC321 - 500N	500 N	0.015 N	3.6 N
XFTC321 - 01KN	1000 N	0.031 N	7.1 N
XFTC321 - 02KN	2000 N	0.061 N	14.2 N

[a] Analog signal converted within UTJLS data acquisition system

Linear Actuators

The current configuration applies relative linear motion through the hip gantry system. The required ROM's were determined through compiling the maximum displacements of a subject's hip during the foot-to-floor contact phases of the previously mentioned maneuvers. Each of the three translation axes utilize two linear servo motors (RIPPED series, Parker Hannifin Corp., Cleveland, OH)) guided by linear bearings (*Table 3.1*). These motors have a high power-density, an electrical time constant of 3 ms, and no backlash. This selection provides the capacity and loading rate that is necessary to follow real-time position and force profiles.

For the purpose of safety, each axis is equipped with emergency stops (SNALD, Enertrols U.S.A, Farmington Hills, MI) that can be positioned to limit system ROM and is equipped pneumatic brakes (RB15, Nexen Group, Inc., Vadnais Heights, MN) operated by 3-way solenoid valves (S8, Pneumadyne, Inc., Plymouth, MN). Both the brakes and solenoid valves are spring loaded and engage in less than 0.12 s.

Table 3.3: Multi-axis load cell characteristics

	Omega 160			Custom Load Cell System		
Axis	Range	Resolution	Accuracy	Range	Resolution[a]	Accuracy
Fx	2500 N	0.25 N	31.3 N	4000 N	0.49 N	22.9 N[b]
Fy	2500 N	0.25 N	31.3 N	4000 N	0.49 N	22.9 N[b]
Fz	6250 N	0.75 N	93.8 N	4000 N	0.49 N	22.9 N[b]
Mx	400 N m	0.05 N m	4 N m	610 N m	0.074 N m	3.5 N m[c]
My	400 N m	0.05 N m	5 N m	842 N m	0.103 N m	4.8 N m[c]
Mz	400 N m	0.05 N m	5 N m	1378 N m	0.168 N m	7.9 N m[c]

[a] Analog signal converted within UTJLS data acquisition system
[b] Calculated with law of propagation of uncertainty (BIPM 2008)

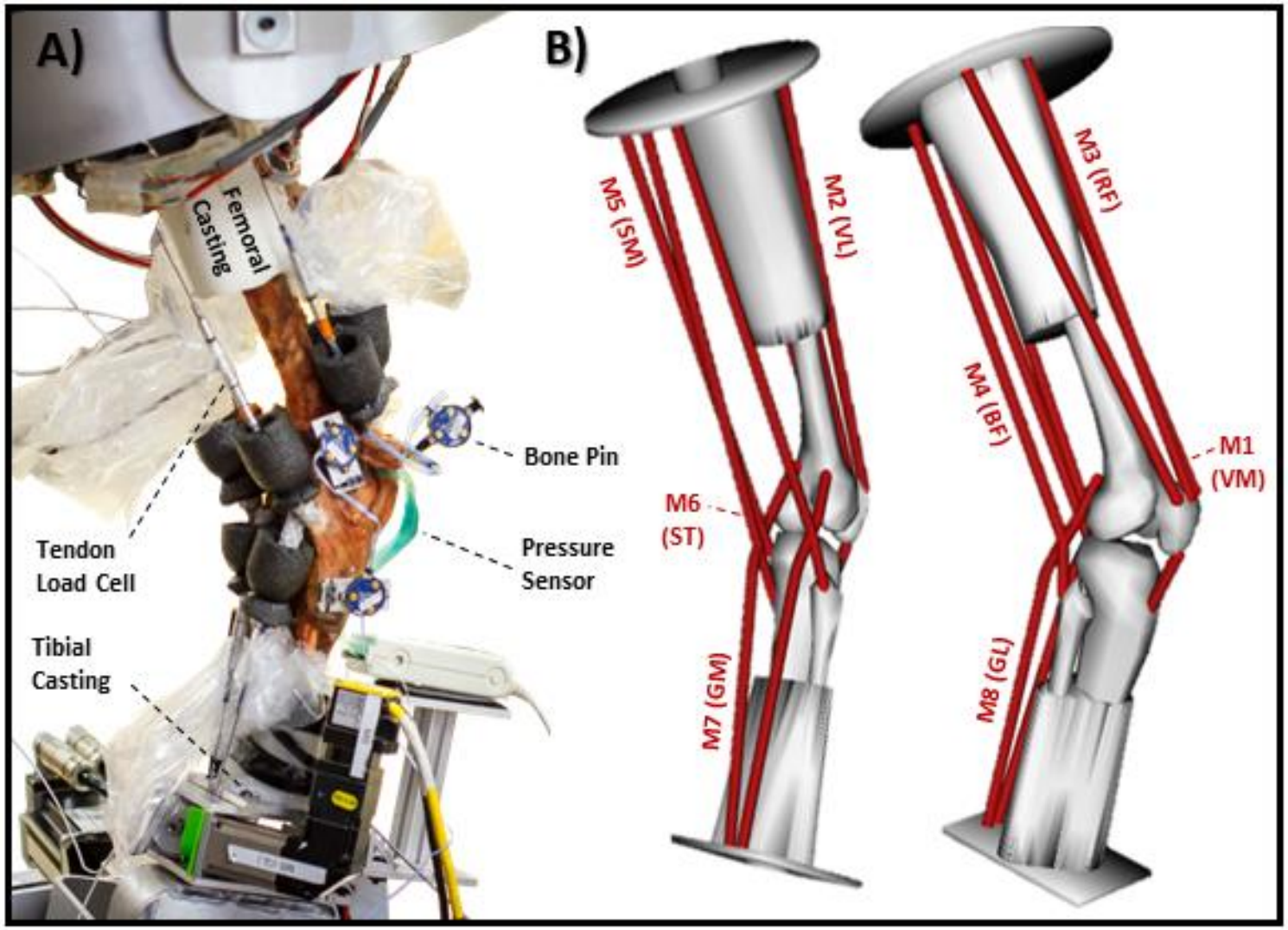

Figure 3.2: (A) Instrumented knee specimen mounted in the UTJLS. Tension load cells are covered in a protective plastic cover, and tendon connections are wrapped in black pipe insulation to assist with freezing. (B) Illustration of musculotendon paths including bone orientation, custom casting molds, and UTJLS interfacing brackets.

Rotational Actuators

Each manipulator contains three rotational axes mounted in series with one another. The upper rotations are mounted on a gantry system, while the lower rotations are mounted on a steel stand centered in the upper manipulators' horizontal ROM (*Figure 3.1a*). Each rotational axis is driven by a servo motor (MPP series, Parker Hannifan Corp., Cleveland, OH) driving a gearbox (AB series, Apex Dynamics, Ronkonkoma, NY) (*Table 3.1*). On each manipulator, the outermost rotation is oriented along the simulator's X-axis with the innermost rotation aligned with the respective bone's mechanical axis (*Figure 3.1*).

Musculotendon Actuators

Accurate application of joint moments from musculotendon forces requires both accurate force magnitude and moment arms, which are dependent upon multiple factors including insertion sites and muscle path (Webb, Blemker, and Delp 2014). To retain anatomical insertion sites, musculotendon actuators are connected directly to the cadaver tendon. In the case of a knee joint, while muscle insertions on the femur, tibia, and fibula are specimen-specific, surrogate muscle insertions on the pelvis and calcaneus are simulator-specific, *i.e.* determined by musculotendon actuator placement and steel cable guides. To represent accurate anatomical muscle insertions, the mounting location of each actuator was derived from previously published 3D models (*Figure 3.2*) (Hausselle et al. 2012).

The UTJLS has eight musculotendon actuators configured to replicate the following muscles: vastus medialis (VM), vastus lateralis (VL), rectus femoris (RF), semitendinosus (ST), semimembranosus (SM), biceps femoris (BF), and medial and lateral gastrocnemius (GM and GL). These actuators consist of servo motors (BE series, Parker Hannifan Corp., Cleveland, OH) and gearboxes (AB042, Apex Dynamics, Ronkonkoma, NY) and are connected to pulleys with steel cables providing a linear ROM of 300 mm (*Table 3.1*).

Table 3.4: Optional feedback sources and control scheme for squat maneuvers

	Feedback device		
Axis	Position	Force	Control Mode
Hx	EMAX 2 encoder	Fx^A of custom GRF load cell	Hybrid[b]
Hy	LMA10 encoder	Fy^A of custom GRF load cell	Hybrid[b]
Hz	EMAX 2 encoder	Fz^A of custom GRF load cell	Hybrid[b]
θx^H	EQI 1331	Mx^H of Omega160	Position
θy^H	EQI 1331	My^H of Omega160	Position
θz^H	EQI 1331	Mz^H of Omega160	Position
θx^A	EQI 1331	Mx^A of custom GRF load cell	Position
θy^A	EQI 1331	My^A of custom GRF load cell	Hybrid[b]
θz^A	EQI 1331	Mz^A of custom GRF load cell	Hybrid[b]
M1	[a]	XFTC321 - 01KN	Force
M2	[a]	XFTC321 - 01KN	Force
M3	[a]	XFTC321 - 02KN	Force
M4	[a]	XFTC321 - 500N	Force
M5	[a]	XFTC321 - 500N	Force
M6	[a]	XFTC321 - 500N	Excluded
M7	[a]	XFTC321 - 500N	Force
M8	[a]	XFTC321 - 01KN	Force

[a] 2000-line incremental encoder to be integrated as a future feedback source
[b] Hybrid control is tuned for force response

Sensors

Various sensors have been implemented in the design of the UTJLS to measure forces and positions (*Table 3.4*). Musculotendon forces are measured with tension load cells (XFTC321, Measurement Specialties, Hampton, VA), which are connected at the point of each tendon's attachment (*Table 3.2*) (*Figure 3.2a*). This sensor placement prevents measurement error due to friction in cable guides, and the 10 mm diameter of the tension load cells allows for the musculotendon line-of-action to route adjacent to bones without collision.

The rotations of the lower manipulator are mounted on spherical bearings connected to four three-axis load cells (3A120, Interface Inc., Scottsdale, AZ) (range: 0-1000 N, accuracy: 0.3 % full scale, FS, repeatability: 0.1 % rated output, RO) (*Table 3.3*) (*Figure 3.1a*). Each three-axis load cell is mounted equidistant from the ankle's center of rotation, which provides moment arms used for moment measurement. Through use of this custom design, the range of vertical force and x-moment measurement is configured for simultaneous, highly-dynamic loading.

A six-axis load cell (Omega160, ATI Industrial Automation, Apex, NC) is attached to the hip manipulator to measure hip forces and moments (*Table 3.3*). It is located at the center of rotation of the simulated hip with the superior musculotendon actuator system located on the measurement side of the load cell, which prevents musculotendon forces from being included in the measurement (*Table 3.4*) (*Figure 3.1a*).

All rotations and linear axes are equipped with absolute encoders. Linear axes, Hx and Hz, are equipped with the same model absolute encoders (EMAX 2, ELGO Electronic, Inc., Chicago, IL) (maximum speed: 4 m/s, resolution: 0.01 mm, accuracy: 0.186 mm), and the Hy linear axis is equipped with another model absolute encoder (LMA10, Renishaw Inc., Hoffman Estates, IL) (maximum speed: 14 m/s, resolution: 7.8 μm, accuracy: 0.06 mm). All six MPP servomotors are equipped with an internal absolute encoder (EQI 1331, Heidenhain Corp., Schaumburg, IL).

Controller and Data Acquisition

Two computers, a host computer and a real-time control computer, have been included to support the custom UTJLS software developed in LabVIEW™ version 2014 SP1 (National Instruments, Austin, TX). The host computer provides a user interface, whereas the real-time control computer operates using a LabVIEW™ real-time operating system. Control computation and data collection is performed by the real-time computer with support from a data acquisition chassis (NI PXI-1036, National Instruments, Austin, TX) including a field-programmable gate array (NI PXI-7811R, National Instruments, Austin, TX). This configuration provides the computing power to operate the UTJLS in real-time with a controller loop speed of 2000 Hz.

Electronic Hardware

All actuators run off drivers configured for current control. Rotational motors are driven by analog brushless drives providing trapezoidal commutation through hall state feedback (BE series, Advanced Motion Controls, Camarillo, CA), and linear motors are driven by digital drives providing sinusoidal commutation through combined encoder and hall state feedback (DP Series, ADVANCED Motion Controls, Camarillo, CA). All drives receive commands from the UTJLS controller through analog signals.

Custom low voltage hardware has been included on printed circuit boards to assist in data acquisition and interfacing between equipment. Functions served by this equipment include analog signal amplification, low-pass filtering, differential to single-ended signal conversion, and digital signal amplification (*Figure 3.3*).

Specimen Mounting

A custom mounting device was developed to support correct alignment of specimens and to minimize the shape, weight, and inertia of cadaver mounting components. For both the femur and tibia, complex casting molds were developed that accommodate a large range of bone sizes without intersecting muscle paths (*Figure 3.2b*). The mounting fixture has four line lasers that project two intersecting planes as guides for bone cutting and casting. During alignment, each bone was adjusted until the line lasers intersected its proximal and distal joint centers of rotation, which ensured that the mechanical axis of each bone was aligned to its respective manipulator. The effective length of each bone was matched to that of the *in vivo* subject by removing the proximal end of the femur and the distal end of the tibia. While maintaining proper alignment, the bone was then lowered into the mold, and polyurethane (ProtoCast 80R, Industrial Polymers Corp., Houston, TX) was poured into the mold to secure the bone to the metal base for simulator interfacing.

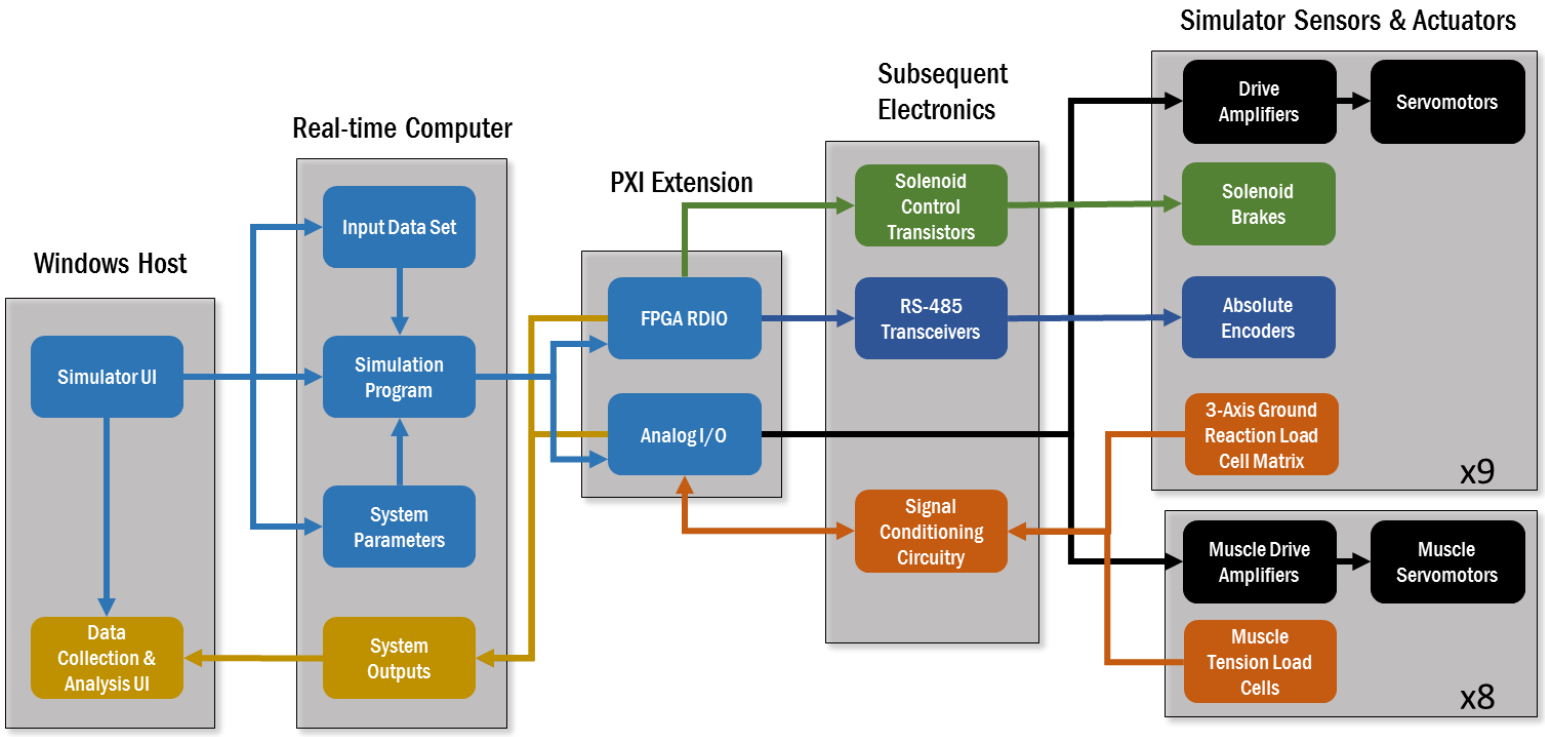

Figure 3.3: Block diagram of UTJLS control structure. Specimen instrumentation is not included in the diagram but is collected in parallel by another computer and data acquisition system.

3.2.2 Controller Development

Controller Architecture and Functions

During each loop iteration at a rate of 2000 Hz, the controller collects and stores sensor data, loads trajectory data, calculates feedback command outputs, and checks safety limits for all twenty-nine sensors and seventeen actuators. In addition, the UTJLS program also provides a variety of functions to assist in cadaver testing including data review, manual subsystem control, specimen alignment, trajectory planning, and error reporting.

Control Strategy

To support accurate application of force and positions, the simulator employs a variety of control strategies that may be applied synchronously. These control strategies include feedforward force, feedforward position, force feedback, position feedback, and compensation for gravity and friction. Feedforward command voltages are determined by multiplying predicted forces by a loading constant and predicted accelerations by a mass constant, where acceleration is calculated from predicted positions using derivative estimation. Gravity compensation is configured for three axes including θx^H, θx^A, and Hz. The compensation for Hz is a constant voltage offset, while gravity compensation for θx^H and θx^A monitors the present rotation and adds a voltage command based on a sinusoidal fit. The friction compensators use position feedback and derivative estimation to determine the current velocity. If velocity magnitude exceeds a specified range, the controller applies a command voltage in the same direction of the measured velocity. Serving as the principal control strategy for the UTJLS, proportional-integral-derivative controllers (PID) are employed for force and position feedback, which are operated synchronously to support hybrid control.

Simulation Phases

Each simulation contains multiple phases of control. The seeking phase initiates the procedure by applying tension to all tendons and ramping the specimen to the initial position of

the maneuver, where it is locked in place. After resting to prevent risk of motor burn out, the simulator applies the following control sequence: ramp force-controlled axes to their initial loads, ramp position-controlled axes to their initial conditions, perform the maneuver, and undergo a stabilization phase when the maneuver is completed or an error has occurred. The UTJLS controller also supplies an analog signal coinciding with maneuver initiation and completion to synchronize simulator data with cadaver instrumentation.

User Interface

The UTJLS user interface provides numerous features, which are separated into five categories including maneuver selection, parameter configuration, simulation, data analysis, and sub-component operation. When a maneuver is imported or generated, it is saved on the host computer as an option presented in list form. Selection of one of these maneuvers in the interface will send the associated dataset from the host to the real-time control computer, which may then be reviewed graphically alongside feedforward commands. Parameters may be modified manually or by parameter file upload, and since every simulation outputs a copy of the current parameter file, the UTJLS can always be reverted to a previous configuration to identically recreate a test. If an error occurs during testing, the controller will immediately stabilize the simulator and display a description of the error. When a simulation is completed or an error is encountered, the program then stores the maneuver trajectories, sensor measurements, and parameter configuration to a file on the host computer.

Control Scheme

The UTJLS controller's flexible architecture allows for various control schemes to be implemented. Excluding musculotendon actuators which are only configured for force control, each axis may be selected to operate with position feedback, force feedback, or hybrid feedback. *Table 3.4* identifies the available feedback sources and the control scheme selected for squat testing.

3.2.3 Squat Simulation

Simulator Input Data

An athletic male (age: 20 years, height: 1.68 m, weight: 498 N) participated in a motion capture session where he performed five trials of two different squat techniques. Test was approved by the internal review board and an informed consent form was signed. Subject was instrumented with a 37-marker set of the lower body (Northern Digital, Ontario, Canada) and electromyography (EMG) electrodes on the eight muscles represented on the simulator (Delsys, Boston, Massachusetts) with each foot on a force platform (Bertec, Columbus, Ohio) positioned shoulder width apart. Subject was instructed to squat descending for five seconds until the tops of his thighs were parallel to the ground and take five seconds returning to stance. Squats were performed with center of force directly on his heels (heel squat) and on his toes (toe squat) at the apex of the squat. A model was developed in Visaul3D (C-Motion Inc., Germantown, Maryland) and allowed for three rotations and three translations at the hip, knee, and ankle joints. Lower extremity rotations, translations, moments, and ground reaction forces (GRF) were calculated, exported, and used as inputs for the UTJLS *in vitro* simulations. Individual muscle forces were calculated through CEINMS, a hybrid electromyography-driven model, and input into the simulator (Sartori et al. 2012).

Cadaver Preparation

Four lower extremity male specimens (age: 21-55 years, side: right) were labeled M, K, U, and B. Specimen M, U, and B were partially fixed, whereas specimen K was fully fixed. While skin, adipose tissue, and fascia were removed up to the knee, the joint capsule, tendons, ligaments, and soft tissue inside of the knee were left intact. Tendons were cleaned of muscle tissue and transected 75 mm from their attachment point. Anterior incisions were made along the medial and lateral aspects of the patella to support instrumentation including a differential variable reluctance transducer (DVRT) (LORD Sensing, Willston, Vermont) and a custom pressure sensor (Teksan, Inc., Boston, Massachusetts). Posterior incisions were made superior to the medial and lateral

menisci allowing insertions of the custom pressure sensor and placed anteriorly through the joint capsule superior to the meniscus. Sensor was surgically attached both anteriorly and posteriorly. DVRT was sutured onto the anteromedial bundle of the ACL. The patella incisions were sutured closed with sensors inside to mimic an intact knee capsule. Specimen was placed in the UTJLS and tendons were connected through freezer clamps (*Figure 3.2a*).

Tendons were wrapped in gauze, covered in electrolyte gel, and inserted into extension hulls which were attached to tension load cells and musculotendon actuators. Tendons were frozen in liquid nitrogen to prevent damage and increase tensile strength (Sharkey, Smith, and Lundmark 1995). Motion capture bone pins (Northern Digital, Ontario, Canada) were screwed into the femur, patella, and tibia (*Figure 3.2a*).

Experimental Protocol

To account for specimen geometry and errors during casting, an alignment protocol was used to manually determine specimen specific offsets for θy^H and θz^H. During this protocol, the simulator applied a vertical 100 N force at 30° and 90° flexion with all other GRF's held at zero. Offsets were then iteratively adjusted until the tibial plateau forces were distributed across both the medial and lateral pressure sensor pads to replicate a 1.5:1 force distribution respectively (Miller et al. 2009; Werner et al. 2005).

Prior to calibration testing and squat simulation, an axial preload of 500 N was applied to the specimen for pressure sensor conditioning. Pressure sensor calibration tests applied a vertical 250 N force at 60° flexion with all other GRF's held at zero, and the same test was applied at 30° flexion to measure offset of internal/external rotation (IE). Each of the four specimens underwent three heel squat tests with musculotendon force, three heel squat tests without musculotendon force, three toe squat tests with musculotendon force, and three toe squat tests without musculotendon force. Only two toe squat tests without musculotendon forces were collected from specimen K due to a labeling error. In total, data from 47 tests was collected to determine the accuracy and repeatability of the UTJLS. The magnitude of the musculotendon force profiles were

scaled by 50% of *in vivo* estimates to prevent tendon failure during testing. Tibiofemoral contact, relative ACL strain, and relative tibiofemoral kinematics were collected for a future study identifying differences between heel and toe squat maneuvers. The VM tendon of specimen M was ruptured during testing and replaced with a threaded-insert.

Data Conditioning

For repeatability and accuracy analysis, the signal output from the UTJLS force sensors were low-pass filtered at 58 Hz to eliminate interference from nearby AC power, and all signals including position sensors were resampled and interpolated from 2000 Hz to provide an effective 100 Hz sampling.

Calculation of Anatomical Rotation

The anatomical rotations presented in this study were determined through a vector analysis using the floating axis method described in Grood and Suntay 1983; however, the axes were not determined by bony landmarks. Rather, the anatomical axes were identified from simulator sensors assuming that the calibration protocol aligned the FE axis to the simulator's X-axis and achieved zero IE.

Statistical Methods

This study assessed the short-term accuracy and precision errors of the UTJLS during the four squat maneuvers described in the experimental protocol. Standard deviations were determined for the UTJLS position and force sensors identified in Table 4 along with the three linear forces measured by the Omega160 load cell (i.e. Fx^H, Fy^H, and Fz^H). The following equations were used to calculate standard deviation and upper limit of confidence intervals for accuracy, trial repeatability, and specimen repeatability (Glüer et al. 1995):

$$SD = \sqrt{\sum_{k=1}^{m}\sum_{j=1}^{n_j}\sum_{i=1}^{o_i}\frac{(x_{ijk}-y)^2}{df(o_i)}} \quad (1)$$

$$df = \sum_{k=1}^{m} (n_j - 1) \tag{2}$$

$$\sigma^2 < \frac{df}{\chi^2_{\frac{\alpha}{2},df}} SD^2 \tag{3}$$

where *SD* is standard deviation, x_{ijk} is the sensor measurement collected on specimen *k* during maneuver *j* for data point *i*, *y* is the reference value for the corresponding data point, *df* is the degrees of freedom of the test, o_i is the total number of data points collected during trial *j*, n_j is the total number of trials for specimen *k*, *m* is the total number of specimen, σ is true error, and χ^2 is the chi-square distribution with probability level $\alpha/2$ with *df* degrees of freedom. The reference value, *y*, is equal to the target trajectory for control accuracy SD, the mean average of all specimen during the same maneuver type for trial repeatability SD, and the mean average of specimen *k* during the same maneuver type for specimen repeatability SD. Offsets for θy^H, θz^H, and θz^A were subtracted from their respective measurements and during calculation of reference trajectories.

3.3 Results

3.3.1 Position Control Response

The four rotation motors operating with position control feedback demonstrated excellent accuracy and trial repeatability with *SD*'s less than 0.13° and 0.12° (*Table 3.5*). Alignment offsets for θy^H were 3.5°, 5°, 0.5°, and 5° and alignment offsets for θz^H were 2°, -2°, 2.5°, and -12° for specimens M, K, U, and B. The average result for each specimen during heel squat testing including 50% musculotendon forces is shown on *Figure 3.4a*.

Table 3.5: Standard deviation of independent variables

Axis	Controller Accuracy	Repeatability	
		Trial	Specimen
θx^H (°)	0.127	0.113	0.110
θy^H (°)	0.018	0.013	0.010
θz^H (°)	0.009	0.006	0.005
θx^A (°)	0.101	0.095	0.093
Fx^A (N)	14.1	8.3	5.8
Fy^A (N)	21.3	15.3	12.1
Fz^A (N)	29.0	19.4	10.7
My^A (N m)	4.3	3.1	1.9
Mz^A (N m)	4.4	2.5	1.5
M1 (N)	5.4	4.9	4.4
M2 (N)	7.9	6.0	4.9
M3 (N)	7.9	5.1	4.3
M4 (N)	2.8	2.3	1.8
M5 (N)	2.3	1.5	1.1
M7 (N)	7.8	6.1	5.0
M8 (N)	2.6	1.8	1.2

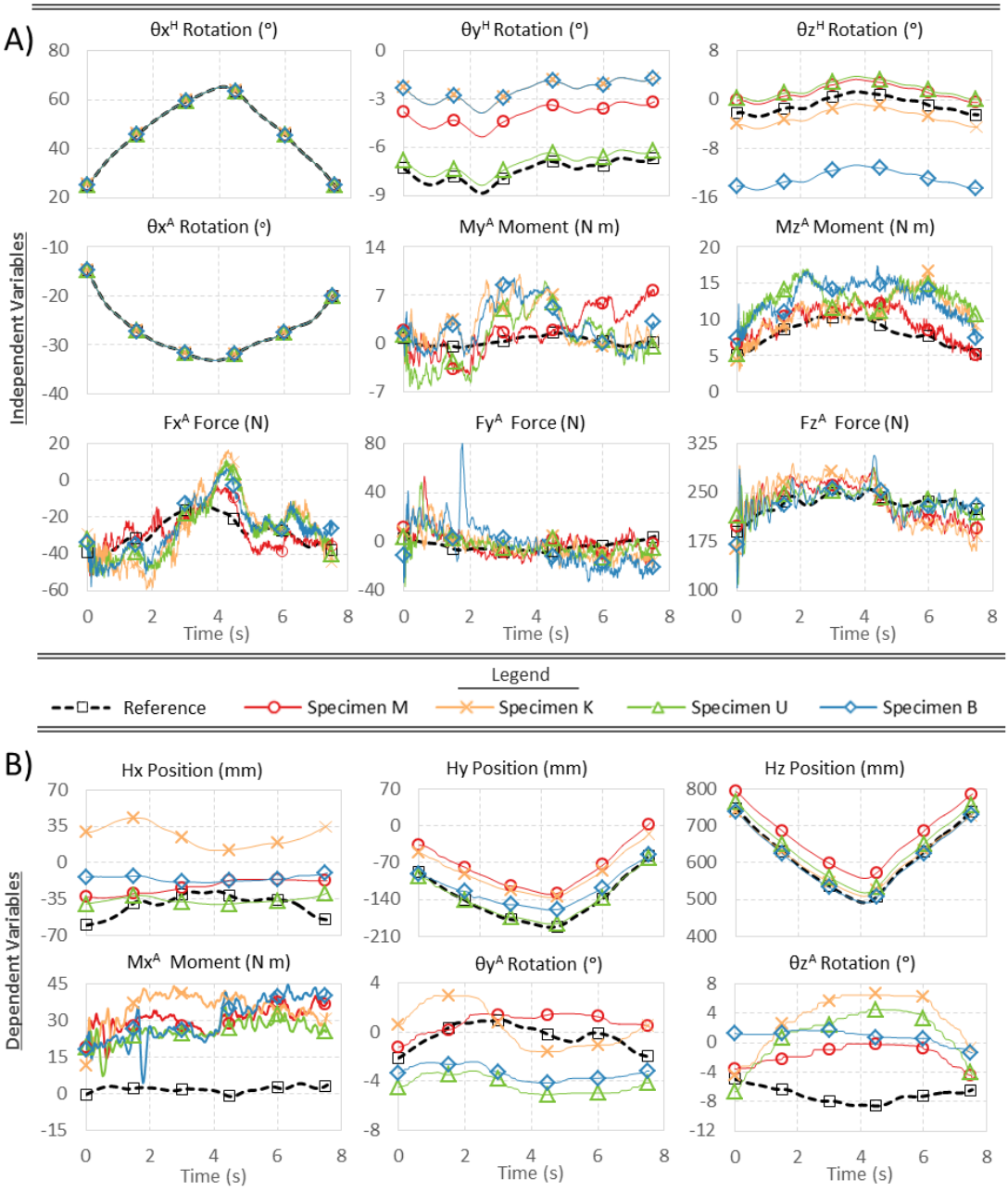

Figure 3.4: Simulator response during heel squat tests with 50% musculotendon forces. Each series is the average of three trials for each specimen. In addition to musculotendon forces, (A) independent variables include position control of four rotations (θxH, θyH, θzH, and θxA) and hybrid control of five GRFs (FxA, FyA, FzA, MyA, and MzA). (B) Dependent variables measured by the UTJLS includes three hip positions relative to ankle center (Hx, Hy, and Hz), two tibial rotations (θzH and θxA), and one GRF moment (MxA). Note that θyH and θzH follow offset profiles in accordance with specimen-specific, alignment parameters identified during static testing.

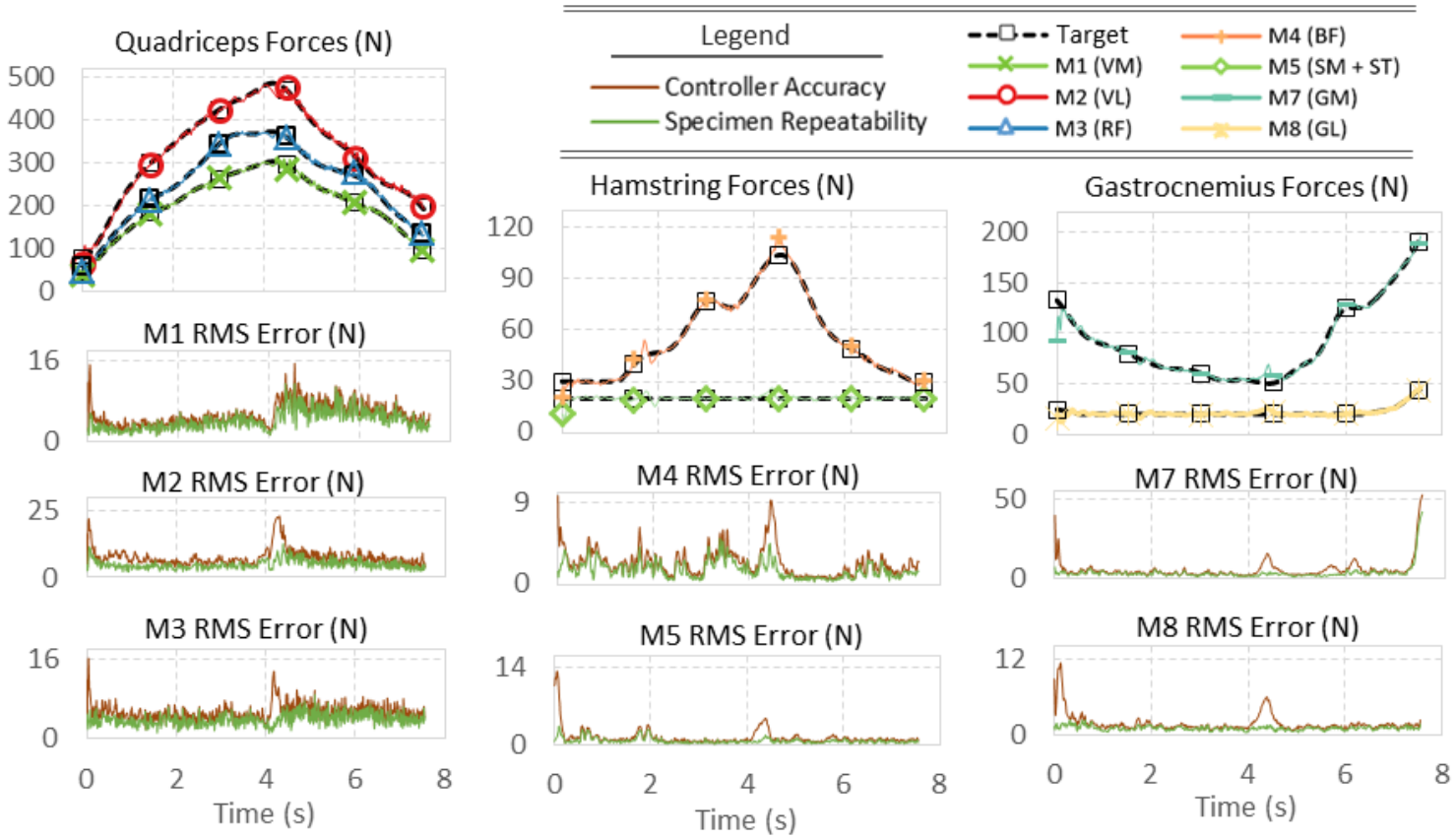

Figure 3.5: Average musculotendon forces of specimen B during heel squat simulation, which are indicative of a typical trial. The RMS error shown is calculated from heel squat simulation data with musculotendon forces collected from four specimens that underwent three trials each. Controller accuracy is compared to desired path, and specimen repeatability is compared to specimen average.

3.3.2 Force Control Response

The seven musculotendon actuators utilized force PID control without any form of position feedback. Accuracy and trial repeatability for all musculotendon forces was less than 8 N for every axis (*Table 3.5*). These results demonstrate an excellent force response as desired for *in vitro* testing with no need for further force control development. The average musculotendon forces for specimen B during heel squat testing with 50% musculotendon forces is shown on *Figure 3.5*.

3.3.3 Hybrid Control Response

Axes utilizing hybrid feedback were tuned to optimize force response. The corresponding GRF's had a maximum accuracy SD of 29 N for forces and 4.4 N m for moments, and the corresponding SD for specimen repeatability was 12 N and 1.8 N m (*Table 3.5*). The average result for each specimen during heel squat testing including 50% musculotendon forces is shown on *Figure 3.4a*.

3.3.4 Dependent Variable Repeatability

The results for sensors with no targeted output are less predictable and repeatable than those that the UTJLS monitors and controls. The SD for each axis is shown on *Table 3.6*, and the average result for each specimen during heel squat testing with 50% musculotendon forces is shown on *Figure 3.4b*. Alignment offsets for θz^{A} were -0.1°, 14.7°, 5.6°, and 7.7° for specimens M, K, U, and B respectively. Included in this analysis are resultant anatomical rotations, which despite no explicit control, maintained FE within a SD of 0.38°.

Table 3.6: Standard deviation of dependent variables

Axis	Trial Repeatability	Specimen Repeatability
Hx (mm)	24.4	8.1
Hy (mm)	25.9	1.3
Hz (mm)	24.9	4.1
θy^A (°)	2.52	1.17
θz^A (°)	2.55	1.26
Fx^H (N)	15.3	4.7
Fy^H (N)	15.5	8.7
Fz^H (N)	18.6	7.0
Mx^H (N m)	7.6	4.6
My^H (N m)	9.5	4.4
Mz^H (N m)	6.6	1.9
Mx^A (N m)	7.6	4.5
FE (°)	0.26	0.10
VV (°)	2.51	1.17
IE (°)	2.55	1.23

3.3.5 Differences due to Musculotendon Loading

For most sensors, application of musculotendon forces minimally influenced accuracy or repeatability, but for some, the effect was substantial. For example, during heel squat testing, musculotendon forces improved the specimen repeatability RMS of Mx^A and Fy^A by 2.6 N m and 6.7 N. The same change in loading increased IE specimen repeatability RMS by 0.63° but reduced RMS accuracy error by 6.2°. Anatomical knee rotations of one specimen are shown in *Figure 3.6*.

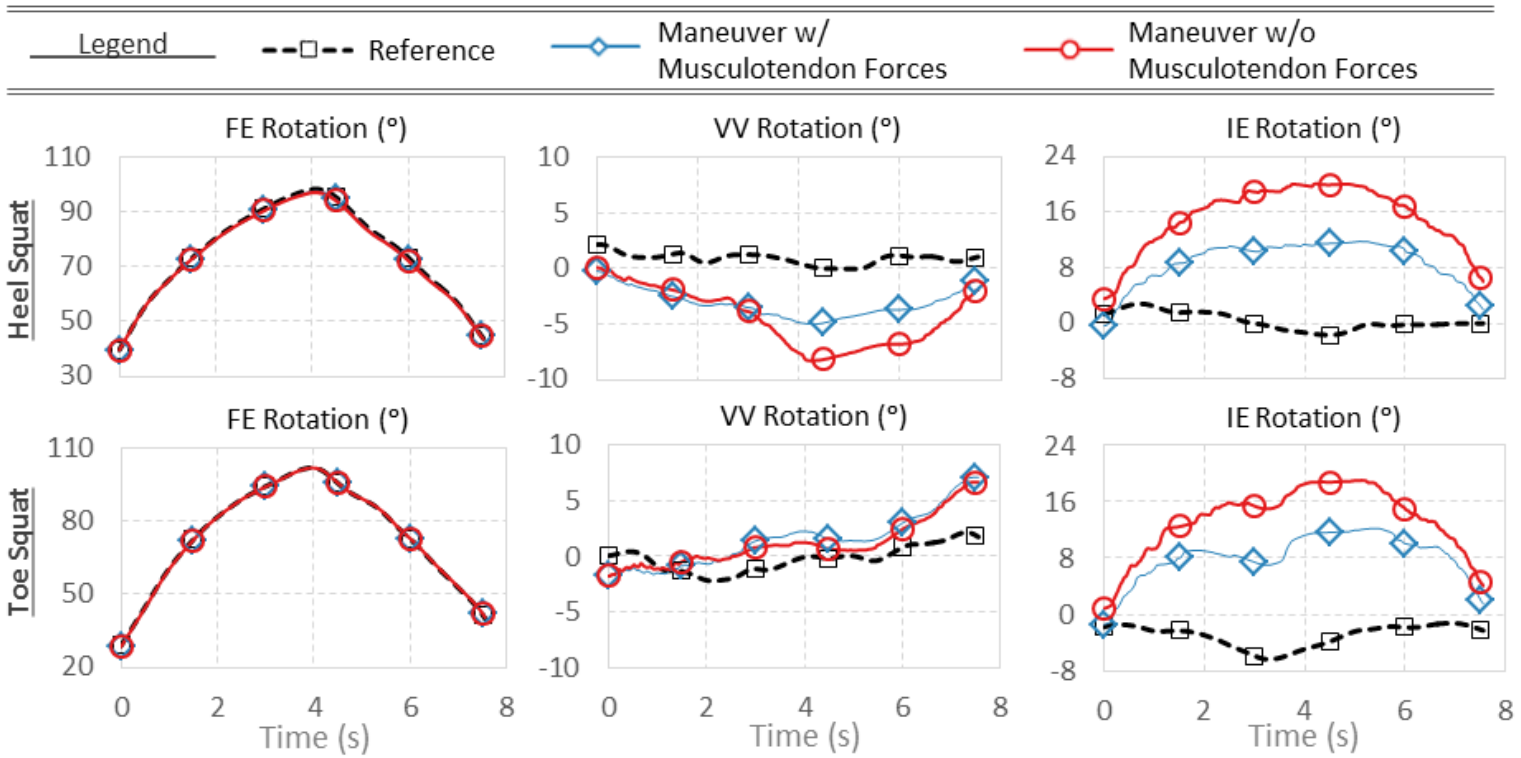

Figure 3.6: Average anatomical rotations of specimen U during heel and toe squat tests performed on the UTJLS. Positive direction of vertical axis indicates increasing flexion, varus, and internal rotation on respective graphs.

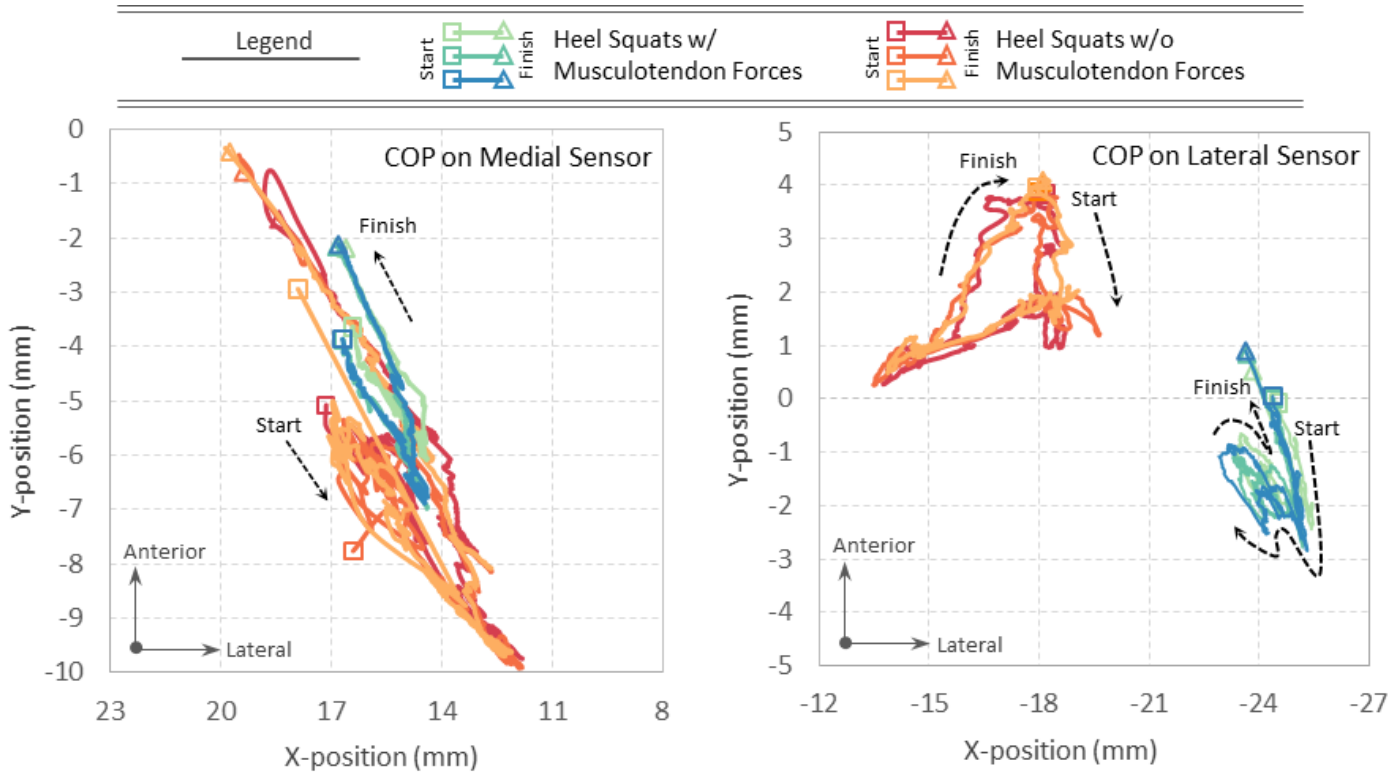

Figure 3.7: Center of pressure on tibial plateau of specimen U during squat simulation.

A similar effect was measured by Tekscan instrumentation, where the introduction of musculotendon forces reduced the range of the center of pressure (COP) travel on both sensor pads without increasing specimen repeatability. Specimen U's COP during heel squat testing is shown in *Figure 3.7*.

3.4 Discussion

During our preliminary work, individual actuator tests demonstrated exceptional accuracy and repeatability, but such results are not indicative of performance during physiological loading where interactions among multiple actuators increase error. A minor example of such an interaction can be seen in *Figure 3.5*, where sudden changes in flexion caused localized peaks in RMS accuracy error for musculotendon forces. Hence, system performance was assessed during simulations of four physiological maneuvers including synchronous control of up to 16 actuators.

3.4.1 Control Scheme

The control scheme of this study effectively performed knee F/E with inverse-dynamics while all other knee DOF's operated in forward-dynamics. This approach provided accurate and repeatable loads while also accommodating geometric variation among cadaver specimens. The desired loading was achieved in real-time despite changes in maneuver, application of musculotendon forces, and specimen.

The results also present some outcomes that are unique to this method. For example, θyA was driven by force rather than position allowing for specimen-specific paths, and as a result, the moment arms between knee center and GRF's also varied throughout maneuvers and generated specimen-specific varus/valgus (VV) knee moments. Other control schemes in literature do not demonstrate this outcome (Goldsmith et al. 2014; Becke and Schlegl 2011; Cassidy et al. 2013; S. L.-Y. Woo and Fisher 2009; Howard et al. 2007). These simulators maintain constant moment arms between knee center of rotation and GRFs by fixing the tibia to the GRF load cell. The UTJLS controller can be configured to effectively match this control scheme by controlling MyA and MzA using θyH and θzH. This control scheme would allow for synchronous control of θyA, θzA,

MyA, and MzA and therefore, consistent application of knee VV and IE moments by GRF's for all specimen.

3.4.2 Controller Response

To date, no study has assessed simulator repeatability and accuracy during a real-time, physiological maneuver that includes musculotendon forces and multiplanar kinematics and kinetics. Time-scaled gait maneuvers of (Noble et al. 2010; Maletsky and Hillberry 2005a), which have similar loading conditions, may serve as a reference for comparison. During simulation of physiological loads, even axes assigned a near zero or constant target experience large disturbances due to direct influence from other axes and inertial effects generated by system accelerations. Despite these disturbances, the position controlled axes and musculotendon actuators performed all tasks with minimal error (*Table 3.5*). The controller accuracy SD's of Fx^A, Fy^A, and Fz^A with a maximum of 29 N are consistent with reported RMS errors in (Noble et al. 2010; Maletsky and Hillberry 2005b), but My^A and Mz^A with a maximum SD of 4.4 N m were less accurate than RMS errors reported in (Noble et al. 2010) (*Table 3.5*).

Numerous factors contribute to the accuracy error of My^A and Mz^A including accuracy of reference trajectories (Figure 3.4b), high-load capacity (*Table 3.1*) operating in a low range of operation (*Figure 3.4a*), disturbances developed from other axes, disturbances from friction, limited resolution from feedback sources (*Table 3.3*), and backlash in the associated gearboxes (*Table 3.1*). These axes demonstrated superior performance during individual actuator testing and with reference trajectories tuned for a specific maneuver. The predicted trajectories for θy^A and θz^A were referenced by the hybrid controller and feedforward components of the controller, but the references did not reflect the actual paths observed during testing, which were specimen-specific and unpredictable prior to testing. Accordingly, reference trajectories tuned for each specimen and maneuver is expected to improve My^A and Mz^A performance. In future studies, improved reference trajectories may be obtained through trajectory optimization algorithms as demonstrated elsewhere (Goldsmith et al. 2014; Noble et al. 2010; Maletsky and Hillberry 2005b),

which have been able to improve force response by more than 85% for linear GRFs and 50% for GRF moments (Bates, Myer, et al. 2015).

The UTJLS demonstrated consistent loading (*Table 3.5*), and the specimen response to that loading was repeatable (*Table 3.6*). Anatomical rotation repeatability was all less than 1.25°, which is reported to be sufficient for investigating passive path kinematics, a simple maneuver when compared to physiological loading (Goldsmith et al. 2014). While the current configuration is suitable for knee testing, improvement may be possible through trajectory optimization and addition of encoder feedback to support hybrid control of musculotendon actuators (*Table 3.4*).

3.5 Conclusion

The UTJLS can simulate physiological loads via *in vitro* musculoskeletal testing including real-time, synchronous application of musculotendon forces and GRF's during multiplanar kinematics. Being the first design of its kind, our simulator utilizes two separate robotic manipulators that contain a total of eight musculotendon actuators and two 6-axis load cells. By adjusting the control scheme configuration, the UTJLS can match the constraints of traditional testing rigs (e.g. oxford rig or robotic arm), recreate absolute motion to reproduce gravitational and inertial loads, and uniquely investigate joint moment contributions from GRF's as demonstrated in this study. With the necessary DOF's, ROM, and speed, the UTJLS is suitable for future testing of faster maneuvers, a variety of human joints, and a kinetic chain of two connected joints (e.g. hip and knee).

Chapter 4: Aim 2 - Fused Filament Fabrication Printer with an Actuated Element for Blending and Local Composition Control

4.1 Introduction

The purpose of aim 2 is to broaden characterization of FFF with active-mixing through mechanical testing of tensile specimen composed of blended thermoplastic filaments, and the secondary goal of this work is the advancement of technology to support synthetic knee development as described in aim 3. This technology enables the application of local composition control in FFF. These advances in technology enable printing materials with a wide range of properties by varying feed rates of multiple filaments which are blended within the hotend before extrusion.

Printer development began with components included in commercially available desktop FFF printer kits, but each prototype printer was modified from the original design with extensive alterations including design and fabrication of custom hotends and extruders, design and implementation of custom heating systems, replacement of printer control boards, modification of printer mechanics, design and fabrication of printer structure, electronics upgrades, and firmware configurations. These printers were supported by slicer software with printer-specific configurations for various applications and custom programs for post-processing slicer results.

Materials were selected for compatibility and with the aim of benefiting simulation of human knee tissues as described in aim 3 and chapter 5 of this dissertation. HTPLA was selected to simulate bone and NF was selected to simulate soft tissues ("NinjaFlex 3D Printing Filament" 2018; "HTPLA Raptor - High Performance PLA 3D Filament - HD Blue Steel - 1.75 – Maker Geeks 3D Printing Filaments" 2018). Eight different blends of HTPLA and NF filament were produced by the final prototyped printer and characterized through tensile testing. Eight combinations of these blends were printed in a tensile specimen with a curved surface for determination of interface bond strength.

Results from this study provided insight into FFF printer design for local composition control, the effects of print configuration, material parameters for synthetic tissue design, and

potential increased strength due to implementation of functional gradients. Notable findings include the effects of seal design on the mixing FFF printer's performance, methods for minimizing oozing and stringing, methods for reducing contamination from unused filaments, techniques for balancing composition of blended filament composition, the effects of raster overlap between regions, the effects of overlap between infill and perimeters, and material properties of varied material blends and material interfaces. Material properties determined through tensile testing including modulus of elasticity (E), Poisson's ratio, yield stress (σ_Y), percent elongation at yield ($EL\%_Y$), ultimate tensile stress (UTS), and percent elongation at failure ($EL\%_F$) and the interface bond strength (σ_{IBS}) between a variety of compositions.

4.2 Background

With development of the synthetic knee of aim 3 as the target application for the FFF printer of this aim, it is necessary to understand methods for simulating joint kinematics and mechanical properties of human tissue in addition to understanding additive manufacturing, local composition control, mechanical testing techniques, and material properties.

4.2.1 Simulation of Human Knee Kinetics and Kinematics

Joint kinetics and kinematics have been investigated through a variety of computational, *in vivo*, and *in vitro* methods. A brief overview of these techniques is provided in chapter 3 of this dissertation.

Computational model development provides several similarities to the synthetic knee approach of this study. During development of computational models for knee studies, tissue elements of the knee are selected for inclusion, and the structure and properties of each element are defined in software. Although computational models not limited to this technique, many develop their design from images from a single knee for development of tissue geometries. In contrast to generic models, the resulting geometries are known as subject-specific models. The materials assigned to these tissue elements can be either subject-specific or general.

Additional details on biological material properties are provided in section 5.2.4.

4.2.2 Thermoplastics

Thermoplastics are polymers that can be reshaped by increasing their temperature without a chemical change. Thermoplastics are conventionally categorized as either amorphous or crystalline depending on material properties. Below glass temperatures (T_g), thermoplastics are hard and brittle behavior, and above this temperature, thermoplastics become soft and rubbery.

4.2.3 Additive Manufacturing

Because of its versatility, AM, often known as 3D printing, has been integrated into a wide variety of industries and even made available for home use. Many additive manufacturing technologies have been developed, which vary greatly in design-type, capabilities, and cost. (Prakash, Nancharaih, and Rao 2018). All of these technologies follow a common work flow, which progresses from concept through software, fabrication, and post-processing to its application (Gibson, Rosen, and Stucker 2015).

4.2.4 FFF Technology

FFF is an AM method that pushes a polymeric material in filament form into a heated liquefier by a roller mechanism driven by a motor. Per layer, filament is extruded in an X-Y plane onto a substrate as rasters that cool and form perimeters and infill. Each of these layers stack to form a part relying on adhesion between rasters (Bellini and Güçeri 2003).

4.2.5 Local Composition Control

LCC is an emerging topic of research, which has been defined as control of a continuously varying spatial composition profile of two or more materials. The technology developed in this study is based on FFF augmented by a custom hotend with an actuated element intended to provide LCC through filament blending. Similar technology is rare and has not demonstrated the ability to mix materials with the wide range of stiffness as demonstrated in this study. Known attempts to enable LCC in FFF include the mixing printers developed at the University of Bath (Taubert 2012; Corbett 2012).

Most developments in FFF that resemble LCC are intended for control of color. Some studies relied on passive mixing with multiple filament inlets but known applications remain limited to variation in color. Among the most advanced forms of this technique is the control scheme presented by Song and Lefebvre (Song and Lefebvre 2017). Although clearly not intended to be a fully functional implementation of LCC, the dual-color mixing performed by Reiner et al. attempted to control color through raster patterns and is worth mentioning as it resembles the drop-into-drop technique used for LCC in inkjet printers but implemented using FFF (Reiner et al. 2014).

LCC is among the most rare and advanced AM capabilities. The most common ability is almost exclusively provided by high-cost, inkjet printers, which utilize a drop-into-drop method of varying composition. A custom multimaterial printer developed at MIT has demonstrated LCC using advanced the most advanced features including LCC is the MultiFab machine developed at the Massachusetts Institute of Technology (MIT) (Sitthi-amorn, Lan, and Wang 2015; Zhang et al. 2016).

Lan developed a nozzle with an active mixing element for material extrusion of fluid polymers during 3D printing. This printer demonstrated variable stiffness and gradients through composition control (Lan 2018).

4.2.6 Mechanical Characteristics of Blended Materials Manufactured by FFF

Other studies have investigated mechanical properties of FFF of polymer blends and composites. These materials have been blended in screw extruders and formed into filament., which is then printed in standard FFF printers (Rocha, Perez, and Roberson 2014; Torrado Perez, Roberson, and Wicker 2014).

4.2.7 Functional Gradients

FGs are material features with varying composition, microstructure, or discontinuities throughout their volume (Mahamood and Akinlabi 2017). FGs have been applied to numerous industries including aerospace, medicine, energy, and optoelectronics, which are utilized for their

ability to transition between varying compatibility, increase strength through increased bond strength and reduced stress concentrators, alleviate stresses resulting from thermal expansion, and increase a material's temperature service temperature. Notable to this study, FGs are common within human tissue and provide a necessary function for material strength in musculoskeletal systems (Zhang et al. 2016). As this study investigates the potential benefit of functional gradients in LCC during FFF it provides an opportunity to integrate them into the synthetic tissue of aim 3. Highlighting the importance of this study. few studies have investigated LCC in AM for FG fabrication, but this subject is becoming more common in literature as emerging technologies enable its application. AM technologies that can potentially produce FGs include, material extrusion, selective laser processes, and material jetting (Zhang et al. 2016).

4.2.8 Interface Testing Methods

Standards for determining interface strength include ASTM D2095 and ASTM D3528. These tests investigate the interfaces of lap-joints and butt joints and do not account for stress distributions across those interfaces (ASTM D2095; ASTM D3528). Where interfaces intersect a free surface, an interface corner is formed, which is at risk of forming stress singularities. Such stress singularities can dominate the behavior and strength of an interfaces, which prompted research to develop alternative bond strength test procedures, which utilize geometries that attempt to prevent the formation of stress singularities. Methods include but are not limited to integrating curved interfaces into flat coupons (Lauke, Schüller, and Schneider 2012) and testing cylindrical specimen with a spherical interface (Chowdhuri and Xia 2013). The curved interface described by Lauke et al. is limited in its ability to prevent stress singularities due to the edges present in the third dimension of the specimen, which is why future studies by Lauke, attempted to further characterize this effect (Lauke 2007), and Chowdhuri et al. and Xia et al. alternatively selected spherical interfaces to prevent the effect altogether (Chowdhuri and Xia 2013; Xia, Chowdhuri, and Ju 2013).

The curved interface proposed by Lauke et al. uses a cylindrical surface that can be fabricated without inducing the stair-step effect, when the specimen is manufactured flat on the printer bed. Although the spherical interface described in these studies were able to avoid stress singularities, the curved interface was selected to minimize stress singularities while avoiding surface roughness associated with the stair-step effect.

4.2.9 Relevant FFF Print Characteristics and Defects

The quality of FFF printed parts are often described in context of mechanical properties, geometric accuracy, and print defects. Many of these limitations and defects are linked to features integrated into firmware, hardware, and slicing software. The most relevant for discussing the results of this study include anisotropy, oozing, ghosting, and surface roughness associated with features like the stair-step effect. The mixing printers developed in this study amplify some of these defects requiring printer-specific tuning and development.

Anisotropy

Functional parts produced by FFF are most often limited by the anisotropic weaknesses that vary with build direction and infill pattern. Anisotropy has been observed for both tensile and compressive properties. The effect of material properties is sensitive to printed materials. Different materials with nearly identical FFF settings have demonstrated anisotropic reduction in strength ranging between 24% and 70% (Rocha, Perez, and Roberson 2014; Torrado Perez, Roberson, and Wicker 2014; Torrado and Roberson 2016; Torrado Perez 2015; Lee et al. 2007).

Oozing

Oozing in FFF is an effect by which material unintentionally exits the extruder's nozzle. This material may cause defects including undesired deposits of material onto printed parts or zippers, which are holes in the printed parts that develop after material fails to extrude as intended because of the material missing from the nozzle (Hergel and Lefebvre 2014).

Ghosting

Ghosting are defects usually associated with surfaces and sharp changes in print direction. These effects often result from carriage vibration or deflection of printer mechanics and form faint variations in either the extruder path or extrusion width (Coward 2015).

Stair-Step Effect

A common effect that contributes to surface roughness in additive manufacturing is the stair-step effect. Edges of each layer form steps equal to the layer height. These steps are minimized on vertical and horizontal build orientations and largest on build orientations with a slope of 45° (Pandey, Reddy, and Dhande 2003).

4.3 Methods

The initial methods employed in this study investigated a variety of materials and fabrication techniques using conventional FFF printers. These materials and methods were refined during multiple iterations of mixing printer development. Once the final design iteration of the mixing printer had demonstrated reliable performance and settings were tuned for the selected materials, specimens were printed and tested in tension to determine material properties including modulus of elasticity (E), Poisson's ratio, yield stress (σ_Y), percent elongation at yield ($EL\%_Y$), ultimate tensile stress (UTS), and percent elongation at failure ($EL\%_F$) and the interface bond strength (σ_{IBS}) between a variety of compositions.

4.3.1 Material Selection

The primary purpose of the materials selected in this aim is simulation of human tissue in aim 3. The function of the materials selected for this purpose include a rigid material to simulate bone, a flexible material to simulate soft tissues, and a soluble material to act as sacrificial support to provide smooth surfaces and barriers between articulating surfaces when printing complex geometries. After a preliminary investigation into custom-made filaments produced at The University of Texas, the material selection process was limited to commercially available filaments that are commonly used in desktop FFF printers. This is appropriate as it ensures that the materials

selected are good candidates for the FFF and are likely to continue to be available for future development of synthetic tissue.

Pilot Study – Custom-made Filament

A Lulzbot Taz 5 (Aleph Objects, Inc., Loveland, Co) printer that had been modified for bi-material printing was used for this study (*Figure 4.1A*). The ABS filament used to simulate bone was extruded in-house from MG94 ABS pellets, and the ABS-SEBS filament mixture used for cartilage simulation was extruded in a proportion of 25% MG94 ABS and 75% SEBS pellets by weight.

Interest in an ABS-SEBS mixture was driven by the low hardness (shore 60A) of the 90% SEBS version of the filament, which could potentially assist with matching physiological pressure distributions, but testing revealed high friction that negatively influenced printing performance and may be a problem for the articulating surfaces of the synthetic knee. Additionally, high friction filaments will be problematic for a mixing printer, which requires higher extrusion forces due to an increased hotend length.

A)

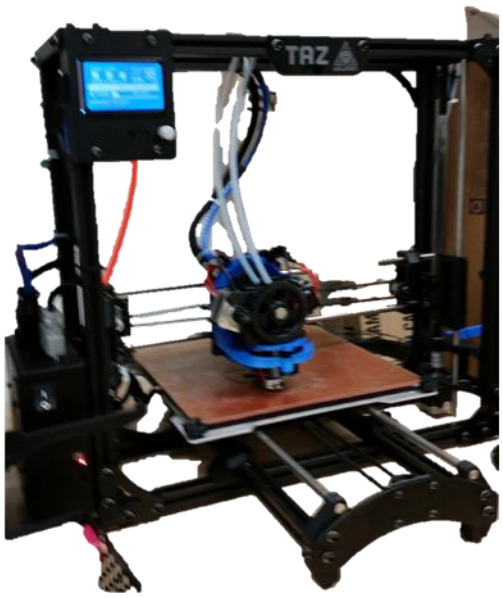

B)

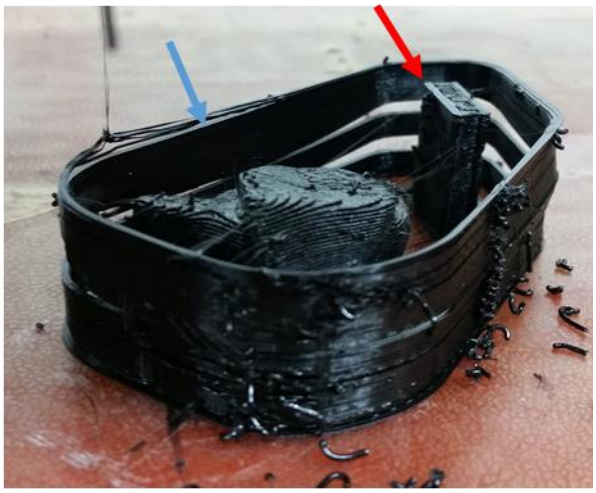

Figure 4.1: A) Lulzbot Taz 5 Traditional bi-material, desktop FFF printer with modification for bi-material printing. B) Printed patella scaled to 70% of the original size including ooze shield and manual priming tower.

Pilot Study – ABS and NF

A preliminary study using ABS for bone and NF for ligaments sought to qualitatively mimic cruciate ligament mechanics. The cruciate ligament geometry was extracted from the knee model using SOLIDWORKS® (Dassault Systèmes SolidWorks Corporation, Waltham, MA) (*Figure 4.2A*) and printed on a low-cost, custom i3 Prusa printer (*Figure 4.3*).

Repetier-Host (Hot-World GmbH & Co. KG, Willich, Germany) settings for conversion of models into G-code were customized for printing ABS and NF on the printer. The hotend temperature setpoint was 230°C for ABS and 245°C for NF. The temperature used for NF is much higher than was recommended by the

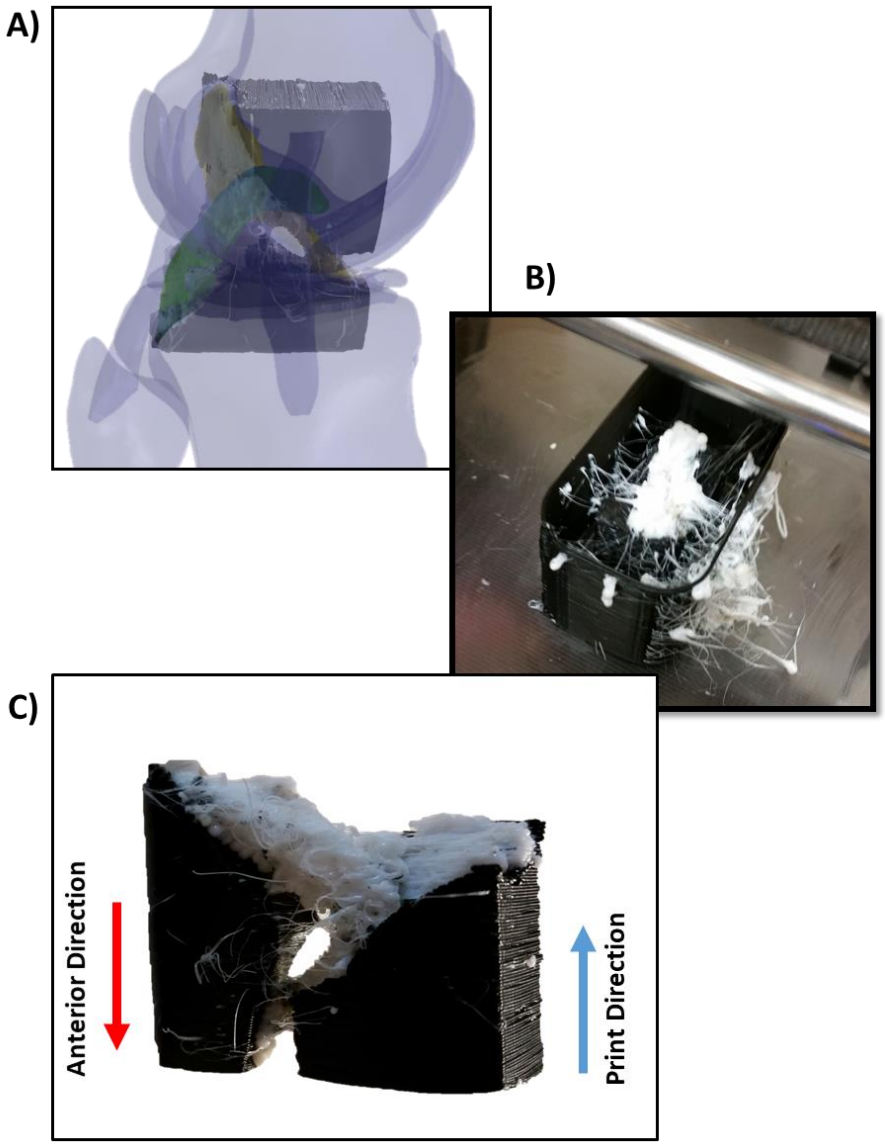

Figure 4.2: A) An image of the printed ACL and PCL with bony islands aligned to a partially transparent image of the source knee model. Yellow shaded region overlaps the ACL. Green shaded region overlaps the PCL. B) Image of printed ACL and PCL with bony islands on print bed. Skirt is shown to prevent oozed NF from sticking to the synthetic ligaments. C) Close-up image of printed ACL and PCL with bony islands. Specimen is oriented as it was printed on the print bed.

manufacturer, but this setpoint along with other considerations were necessary due to the limitations of this printer. The Bowden extruders introduce undesirable effects including friction in the PTFE, guide tube and energy storage due to filament compression during extrusion. The cumulation of these effects can cause delayed extrusion and printer failure due to filament

buckling. This effect was minimized by adjusting Slic3r settings that reduced the resistance to flow through the printer nozzle. Specifically, the hotend temperature was increased to lower the material viscosity, and print speed was decreased to 20 mm/s from 40 mm/s to reduce material flowrate. Although this improved the reliability of the printer, it also increased nozzle oozing and stringing, which prompted the use of settings for printing an ooze guard, filament retraction, and ooze prevention with a 25°C temperature offset (*Figure 4.2B*). The print was oriented to align the printer Z-axis to the posterior direction of the specimen, which allowed for printing without support material. After printing, the surfaces were manually cleaned, and ligaments were de-bonded from one another using a razor (*Figure 4.2C*).

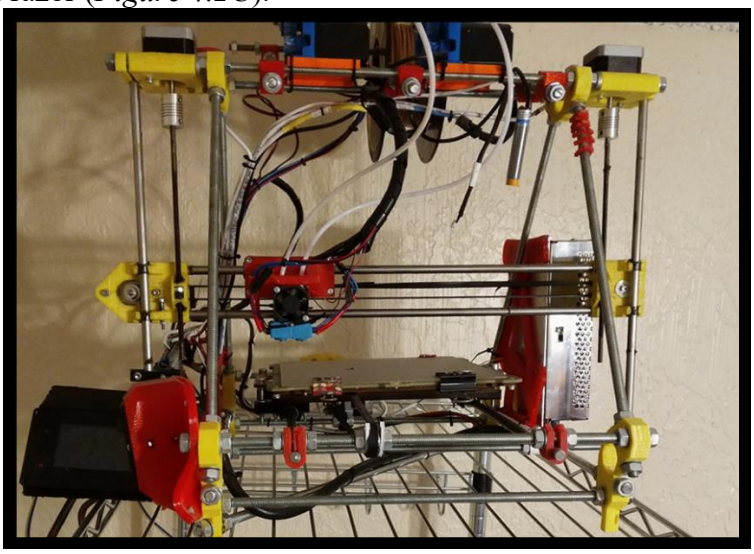

Figure 4.3: Custom Prusa i3 FFF printer including an Azteeg x3 pro motherboard. Mounted on the top of the printer are two bowden extruders that drive filament through PTFE tubes connected to an E3D chimera hotend (E3D-Online Limited, Oxfordshire, UK).

Three identical specimens were qualitatively evaluated through hand-held manipulation, which demonstrated ligament restraint of tibial anterior/posterior translation, ligament wrapping in the femoral notch, and a large but resistant range of motion for flexion/extension (*Figure 4.2C*). Catastrophic failure of the specimen was observed at the interface between the Tibia and ACL. Future testing revealed some misalignment between nozzles, which may have influenced this

outcome, but nonetheless, this mode of failure emphasizes the possible limitations due to interface strength and the stress concentrators developed between soft and rigid materials.

Qualitative Assessment of Commercially Available Materials using a Dual-extrusion FFF Printer

As a wide range of stiffness is desired, one hard filament and one soft filament will be selected and will facilitate simulation of bone and soft tissues. A third filament will be selected to serve as support material during synthetic knee printing but will not undergo mechanical testing. All three filaments must be readily available and compatible with each other. To ensure compatibility between materials characterized in this study, the potential materials were printed on a custom Prusa i3 FFF printer (*Figure 4.3*). Material selection was based on qualitative assessment of bond strength between materials. All three filaments must be readily available and compatible with each other. To complete the selection of materials, the filament options were tested by printing a cuboid of one material on top of an identical cuboid of another material. A qualitative assessment of material compatibility was determined after optimizing printer settings for each test. and the results are shown in *Figure 4.4*.

Material	ABS	PLA[1]	PVA[1]	NinjaFlex[1]	Porolay Lay-fomm	Porolay Gel-lay
ABS			Very Poor	Great		
PLA[1]			Good	Good	Poor[2]	Fail
PVA[1]	Very Poor	Good		Good	Good	Fail
NinjaFlex[1]	Great	Good	Good			
Porolay Lay-fomm		Poor[2]	Good			
Porolay Gel-lay		Fail	Fail			

1. Material selected for synthetic tissue development
2. Interface strength is lost after soaking in water

Figure 4.4: Qualitative assessment of bond strength between materials when printing thermoplastic filaments on top of one another.

Only dissolvable materials were considered for support since they promote a smooth surface finish without requiring extensive post-processing. PVA was chosen over HIPS and PLA since it quickly dissolves in water and does not require a more aggressive solution that may adversely affect other materials. Arbitrary parts were then printed in PVA to optimize settings and confirm that PVA can be reliably printed.

After selecting PVA as the support material, ABS and PLA, the two most common materials in FFF, were investigated for potential use simulating bone. The strength and stiffness of ABS is favorable for bone simulation, but the interface strength between PVA and ABS is too weak to prevent warping, a common issue with ABS (*Figure 4.5*). In contrast, preliminary tests demonstrated sufficient bond strength between PVA and PLA to provide reliable printing and prevent warping (*Figure 4.6*).

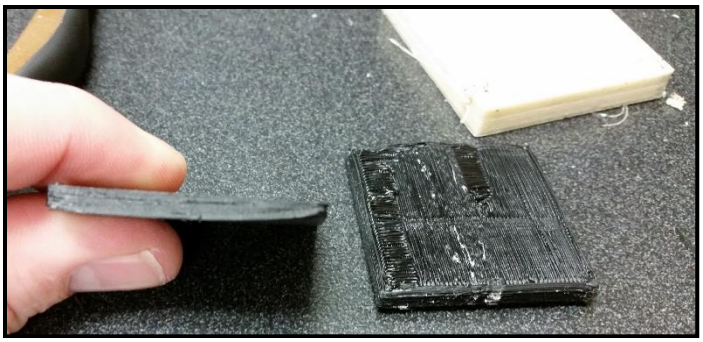

Figure 4.5: Two 40 mm x 40 mm ABS samples (black) that successfully printed on top of PVA (beige). Weak bond strength was unable to prevent ABS warping.

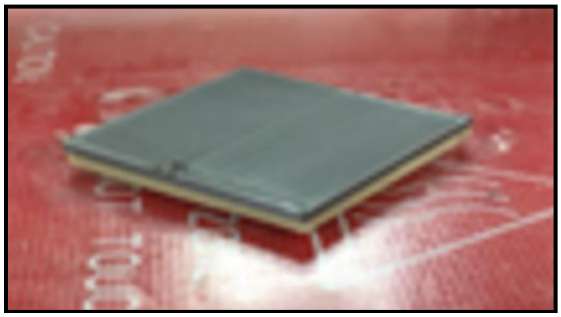

Figure 4.6: 40 mm x 40 mm PLA sample (silver) printed on top of PVA (beige)

Four flexible filaments were tested as options for simulating soft tissue. Specialty filaments that were tested include a custom ABS-SEBS filament produced by the W. M. Keck Center (El Paso, TX), Lay-Fomm 40 (CC-Products, Koeln, Germany), and Gel-Lay (CC-Products, Koeln, Germany). The ABS-SEBS blend was excluded due availability and unreliable printing due to high friction. Lay-Fomm 40 and Gel-lay were excluded after demonstrating weak interface strength between PLA and/or PVA. NF was selected over other flexible filaments as it is commercially available, bonds well to PVA and PLA, prints reliably in direct-drive extruders, has a low coefficient of friction, and is soft enough to simulate soft tissue after structural modification (*Figure 4.7*).

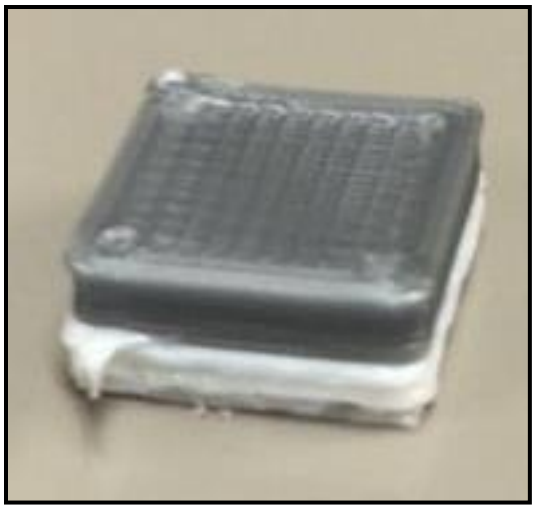

Figure 4.7: 20 mm x 20 mm PLA sample (silver) printed on top of Ninjaflex® (white).

Revision of Material Selection

When operating the mixing printers and printing pure NF in layers with material blends containing PLA, contamination of PLA in pure NF was intermittently observed. This effect was reduced by using custom software to retract inactive filament during nozzle priming, but aggressive retraction settings increased the occurrence of filament jams causing prints to fail. In combination with filament retraction, this effect was eliminated, as observed through visual examination, by replacing the PLA filament with HTPLA filament. All specimen in this study that underwent tensile testing were composed of HTPLA and/or NF.

Another minor modification was made to the material selection as determined by the bond-strength assessment described above. Pure PVA filaments are commonly printed at temperatures below 200°C to avoid thermal degradation but HTPLA and NF was tuned to print at 240°C in the mixing hotend. To avoid jamming and contamination from thermally degraded PVA, the soluble filament was switched to Scaffold (SC) filament (E3D-Online Limited, Oxfordshire, UK), which is PVA-based and has a recommended nozzle temperature of 215°C.

4.3.2 Printer Development

Firmware and Control Board Selection

Open-source firmware including but not limited to Marlin, RepRap (RepRap Contributors 2018), Smoothie, and Repetier-firmware (Hot-World GmbH & Co. KG, Willich, Germany) were reviewed for this application. Firmware was required to have integrated functions for weighted mix ratios for FFF using multiple extruders feeding filament into one nozzle. Both Reprap firmware and Repetier-firmware were noted to have these functions at the time of firmware selection, but Repetier-firmware was selected due to the success of previous studies demonstrating its use for color mixing (Han et al. 2017). The G-code commands for mixing are M163 and M164. M163 sets the weights for a selected extruder, and M164 stores the combined M163 weights as a virtual extruder (*Figure 4.8*).

```
24
25 M163 S0 P15
26 M163 S1 P0
27 M163 S2 P985
28 M163 S3 P6000
29 M164 S0 P1
30
31 M163 S0 P0
32 M163 S1 P0
33 M163 S2 P100
34 M163 S3 P600
35 M164 S1 P1
36
37 T0
```

Figure 4.8: Example G-code file entry using M163 and M164 callouts for mixing weights and virtual extruders assignment. In this example, a command to extrude material from virtual extruder "T0" will split the signals to extrude 0.22%v from motor E0, 0%v from motor E1, 14.07%v from motor E2, and 85.71%v from motor E3.

The control board was selected for compatibility with Repetier-firmware and integrated components for control of mixing printer systems. The control board was required to provide control of eight stepper motors, two heaters, two thermistors, and multiple fans. The Azteeg X3

PRO motherboard (Panucatt Devices LLC, Irvine, CA) exceeds these requirements and was selected for mixing printer development (*Figure 4.9*).

Mixing Printer #1 (MP1)

The first design iteration of the mixing printer was mounted on a Prusa i3 FFF printer (Prusa Research s.r.o., Prague, Czech Republic) and includes a separate QR Bondtech extruder using a standard E3D-v6 hotend (E3D-Online Limited, Oxfordshire, UK) and two QR Bondtech extruders (Bondtech AB, Varnämo, Sweden) for blending two filaments in the custom active-mixing hotend containing a size -105 Kalrez 7075 O-ring (DuPont, Wilmington, DE) (*Figure 4.10-11*). All motors are NEMA 17 stepper motors, and each motor requires a dedicated stepper motor driver. The Mini-Rambo v1.3 motherboard (Ultimachine, South Pittsburg, TN), which came standard with the PRUSA I3 kit, only includes five stepper drives, which is not enough to operate the four motors required for position control, three motors for extrusion, and one motor to actuate the mixing element. The Mini-Rambo v1.3 motherboard was replaced by an Azteeg X3 PRO motherboard (Panucatt Devices LLC, Irvine, CA) with eight stepper drivers and was flashed with Repetier-firmware.

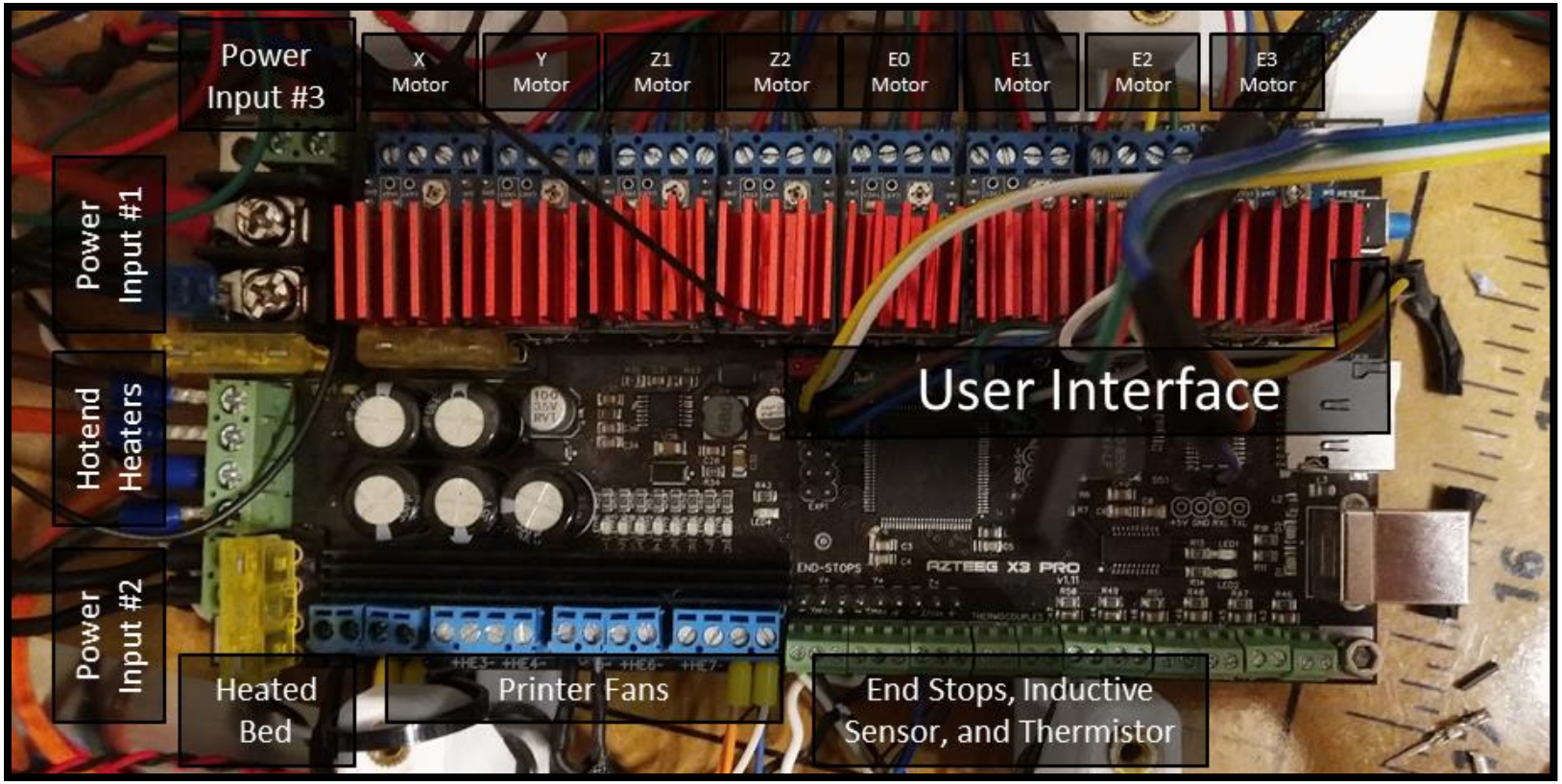

Figure 4.9: Control board configured with wire connections for mixing printer operation

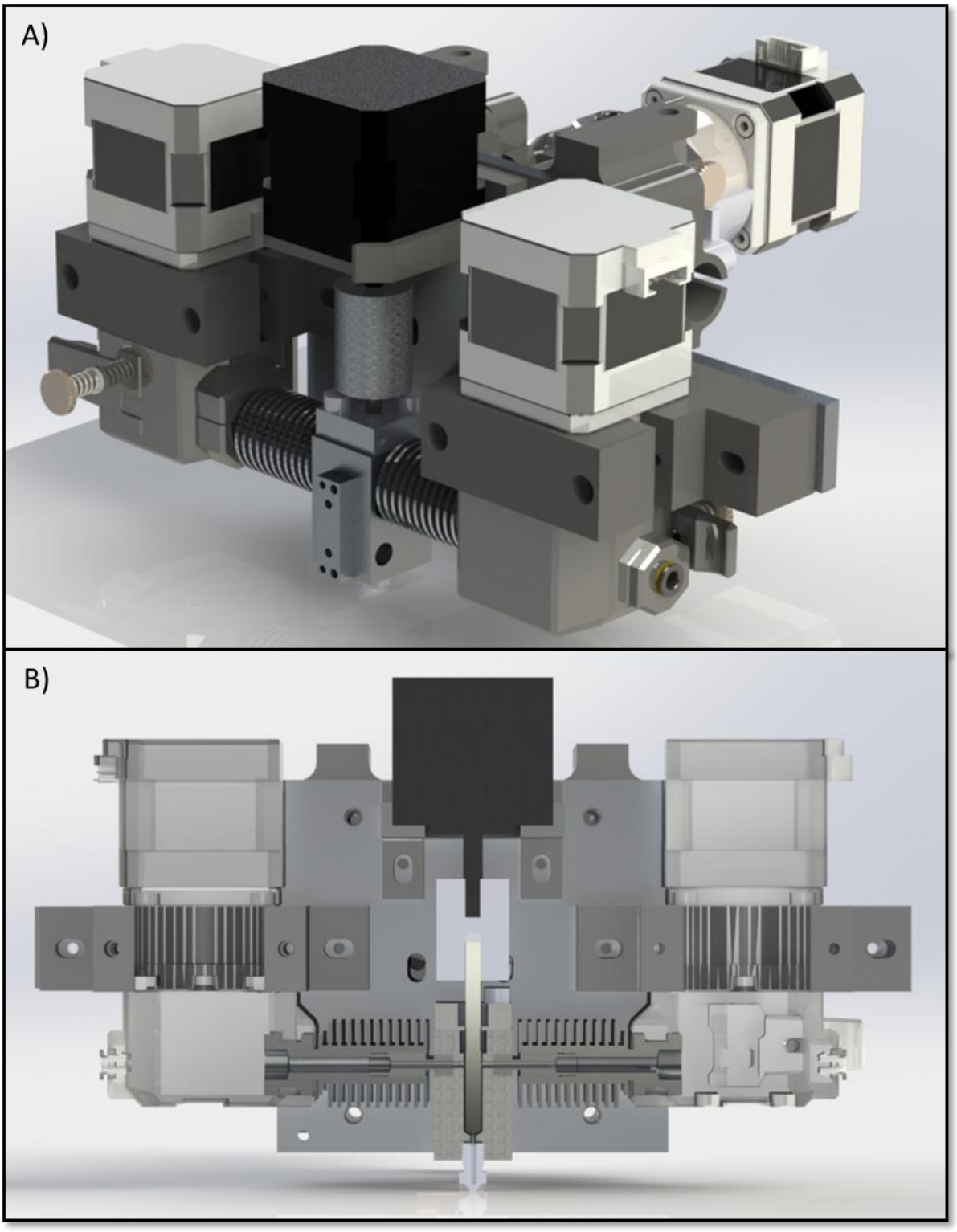

Figure 4.10: A) X carriage of MP1 with mixing hotend with two extruders on the front of the carriage and a secondary extruder and nozzle behind the carriage. B) Cross-section of mixing hotend.

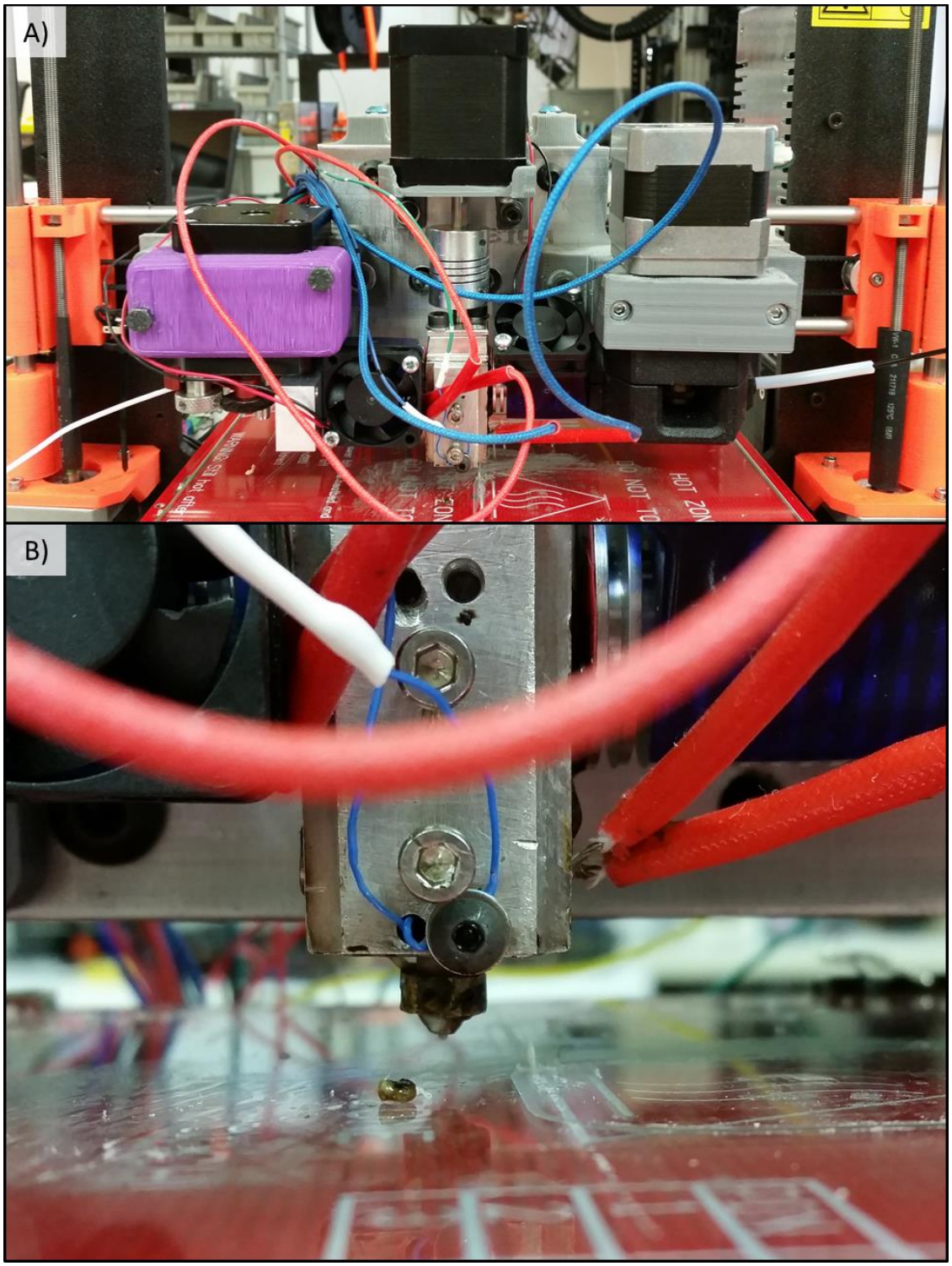

Figure 4.11: A) Front view of MP1 printer configured with Flexion extruder (Diabase Engineering, Longmont, CO) on the left and QR Bondtech extruder on the right. B) Close-up view of mixing hotend. Blue wires connect to thermistor and red wires connect to heater cartridges. Heat sinks surrounding the filament inlets are visible at the top of the image.

Mixing Printer #2 (MP2)

A new printer was developed and designated Mixing Printer #2 (MP2) (*Figure 4.12*). An mk2 printer kit (Prusa Research s.r.o., Prague, Czech Republic) was converted for this application but as development progressed, nearly all components were replaced for the custom requirements of this application. At the core of these changes is a custom hotend providing three filament inlets aligned tangentially to the heated chamber and actuated element. The primary reason for adding a third filament inlet was the removal of the second nozzle on the printer carriage. The soluble filament can then be printed from the same nozzle as the other materials.

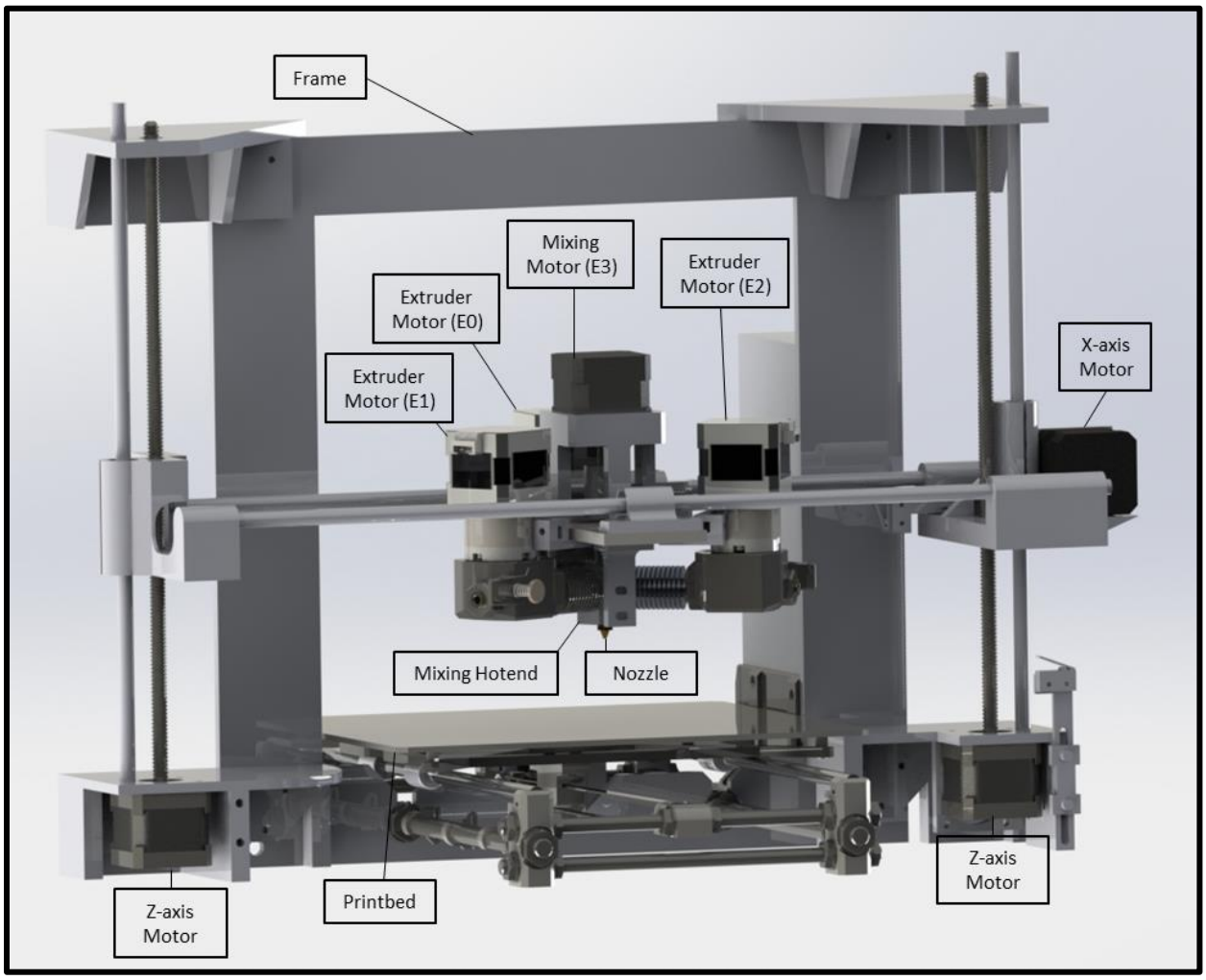

Figure 4.12: Computer model of MP2 assembly including printer mechanics, custom carriages, mixing hotend, and printbed. Inductive sensor is located behind extruder motor E1.

By consolidating all filament inlets into one nozzle, the second nozzle of MP1 was excluded from the design. This design change provided many advantages. Use of only a single nozzle eliminated the reduction in printable volume associated with the distance between the two nozzles. Without multiple nozzles, there is no need to physically align nozzle heights parallel to the print bed, provide software alignment of multiple nozzles in either the firmware or slicing software, nor extend the time to print by including commands to wait for temperature changes as a nozzle enters and exits an inactive state. Print quality also improves by eliminating this nozzle since print defects caused by materials oozing from the inactive nozzle, nozzles impacting components on the print bed, and gaps between printed components due to nozzle misalignment will not occur. Possible disadvantages with this approach include contamination from the third filament and degradation of materials either inside or in contact with the hotend. Specifically, SC filament has a low recommended operating temperature as compared to NF and HTPLA. During operation in the same hotend, the SC filament may be exposed to elevated temperatures and degrade which may cause deposits of burned material in the printed components and filament jams due to degradation of material in the filament inlet.

Components of the carriage design include a mounting bracket for the hotend, X-axis linear bearings, two 60-watt heater cartridges, a 100k ohm thermistor, an induction sensor for bed levelling, three QR Bondtech extruders (Bondtech AB, Varnämo, Sweden), three E3D v6 heatsinks with heatbreaks, an E3D plated copper nozzle, and a stepper motor connected to the actuated element through a flexible coupling. The carriage plate was fabricated using conventional subtractive methods from an extruded 0.25 inch plate of 6061-T6 aluminum.

Components of the structure and printer mechanics were modified to meet printer requirements. An X-carriage, a Z-carriage, and Z-motor mounts were custom design, FFF printed, and integrated into the printer mechanics. The X-motor and Y-motor were upgraded to 2-amp Nema 17 stepper motors and equipped with heatsinks. This motor configuration was necessary to support the torque and associated electrical current necessary for the required accelerations of the

X-carriage and Y-carriage. Belts for the X-axis and Y-axis were upgraded to GT2 fiber reinforced timing belts (Gates Corporate, Denver, CO) to minimize ghosting and printer resonance.

An Azteeg x3 pro control board with eight SureStepr SD2224 stepper drivers (Panucatt Devices LLC, Irvine, CA) was included in this design. The power drawn to run the two 60-watt heaters, the 100-watt heated bed, and the increased current of the stepper motors required that the original kit's 240-watt power supply be upgraded. The replacement power supply was a 12V 480-watt power supply. A 120-mm fan was mounted above the board to prevent the board from overheating. The control board was driven by Repetier-firmware version 1.00 with a custom configuration and some modifications made to the firmware's features. Some notable configuration settings that were modified including mixing printer settings, extruder settings, bed compensation settings, and inductive probe settings.

Revisions made to Mixing Printer Design #2 (MP2_R)

As was the case of MP1, O-ring performance prevented extended operation of MP2. Initially, the inconsistent rate of failures of the seals were attributed to installation error. However, after repeated seal failures were observed and analyzed, it was noted that the conditions of the failed O-ring did not match conventional failure modes described by O-ring manufacturers. Multiple attempts were made to utilize the O-rings and prevent failure including application of high-temperature Krytox 240AD grease (Miller-Stephenson, Danbury, CT) to assist with installation and operation, altering the installation procedure to ensure the O-ring was seated without rolling, and a variety of backup rings materials and configurations. These techniques did not resolve the issues caused by O-ring failure. The suspected cause of premature failure of the O-ring was adhesion between the O-ring and the rotating shaft due to solidification of the process materials within the hotend, though poor alignment of the actuated element and the hotend were not ruled out.

To overcome these limitations, the custom-hotend was revised in design and manufactured with tighter tolerances. Additionally, smoother surface finishes in the gland, on the actuated

element, and within the hotend were provided. The O-ring was replaced by a graphite impregnated PTFE seal energized by stainless-steel springs (Model: SES, Size: -106) (Marco Rubber and Plastics Inc., Seabrook, NH). Other changes were made to the design including an opening made for a cartridge-style thermistor, M5 screws with shoulders for improved alignment between the bearing housing and the hotend, and increased distance between bearings to reduce the rotation of the actuated element. This new design is designated mixing printer #2 with revision (MP2_R) (*Figures 4.13-15*). The MP2_R endured near continuous operation without a seal issue for approximately 120 days.

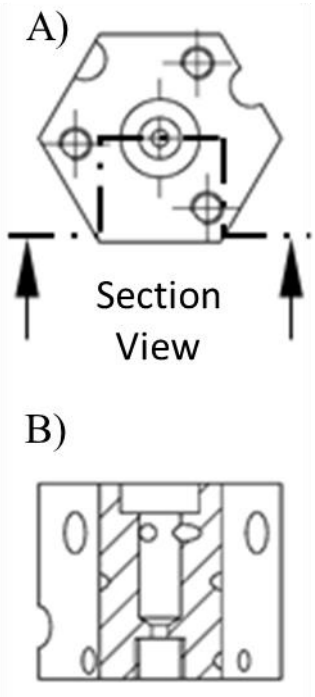

Figure 4.13: Custom hotend for MP2_R. A) Top view of hotend. B) Section view intersecting heated chamber. In view at the top of the hotend is a gland for seating the energized seal between the hotend and the actuated element. At the bottom center of the hotend is a threaded opening for seating a nozzle.

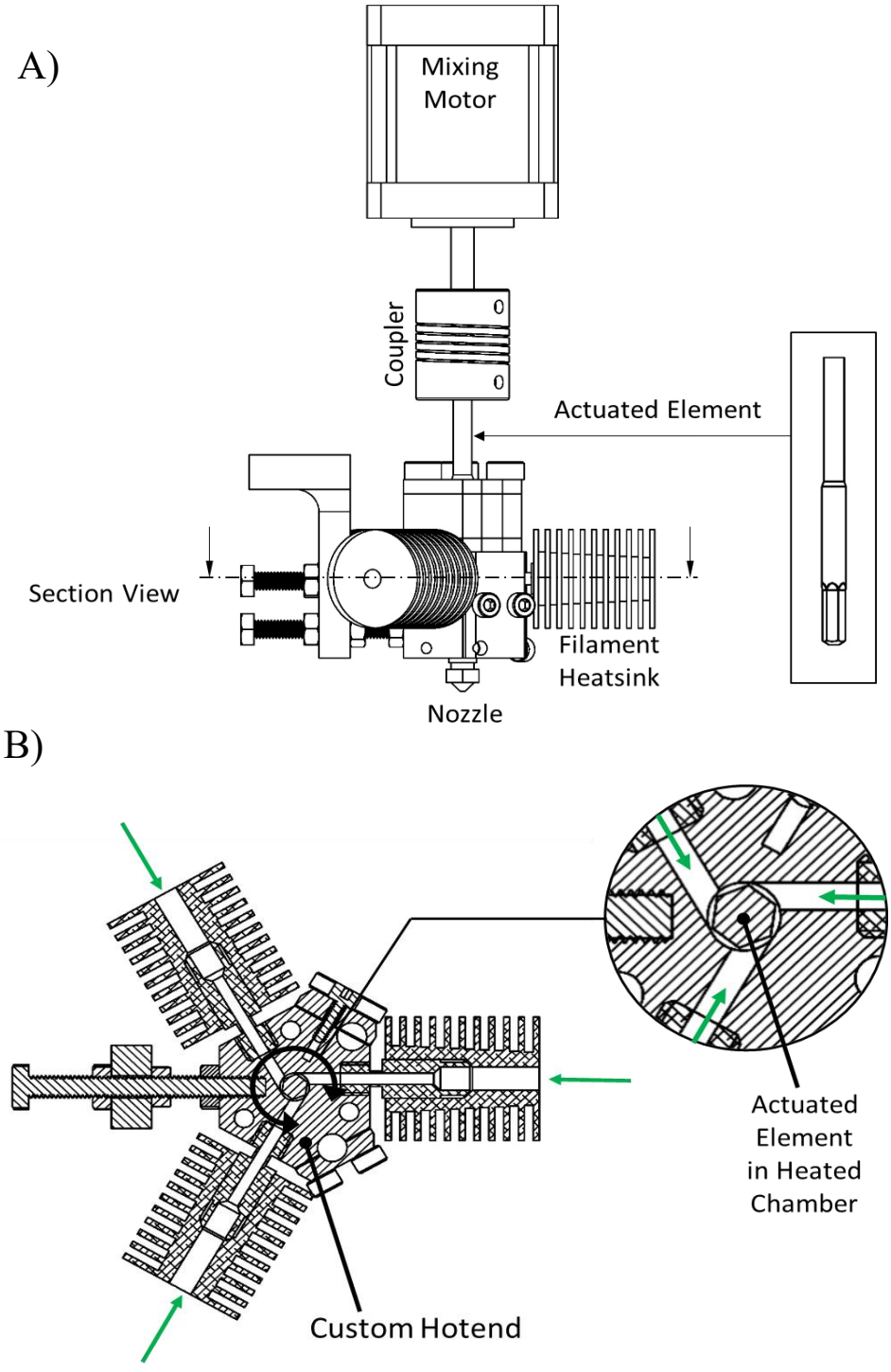

Figure 4.14: A) Assembled view of revised custom hotend. B) Section view as called out on Figure 4.#. Actuated element is configured for material blending and is centered in the hotend's heated chamber. Filament inlets (green arrows) are located tangential to the heated chamber and the actuated element. During operation, the actuated element is rotated counterclockwise to assist with feeding the filament into the hotend.

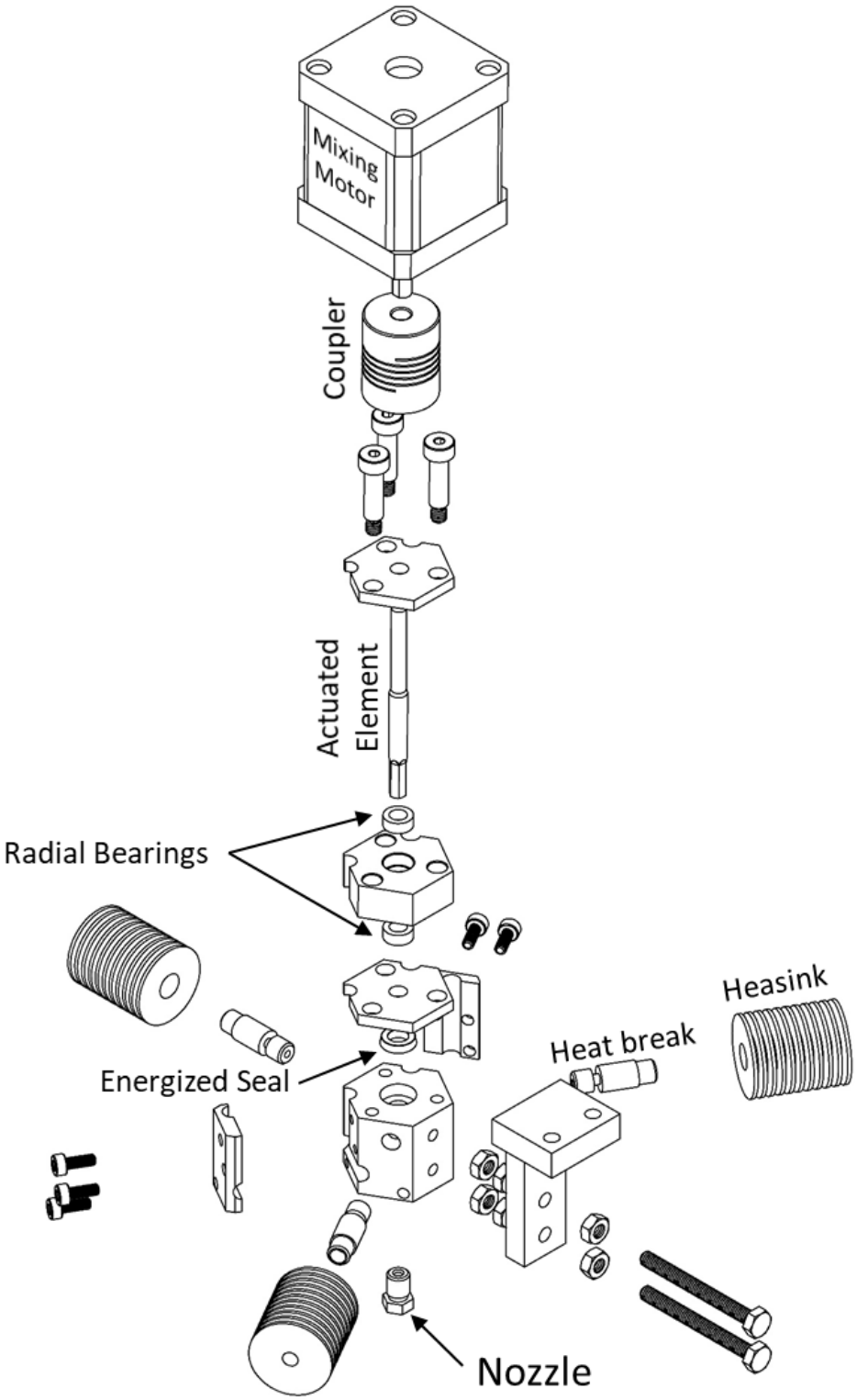

Figure 4.15: Exploded view of revised custom hotend. Energized seal seats into the gland at the top of the heated chamber.

4.3.3 Printer Tuning

Each iteration of the printer design was supported by modifications made to firmware and slicer software to improve print quality. Repetier-Host was used and set to run Slic3r for preparation of print files. Most changes provide general improvement for FFF blending of NF and HTPLA, but some settings are specific for performance of individual printers.

Early tuning determined the necessary motor weights assigned through M163 to achieve homogeneous mixing. The ratio used to achieve homogeneity was six parts mixing motor rotation and one part for total filament extrusion. *Figure 4.16* provides an example of an under mixed printed part fabricated using MP1.

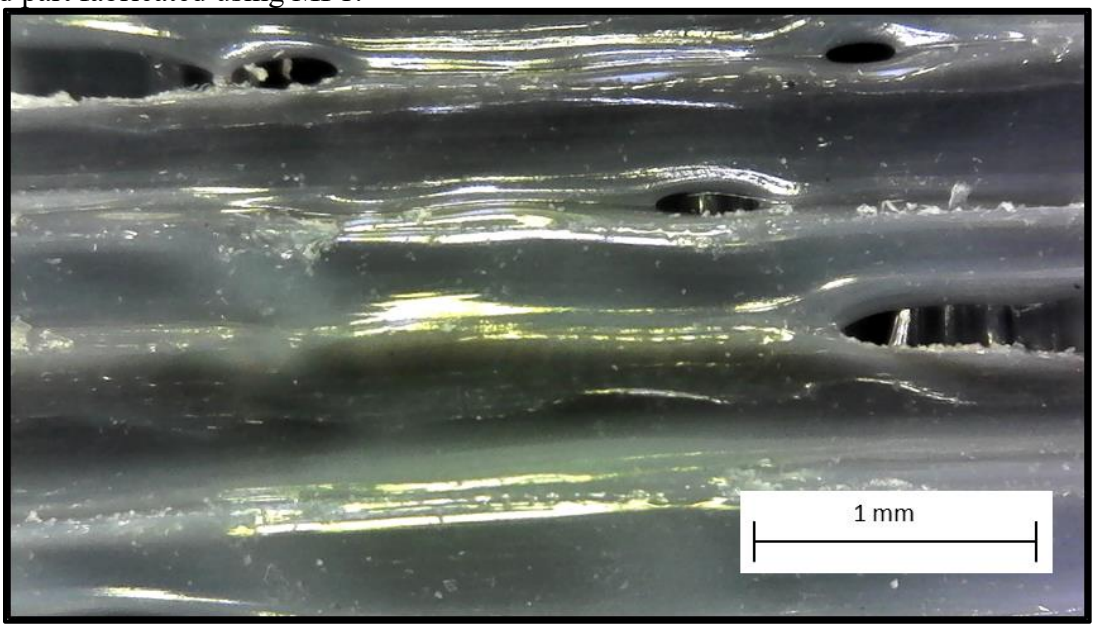

Figure 4.16: Early print with MP1 demonstrating undermixing due to a low M163 weight applied to the mixing motor. This image includes a view of horizontal rasters of printed PLA (black) and NF (white). Variation of composition within single rasters are visible in this test but not after tuning.

Extrusion width was determined by reviewing print previews of a sliced D638 type V specimen (ASTM International 2003). In increments of 0.01 mm, the best extrusion width for reducing gaps was determined to be 0.46 mm. An example of this gap reduction when comparing 0.46 mm and 0.5 mm is provided in *Figure 4.17*.

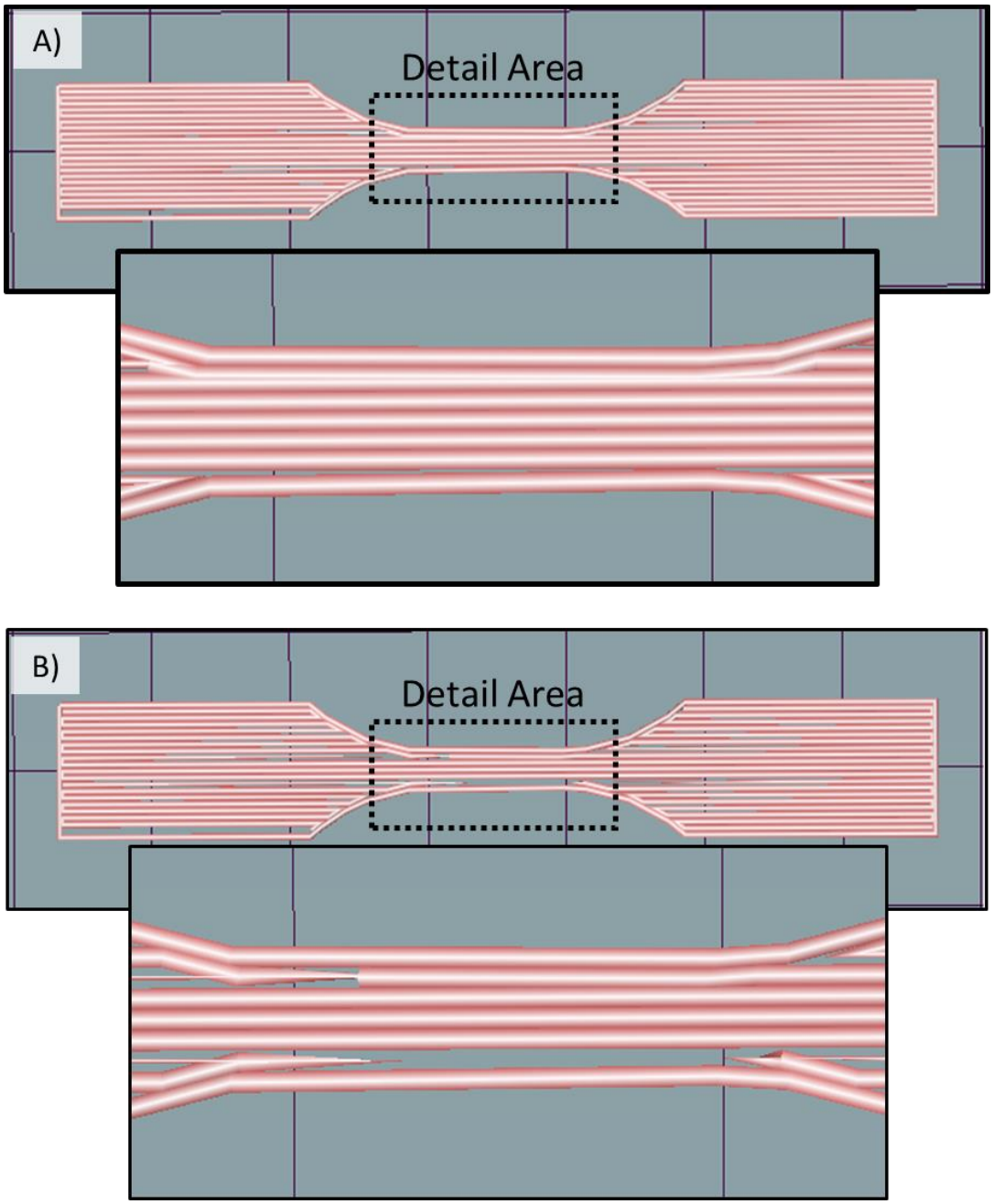

Figure 4.17: Print preview of a single layer from two extrusion width settings for printing a D638 type V specimen. A) Print preview with extrusion width set to 0.46 mm. Note that a small gap is visible between the bottom perimeter and the infill raster above. B) Print preview with extrusion width set to 0.5 mm. Note the large gap between the bottom perimeter and the infill raster above.

Print speed was determined by running prints extruding NF for multiple layers. The print speed of each print was incrementally increased until under-extrusion or filament slipping was

observed. Print speeds of MP1, MP2, and MP2_R are set to 8 mm/s, 22 mm/s, and 18.4 mm/s, respectively (*Table 4.1*).

Table 4.1: Slicer settings determined during tuning

Printer	Nozzle Diameter	Print Speed (mm/s)	Infill (%)	Travel (mm/s)	Extrusion Width	Layer Height
MP1	0.8	8	100	120	0.8	0.4
MP2	0.5	22	100	200	0.46	0.4
MP2_R	0.5	18.4	100	200	0.46	0.2

Initial firmware configurations set steps/mm for printer mechanics and extruder motors as defined by either manufacturer's recommendations or unit conversion calculations that account for drive system configurations. No additional tuning was necessary for printer mechanics, but extruder parameters were further tuned for specific filaments.

Table 4.2: Flow multipliers and nozzle temperatures for tuned compositions

Composition ID	HTPLA (%V)	NF (%V)	Nozzle Temperature (°C)	Flow Multiplier
100%	100.0	0.0	240	7.00
50%	50.0	50.0	240	7.70
25%	25.0	75.0	240	7.18
12%	12.0	88.0	240	7.14
6%	6.0	94.0	240	7.00
3%	3.0	97.0	240	7.00
1.5%	1.5	98.5	240	7.00
0%	0.0	100.0	240	7.00

The manufacturer recommendation is 476.5 steps/mm for a stepper motor driver with 16 microsteps/step running a QR Bondtech extruder. To improve tuning, each extruder was paired with one of the selected materials and adjusted by comparing command displacement to actual filament displacement as measured with calipers. The final tuned settings were determined by review of printed D638 specimens and models with a complex structure. Visual inspection was performed externally and with specimen cut in half with a razor blade. Parts printed with harder compositions were wet sanded as necessary to view gaps in detail. Individual extruders paired with specific filaments were tuned by changing steps/mm for the respective extruder in the firmware. The extruders paired with HTPLA, NF, and SC were set to 419.6, to 484.9 steps/mm, and 466 steps/mm respectively. By using this approach, M163 weights for the extruders are made proportional to the ratio of filament flow. Slicer software flow multipliers for single filament compositions are set to 7.00 to account for the M163 weights for six parts mixing motor rotation and one part filament extrusion. Compositions and corresponding slicer flow multipliers are shown in *Table 4.2*.

During FFF, flexible filaments store more energy between the extruder and nozzle in the hotend than conventional thermoplastics like PLA or ABS. In effect, this stored energy makes changes in flow rate difficult. Filament does not immediately start to flow from a primed nozzle when filament is driven into the hotend, nor does it immediately stop flowing from the nozzle when feed rate is stopped or reversed. As a result, flexible filaments have more defects from oozing, stringing, blobs, and gaps at print seams. Normally, these effects can be mitigated by retraction, but this solution does not work well for flexible filaments. More effective solutions include reduced print speeds, increased jerk and acceleration settings, reduced travel moves across perimeters, and increased travel move speeds. Another way to help combat these defects is integration of linear advance.

Due to the comparatively large volumes of the mixing printer's heated chambers, the flexible filaments store more energy than conventional FFF printers and, without compensation, impart more associated defects. Mixing printer settings to address these defects include changes

to slicer settings included removal of retraction and travel move speed was increased from 120 mm/s to 200 mm/s to reduce these effects and changes to firmware settings as described in *Table 4.3*.

Table 4.3: Firmware settings to reduce flexible filament oozing and stringing

Variable Callout in Firmware	Value	Units
MAX_ACCELERATION_UNITS_PER_SQ_SECOND_X	3000	mm/s^2
MAX_ACCELERATION_UNITS_PER_SQ_SECOND_Y	3000	mm/s^2
MAX_ACCELERATION_UNITS_PER_SQ_SECOND_Z	500	mm/s^2
MAX_TRAVEL_ACCELERATION_UNITS_PER_SQ_SECOND_X	3000	mm/s^2
MAX_TRAVEL_ACCELERATION_UNITS_PER_SQ_SECOND_X	3000	mm/s^2
MAX_TRAVEL_ACCELERATION_UNITS_PER_SQ_SECOND_X	500	mm/s^2
MAX_JERK	20	mm/s
MAX_ZJERK	6	mm/s
EXT0_MAX_ACCELERATION	5000	mm/s^2
EXT0_MAX_START_FEEDRATE	50	mm/s
EXT1_MAX_ACCELERATION	5000	mm/s^2
EXT1_MAX_START_FEEDRATE	50	mm/s
EXT2_MAX_ACCELERATION	5000	mm/s^2
EXT2_MAX_START_FEEDRATE	50	mm/s
EXT3_MAX_ACCELERATION	5000	mm/s^2
EXT3_MAX_START_FEEDRATE	50	mm/s

Visual inspection of specimen printed for tuning revealed gaps between infill and perimeters. These defects were addressed by changing extrusion width to improve coverage by infill and increasing infill/perimeter overlap from 0 mm to 0.25 mm. Tactile review of other test prints were identified to have weak bond strength between regions with different composition. Increased bond strength was apparent after increasing regions/extruder overlap from 0 mm to 0.18 mm.

Miscellaneous modifications to slicer software and printer firmware include tuning parameters for the inductive Z-probe, distortion correction such that first layer printing followed defects in the print bed, probe location for homing the z-axis set to center of the print bed, and print bed temperatures set to 45°C.

4.3.4 D638 Specimen Fabrication and Tensile Tests

Fabrication

D638 type V specimen were fabricated flat on the print bed and aligned with the printer's X-axis for each of the eight compositions described in *Table 4.2.* Three specimens of each composition were printed individually for determination of E, σ_Y, EL%$_Y$, UTS, and EL%$_F$, and three specimens of each composition were printed simultaneously for determination of Poisson's ratio. Fabrication was performed on MP2_R using Repetier-Host and the respective slicer settings in *Table 4.1* and filament settings as described in *Table 4.2*. Skirts were added to print settings to ensure that the nozzle was primed before printing the first layer of each specimen. Composition of each specimen was set by M163 and M164 commands inserted into the start of each print file.

Tensile Tests

Specimen were measured in height and width using calipers before being mounted with GW-XT wedge grips (ADMET Inc., Norwood, MA) in an eXpert 5603 universal testing machine (ADMET Inc., Norwood, MA) (model: eXpert 5603, stroke length: 305 mm, position resolution: 0.057 μm) configured for tensile testing and controlled by MTEST Quattro Material Testing System v5.00.02 (ADMET Inc., Norwood, MA) running on a desktop computer. Grip length was set to 25.4 mm, and load rate was set to a constant rate of 10 mm motor displacement per minute. Data was collected at a rate of 100 Hz including tensile force recorded by an SM-1000 load cell (Interface Inc., Scottsdale AZ) and position recorded by the eXpert 5603's motor encoder and a 3442 axial extensometer (Epsilon Technology Corp., Jackson, WY) (gauge length: 0.3 in., range: +0.50 in. to -0.05 in., linearity: 0.110% F.S., Hysteresis = 0.326% F.S.). Specimen tested for determination of Poisson's ratio were painted with spray paint to produce a speckle pattern to assist

with measurement from a DIC system running Vic-Gauge Image Correlation Software Version 8, build 356 for data collection. DIC by Correlated Solutions Setup: cameras: Point Grey model GRAS-20-S4M-C), camera lenses: Schneider Kreuznach CM120 BK 15 compact (1001960 Xenoplan 1.9/35-0901), dual Flood Lights, Model 900420W by Visual Instrumentation Corp with a single power supply power supply model 201240WA. Post-processing done with VIC-3D Digital Image Correlation Version 7.2.4, build 373. Results were processed to determine E, σ_Y, $EL\%_Y$, UTS, and $EL\%_F$ and resultant fracture surfaces were reviewed optically.

4.3.5 Custom Software for Sorting by Tool and Adding Priming Blocks including Retraction

Transition from one composition to another requires that the material within the hotend must be purged from the current composition to the next. This is further complicated by residual contaminants within the hotend and when printing with a single filament due to contamination from inactive filaments in the hotend. To manage changes in composition, two custom programs were developed in LabVIEW™ version 2014 SP1 (National Instruments, Austin, TX) (*Figures 4.18-20*).

Custom Program for Sorting Print File Content by Tool

A custom program was developed to modify print files so that tool callouts occur in sequential order (Figure 4.19). Sorting a print file by tool is valuable for the addition of priming blocks as it can be configured to reduce contamination through incremental steps from one extreme composition to the extreme opposite composition (e.g. use smaller priming towers to make small changes in composition rather than require large changes in composition and larger priming towers). This program reads the G-code file created by slicer software and copies sections of code from one tool callout or layer change to the next tool callout and rearranges them so that each layer contains sequential tool callouts and associated commands. As the program rearranges the file, it also deletes all travel moves but one before tool callouts.

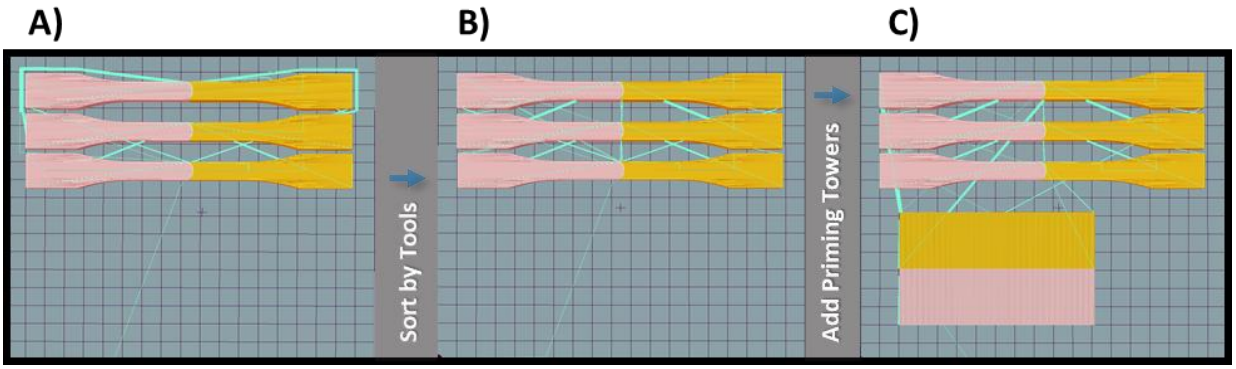

Figure 4.18: Print previews of files for printing interface bond strength specimen. Preview includes print moves for composition 1 (pink), print moves for composition 2 (orange), and travel moves (blue). A) Print file as processed by slicing software. Sequence of printing is optimized for minimal travel moves while reducing travel across perimeters. B) Print file after processing through the custom "sort by tools" software. Sequence of printing per layer is pink and then orange. C) Print file after processing through the "sort by tools" software and the "add priming towers" software. Sequence of printing per layer is pink priming block to pink side of specimens to orange priming block to orange side of specimens.

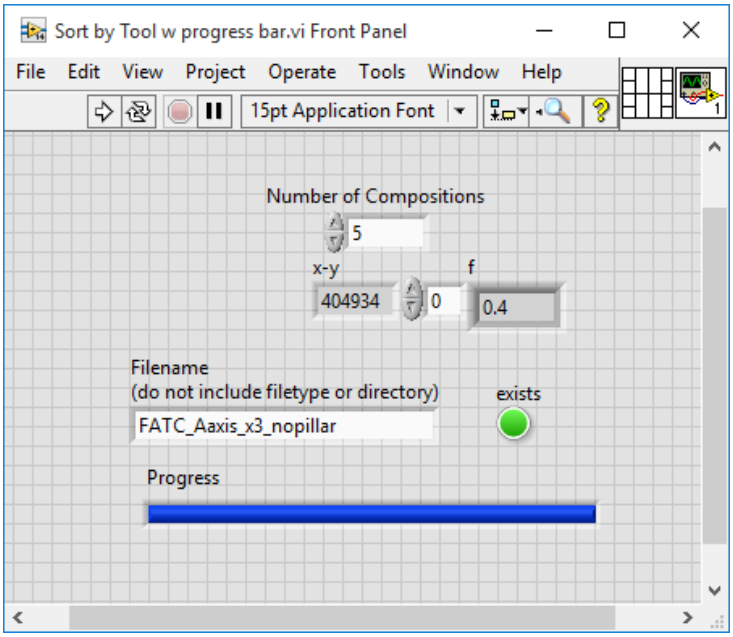

Figure 4.19: User interface of custom program for sorting G-code content by virtual extruder.

Custom Program for Adding Priming Towers and Retraction

A custom program was developed to further process print files already processed by the sort by tool program. This program adds priming towers at the start of each tool change. Priming

towers consist of rectilinear rasters that alternate by layer. Parameters are provided by the user including priming tower length, priming tower depth, location on the print bed, nozzle temperatures, and retraction settings.

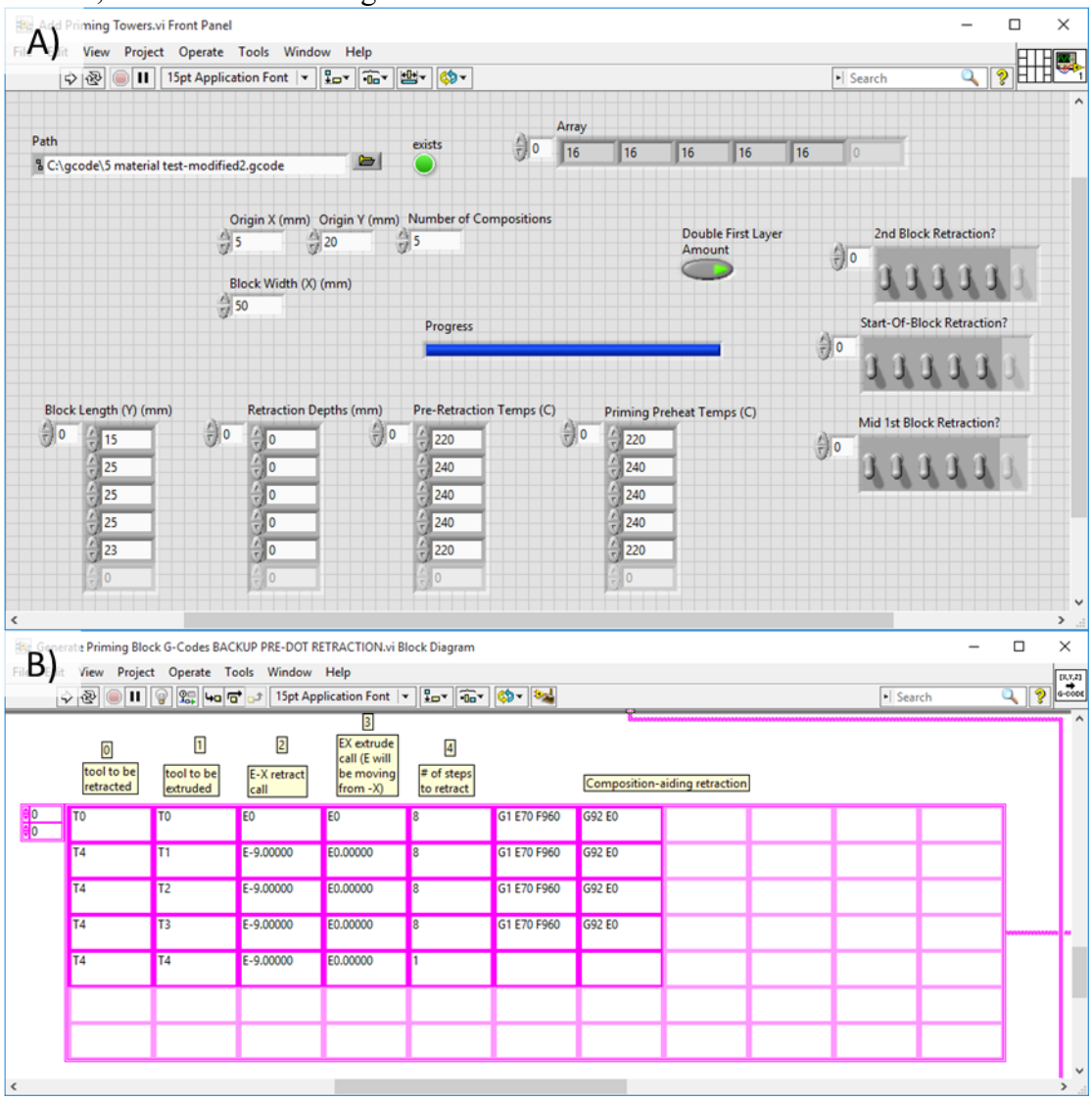

Figure 4.20: Custom program for adding priming towers to print file. A) User interface including options for priming tower dimensions, priming tower location, number of compositions, the addition of retraction, and increased first layer height. B) Array within custom program for control over retraction. Toggles on user interface enable and disable rows of this array.

4.3.5 Interface Bond Strength Tensile Tests

Fabrication

Concave and convex models of the IBS specimen were designed in SOLIDWORKS following the dimensions described by Lauke et al (Lauke, Schüller, and Schneider 2012). The convex model and concave model were aligned in a SOLIDWORKS assembly and exported as STL files. The files were imported in sets of three into Repetier-Host with the specimen flat on the print bed and axially aligned along the printer's X-axis. Convex materials were assigned to virtual extruder "T0" and concave materials were assigned to virtual extruder "T1." Printer settings included M163 and M164 commands for the desired blends of HTPLA and NF with the harder composition to "T0" and softer composition to "T1.". Files were sliced into G-code print files and post-processed using the "Sort by Tool" and "Add Priming Towers" software. IBS specimen were printed with the MP2_R slicer settings in *Table 4.1*, filament settings in *Table 4.2*, and IBS specimen-specific settings for slicer and custom software as shown in *Table 4.4* on MP2_R.

Table 4.4: Slicer and software settings specific to IBS specimen

IBS Composition ID	Composition 1 (Convex)		Composition 2 (Concave)		Priming Tower Dimensions		Retraction	
	HTPLA (%V)	NF (%V)	HTPLA (%V)	NF (%V)	X (mm)	Y (mm)	Comp. 1 (mm)	Comp. 2 (mm)
100 v 0	100	0	0	100	100	30	-11.4	-7.4
100 v 50	100	0	50	50	100	30	0	-7.4
50 v 25	50	50	25	75	100	20	0	0
25 v 12	25	75	12	88	100	20	0	0
12 v 6	12	88	6	94	100	20	0	0
6 v 3	6	94	3	97	100	20	0	0
3 v 1.5	3	97	1.5	98.5	100	20	0	0
1.5 v 0	1.5	98.5	0	100	100	20	-11.4	0

Tensile Tests

IBS specimens were measured in height and width using calipers before being mounted in GW-XT wedge grips within the eXpert 5603 universal testing machine configured for tensile testing and controlled by MTEST Quattro software running on a desktop computer. Grip length was set to 110 mm, and load rate was set to a constant rate of 10 mm motor displacement per minute. Data was collected at a rate of 100 Hz including tensile force recorded by the SM-1000 load cell and position recorded by the eXpert 5603's motor encoder and a 3442 axial extensometer. Results were processed with assistance from finite element analysis and fractography to estimate interface bond strength.

4.3.6 2D Finite Element Analysis of Interface Bond Strength Tests

Finite element (FE) analysis was performed following the methods described by Lauke and Schüller using ANSYS Mechanical APDL 17.0 (ANSYS, Inc., Canonsburg, PA). Verification was performed by inputting Lauke and Schüller's material and geometric parameters to determine agreement between this model and theirs. For each set of IBS tensile tests, an FE analysis matching IBS specimen geometry, elastic modulus and Poisson's ratio of respective compositions, and the maximum force applied during testing was input into the FE model to determine the distribution of stress across the interface.

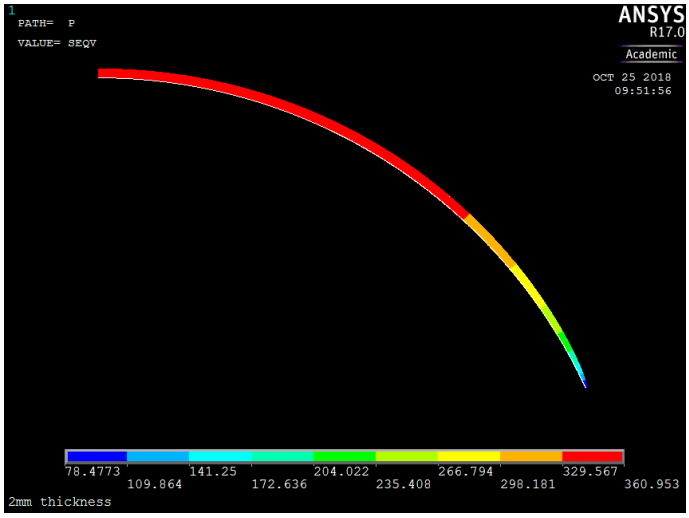

Figure 4.21: Example of elements along nodal path across half of the specimen's interface. Color indicates equivalent stress.

IBS FE Model Development

Geometry of the specimen are imported into ANSYS with 60 mm length, 10 mm width, and 2 mm depth for verifying the model and 7 mm for IBS analysis. Interface is located in the center of the specimen separating the mesh into a convex and concave side. Radii of the interface vary with the analysis being performed. The geometry was meshed with a free mesh set to a mesh size control of 0.5 and refined with decreasing element size in regions near the curved interface (*Figure 4.21*). Structural displacement constraints were applied to the bottom nodes of the specimen, and vertical force was applied across 41 nodes along the top of the specimen. Results from the nodal path along the curved interface was exported from the simulation including corresponding shear stress and normal stress in the vertical direction and horizontal direction. Results were also converted from stress in cartesian coordinates to stress in polar coordinates with the interface center of curvature to better represent loads relative to the interface surface.

Model Verification

The model was verified to match results from Lauke et al. by applying the parameters and inputs from their study to our model. Four geometries and meshes were generated with 2 mm depth, and radii 5.05, 5.50, 7.50, and 10.00 to determine the stress concentration factors at the center of the interface for normal stress in the vertical direction. The material on the convex side of the interface was assigned an elastic modulus of 3,000 MPa with a Poisson's ratio of 0.49, and the material on the concave side of the interface was assigned an elastic modulus of 330 MPa with a Poisson's ratio of 0.35. Vertical load was chosen arbitrarily as the results were normalized by dividing results by the total force and multiplied divided by the cross-sectional area.

Analysis of experimental IBS tests

Parameters from IBS tensile tests were applied to the FE model including maximum force, an interface radius of 5.5 mm, and 7 mm depth. Elastic moduli and Poisson's ratios as determined from experimental D638 tensile tests were applied to the respective concave and convex sides of the interface.

4.4 Results

4.4.1 Preliminary Tests

Print quality and reliability increased with printer development, and visual inspection of printed materials observed improved blending by fine tuning material selection, priming blocks, mixing rod rotation, and retraction.

Conventional FFF

The methods and techniques utilized in this study were iteratively developed in response to observations from conventionally printed specimen. One such investigation into FFF was printing a model of a human patella and associated cartilage, which was printed using ABS filament and an ABS-SEBS blend. Testing revealed that the ABS-SEBS mixture had high friction during and after printing. Printer performance was diminished due to difficulty extruding the filament through the hotend. Despite printing with a direct drive system, the ABS-SEBS filament had to be printed at 285°C, which promoted oozing during printing. By adding a priming tower and an ooze shield to the print settings, the negative effects of oozing were mitigated, and a quality print was achieved (*Figure 4.22*). Such high friction filaments would be difficult to extrude through a mixing printer and were excluded from future studies.

Another early iteration of testing printed the ACL and PCL with femoral and tibial bony islands printed in ABS and NF (Figure 4.2). The hotend temperature setpoint was 230°C for ABS and 245°C for NF. The temperature used for NF exceeded manufacturer recommendations, but this setpoint along with other considerations were necessary due to the limitations of this printer. The Bowden extruders introduce undesirable effects including friction in the 4mm PTFE, guide tube and energy storage due to filament compression during extrusion. The cumulation of these effects can cause delayed extrusion and print failure due to filament buckling.

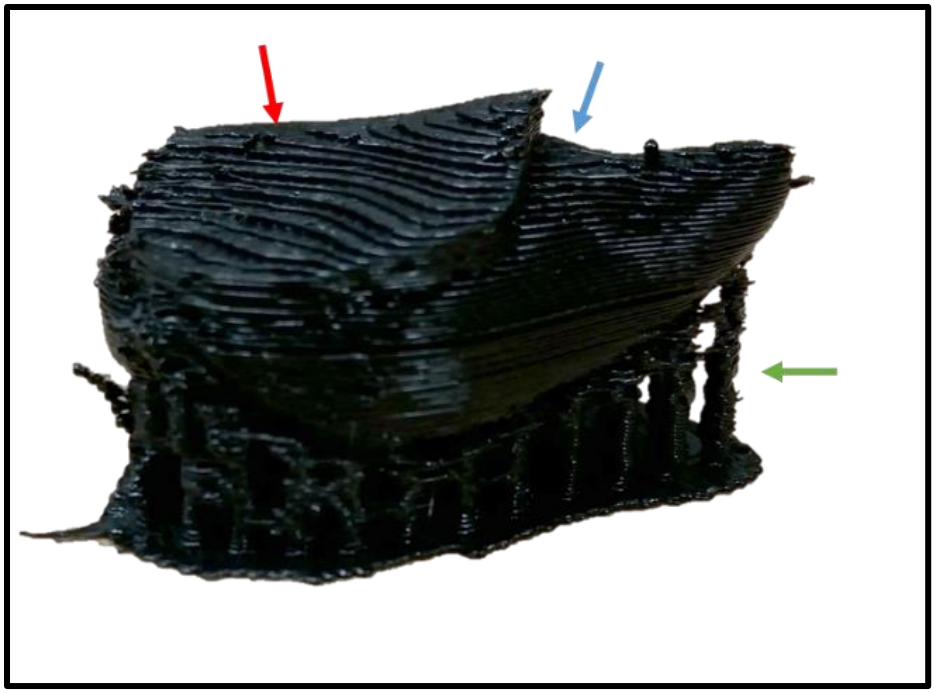

Figure 4.22: Patella with patellar cartilage printed in ABS and ABS/SEBS mixture. Red arrow indicates patellar cartilage printed in ABS/SEBS composition. Blue arrow indicates patella printed in ABS. Green arrow indicates support structure printed in ABS.

Three identical specimens were qualitatively evaluated through hand-held manipulation, which demonstrated ligament restraint of tibial anterior/posterior translation, ligament wrapping in the femoral notch, and a large but resistant range of motion for flexion/extension Catastrophic failure of the specimen was observed at the interface between the Tibia and ACL. This mode of failure highlighted the risk that synthetic tissues produced through FFF may be limited by stress concentrators developed between soft and rigid materials and/or weak bond strength between these materials, which prompted the evaluation of

Results from Mixing Printer Pilot Studies

Early studies using MP1 confirmed enough miscibility between materials to provide effective mixing. This was further confirmed to allow control of material stiffness by printing springs with varying composition (*Figure 4.23*).

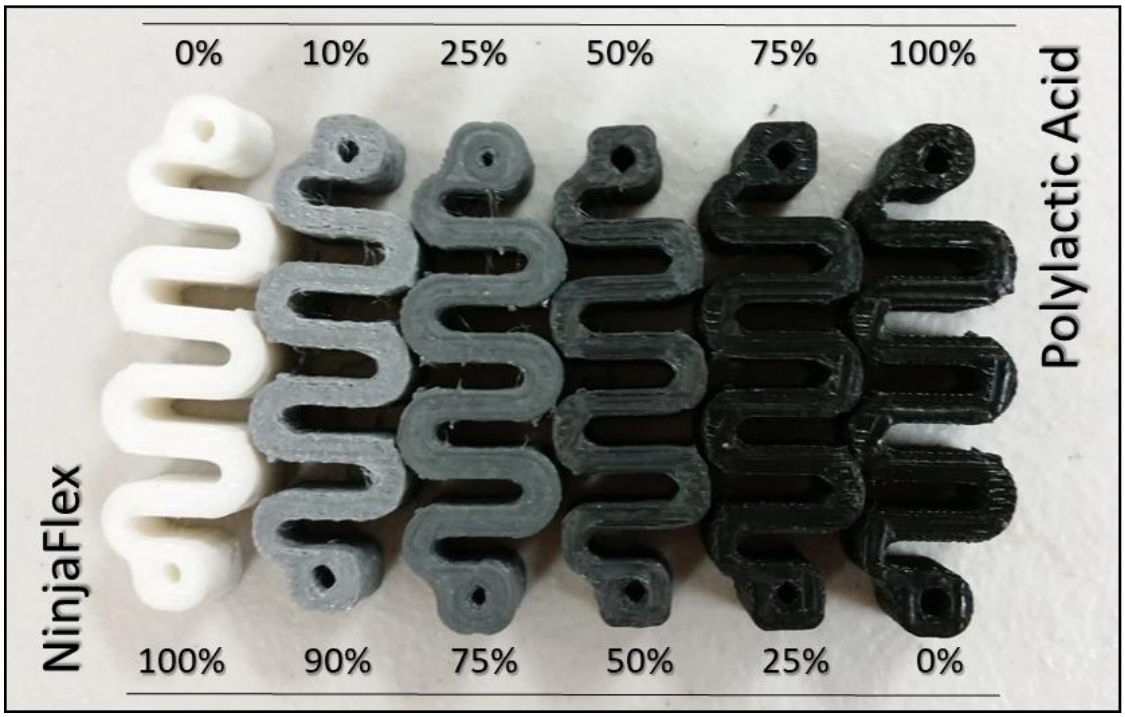

Figure 4.23: Springs printed by MP1 with varying composition of NF and PLA. Specimen on the far left (white) is composed of pure NF and is easily deformed. Composition of the springs increases in composition of PLA from left to right. Specimen on the far right (black) is composed of pure PLA. Stiffness increases to the right as PLA composition also increases.

4.4.2 D638 Tensile Test Results

Results from the first set of D638 tensile tests are summarized in *Table 4.5* including E, σ_Y, EL%$_Y$, UTS, and EL%$_F$. None of the specimens with compositions 0%, 1.5%, or 3% failed during testing. Specimen 1 of composition 6% broke during testing but specimens 2 and 3 did not. It was noted that specimen 1 of composition 6% was unintentionally held in place for the longest time for all specimen during extensometer removal. Specimens with compositions 12%, 25%, 50%, and 100% broke during tensile testing. Mean UTS by composition is shown in *Figure 4.24*. Mean EL%$_F$ is shown in *Figure 4.25*. Mean σ_Y by composition is shown in *Figures 4.26-27*. A non-linear regression fit was applied to mean σ_Y by composition and is shown in *Figure 4.27*. Mean EL%$_Y$ by composition is shown in *Figure 4.28*. Mean E by composition is shown in *Figures 4.29-30*. Mean σ_Y by composition and is shown in *Figure 4.27*. Mean EL%$_Y$ by composition is shown in *Figure 4.28*. Mean E by composition is shown in *Figures 4.29-30*. A non-linear

Table 4.5: Tensile test results for each D638 specimen tested for modulus of elasticity, yield stress, % elongation at yield, ultimate tensile stress, and % elongation at failure

Composition (%v HTPLA)	Specimen	Dimensions (mm)		Modulus of Elasticity (MPa)			Yield Stress (MPa)			% Elongation at Yield			Ultimate Tensile Stress (MPa)			% Elongation at Failure		
		Width	Height		Mean	SD		Mean	SD		Mean	SD		Mean	SD		Mean	SD
0%	1	3.52	3.23	17.8	17.3	0.66	0.76	0.84	0.07	4.42	5.00	0.50	>33.8	>34.7	Unk.	>165	>165	Unk.
	2	3.40	3.23	17.4			0.88			5.20			>35.3			>165		
	3	3.44	3.24	16.5			0.87			5.36			>34.9			>165		
1.50%	1	3.40	3.21	21.4	20.8	0.63	0.60	0.53	0.07	2.96	2.64	0.29	>35.6	>35.3	Unk.	>165	>165	Unk.
	2	3.43	3.25	20.9			0.47			2.39			>35.2			>165		
	3	3.48	3.22	20.2			0.50			2.58			>35.1			>165		
3%	1	3.44	3.23	33.9	39.2	4.92	0.87	0.82	0.07	2.68	2.28	0.41	>36.7	>36.4	Unk.	>165	>165	Unk.
	2	3.30	3.25	43.6			0.74			1.85			>37.4			>165		
	3	3.51	3.23	40.0			0.86			2.31			>35.2			>165		
6%	1	3.35	3.25	76.5	78.3	3.22	1.83	1.79	0.06	2.56	2.48	0.17	39.2	>40.3	Unk.	>165	>165	Unk.
	2	3.33	3.21	82.1			1.73			2.28			>40.5			>165		
	3	3.30	3.22	76.4			1.82			2.59			>41.3			>165		
12%	1	3.68	3.23	139	151	10.1	3.27	3.40	0.13	2.53	2.44	0.09	36.2	36.7	1.84	>165	>165	Unk.
	2	3.40	3.24	157			3.53			2.42			38.7			>165		
	3	3.58	3.23	155			3.40			2.36			35.1			>165		
25%	1	3.53	3.24	335	332	15.2	6.84	6.61	0.20	2.29	2.21	0.10	33.8	32.8	1.26	>165	>165	Unk.
	2	3.47	3.26	345			6.53			2.09			31.4			>165		
	3	3.52	3.24	315			6.46			2.25			33.1			>165		
50%	1	3.37	3.32	1280	1219	65.7	15.2	16.2	1.60	1.40	1.54	0.20	23.6	23.7	0.37	104	121	20.3
	2	3.40	3.28	1149			18.1			1.77			24.1			143		
	3	3.40	3.31	1228			15.4			1.46			23.4			115		
100%	1	3.30	3.24	3428	3483	204	51.7	52.0	4.51	1.69	1.68	0.22	66.2	66.8	0.58	3.14	3.22	0.07
	2	3.27	3.27	3313			56.6			1.89			66.7			3.25		
	3	3.29	3.25	3709			47.6			1.46			67.4			3.27		

regression fit was applied to mean E by composition is shown in *Figure 4.30*. Representative stress-strain diagrams for these tests are shown on *Figures 4.32-34*, and representative fracture surfaces from these tests are shown on *Figures 4.36-37*. Brittle fracture surfaces of specimens with composition 100% were observed. Fracture surfaces of compositions 12%, 25%, and 50% were ductile and had dense fibril formation on the facture surface. The single specimen of 6% composition failed under conditions of plastic deformation but did not demonstrate the same density of fibril formation as observed in the 12%, 25%, and 50% compositions.

Mean Poisson's ratio by composition was determined from the second set of D638 tensile tests as shown in *Figure 4.31*. Graphs presentative of axial strain vs. transverse strain from the tests are shown in *Figure 4.35*.

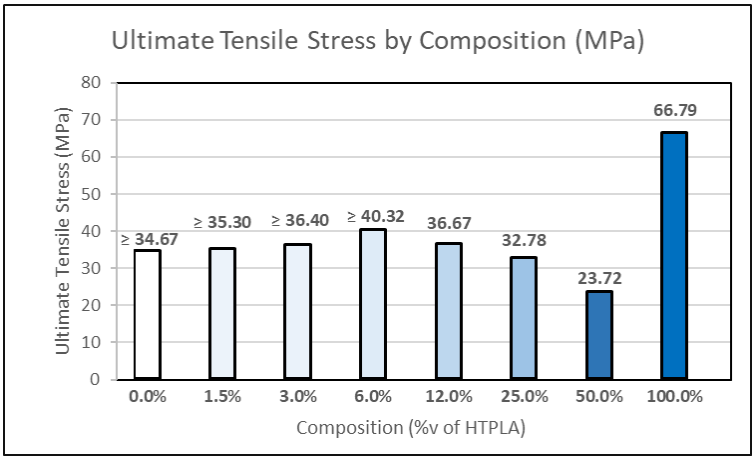

Figure 4.24: Average ultimate tensile stress for tested compositions. No specimens with 0%, 1.5%, or 3% composition failed during tensile tests, and one of three specimens with 6% composition failed during testing. Ultimate tensile stress was reported as greater or equal to the maximum stress measured during testing.

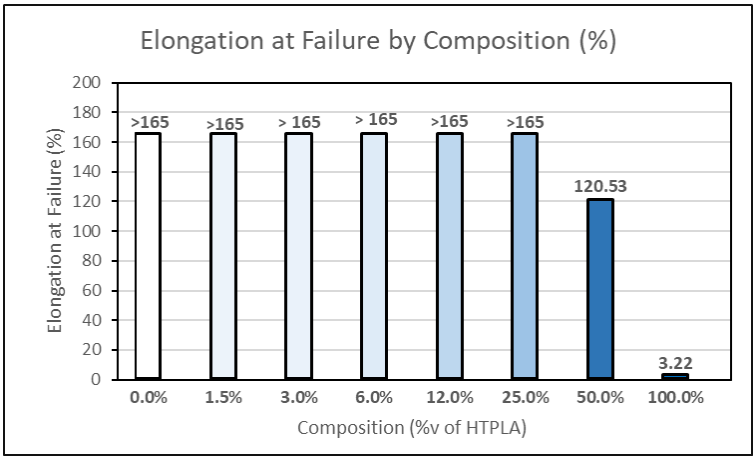

Figure 4.25: Average elongation at failure for tested compositions. No specimens 0%, 1.5%, or 3% with composition failed during tensile tests, and two of three specimens with 6% composition failed during testing. Elongation at failure for these compositions was reported as greater than the maximum elongation of the extensometer.

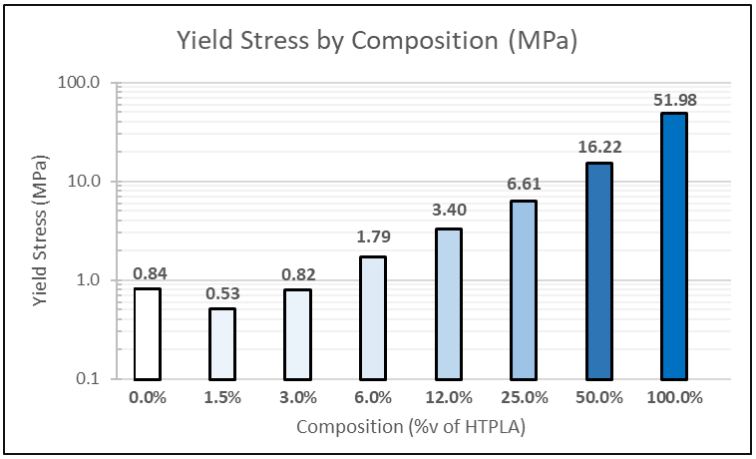

Figure 4.26: Average yield stress for tested compositions.

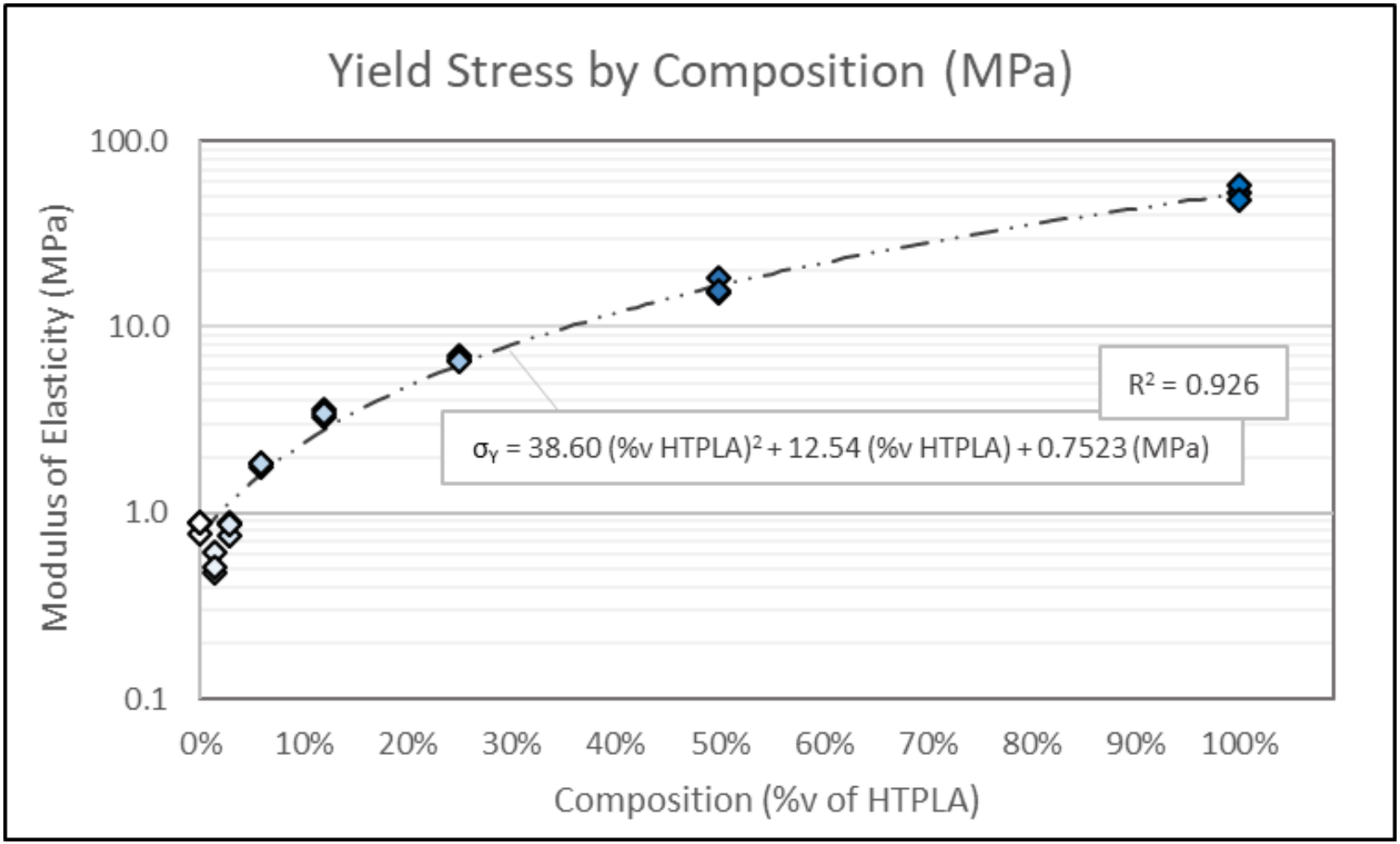

Figure 4.27: Yield stress by composition with a nonlinear regression fit.

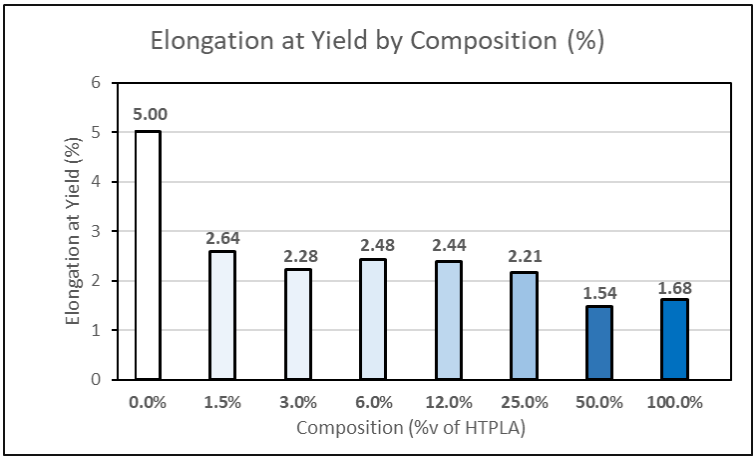

Figure 4.28: Average elongation at yield for tested compositions.

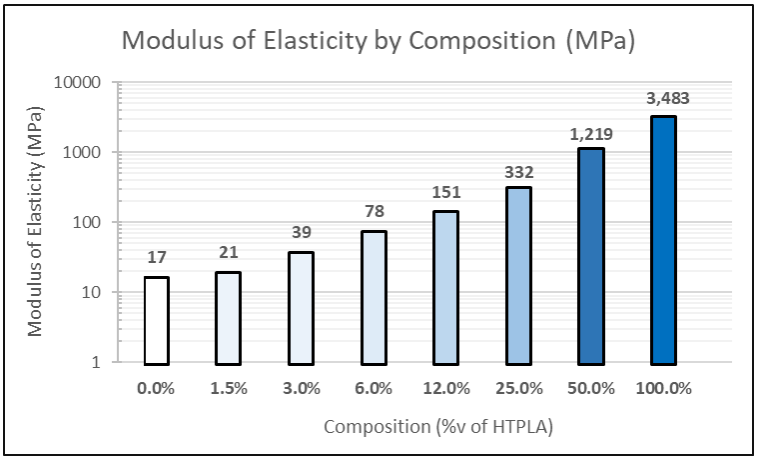

Figure 4.29: Average modulus of elasticity for tested compositions.

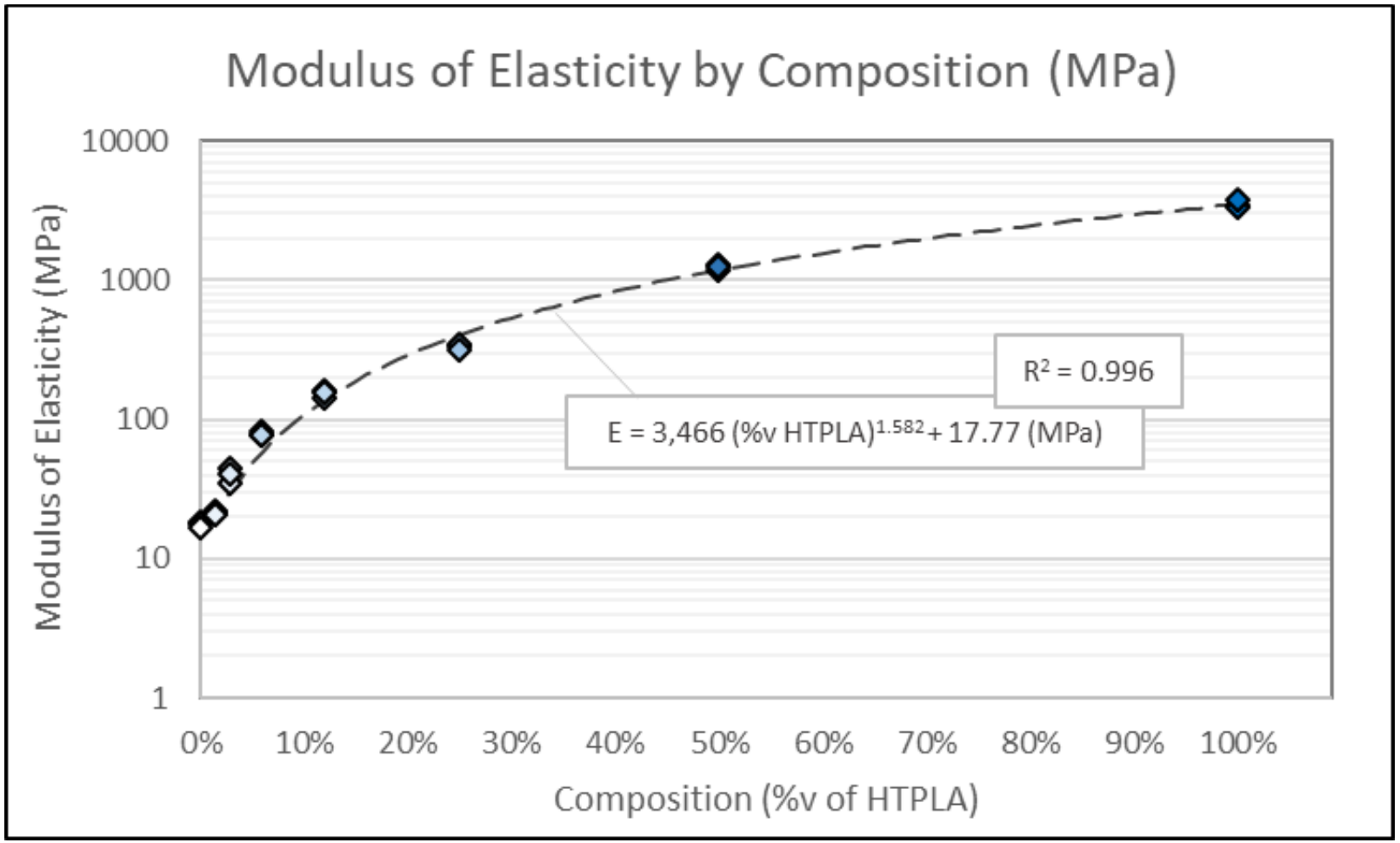

Figure 4.30: Modulus of elasticity by composition for tested specimen with nonlinear regression fit.

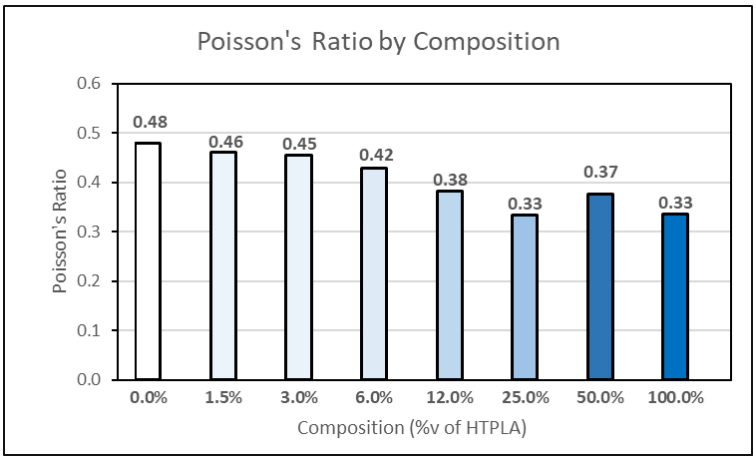

Figure 4.31: Average Poisson's ratio for each composition.

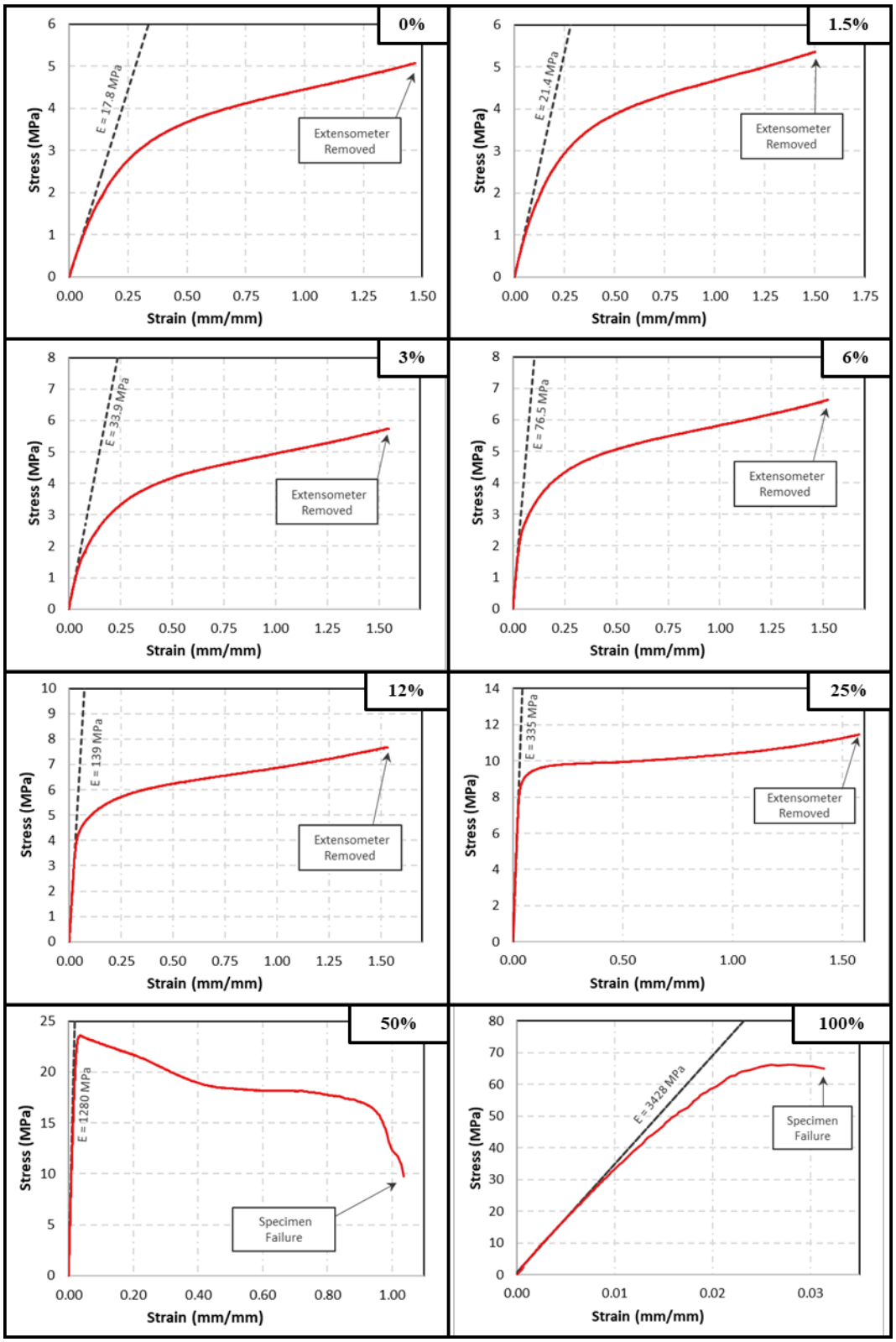

Figure 4.32: Stress vs. strain for specimen 1 of each tested composition as recorded by an extensometer.

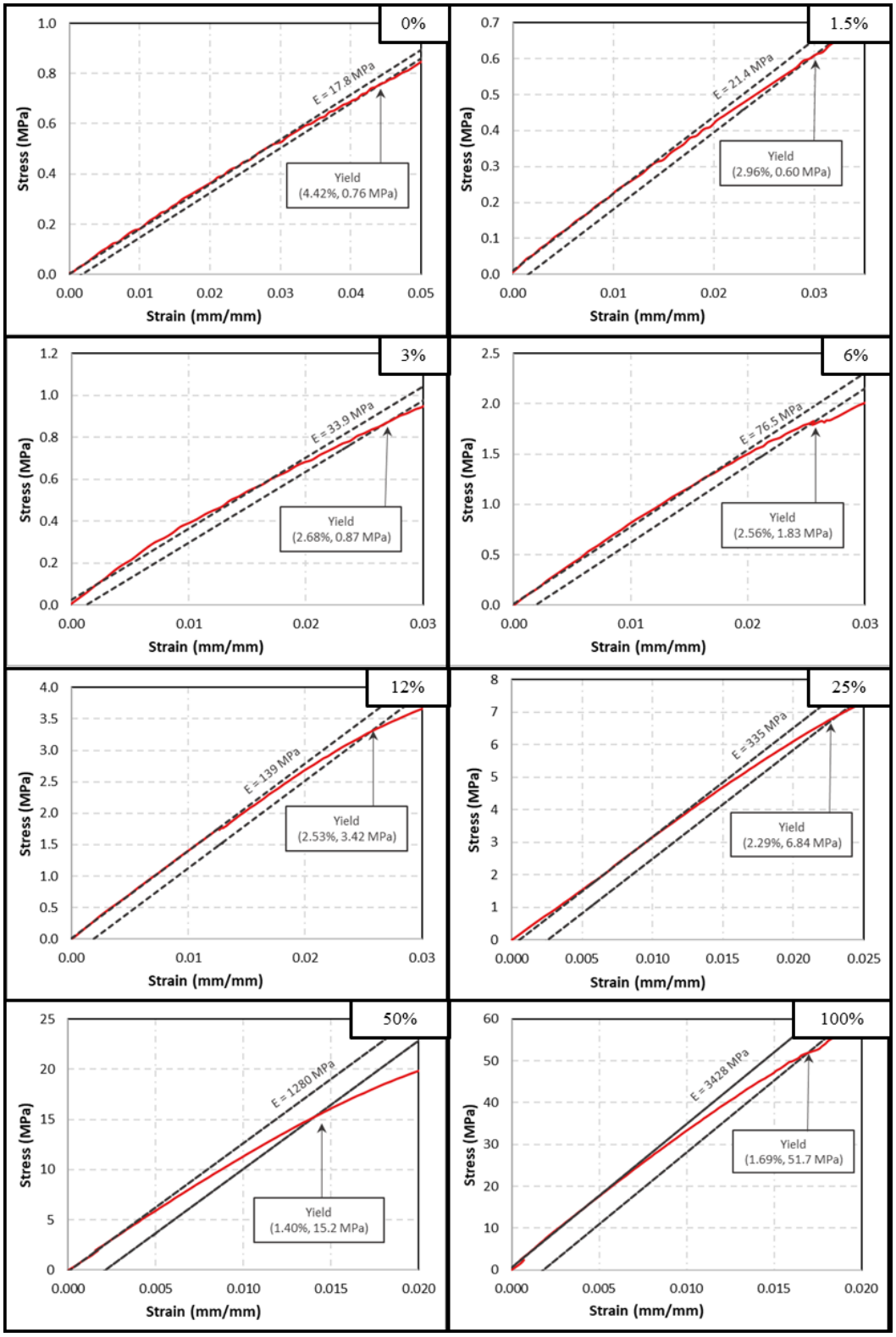

Figure 4.33: Stress vs. strain for specimen 1 of each tested composition as recorded by an extensometer. Scale provides detail of yield stress and percent elongation at yield determined using 0.2% offset method.

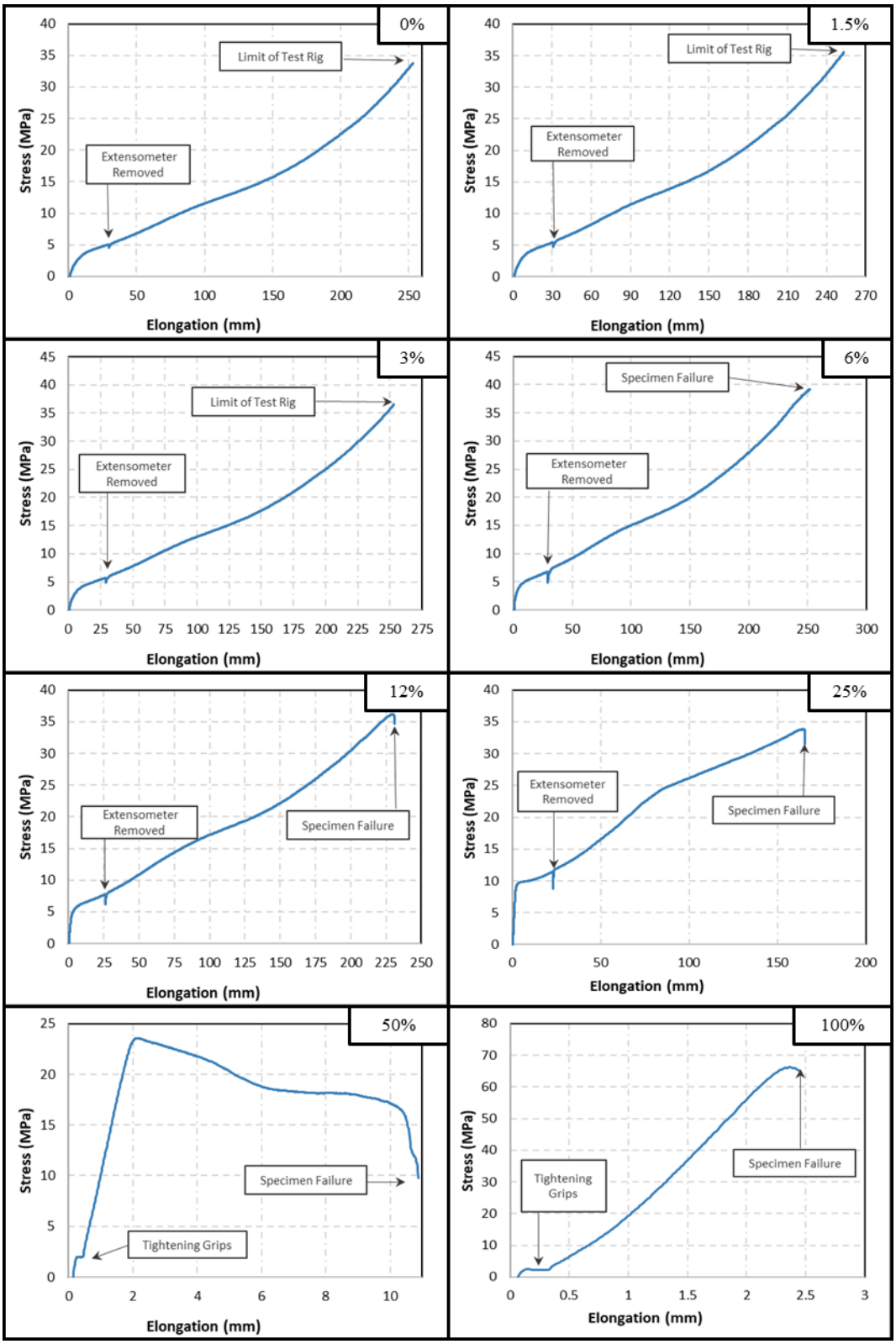

Figure 4.34: Stress vs. elongation for specimen 1 of each tested composition as recorded by the tensile test motor encoder.

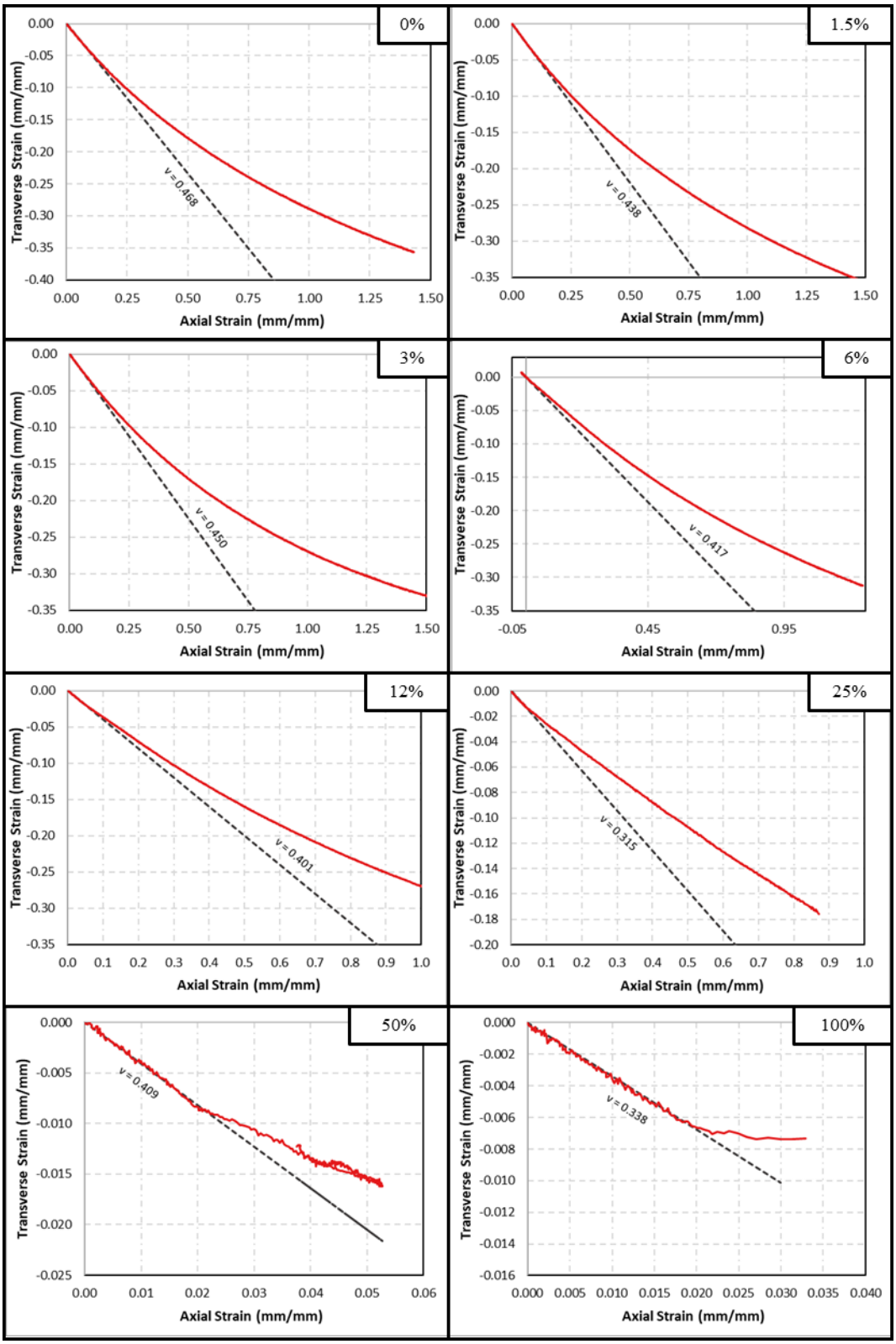

Figure 4.35: Transverse strain vs. axial strain for specimen 1 of each composition. Tangent line represents slope and curve fit for determination of Poisson's ratio

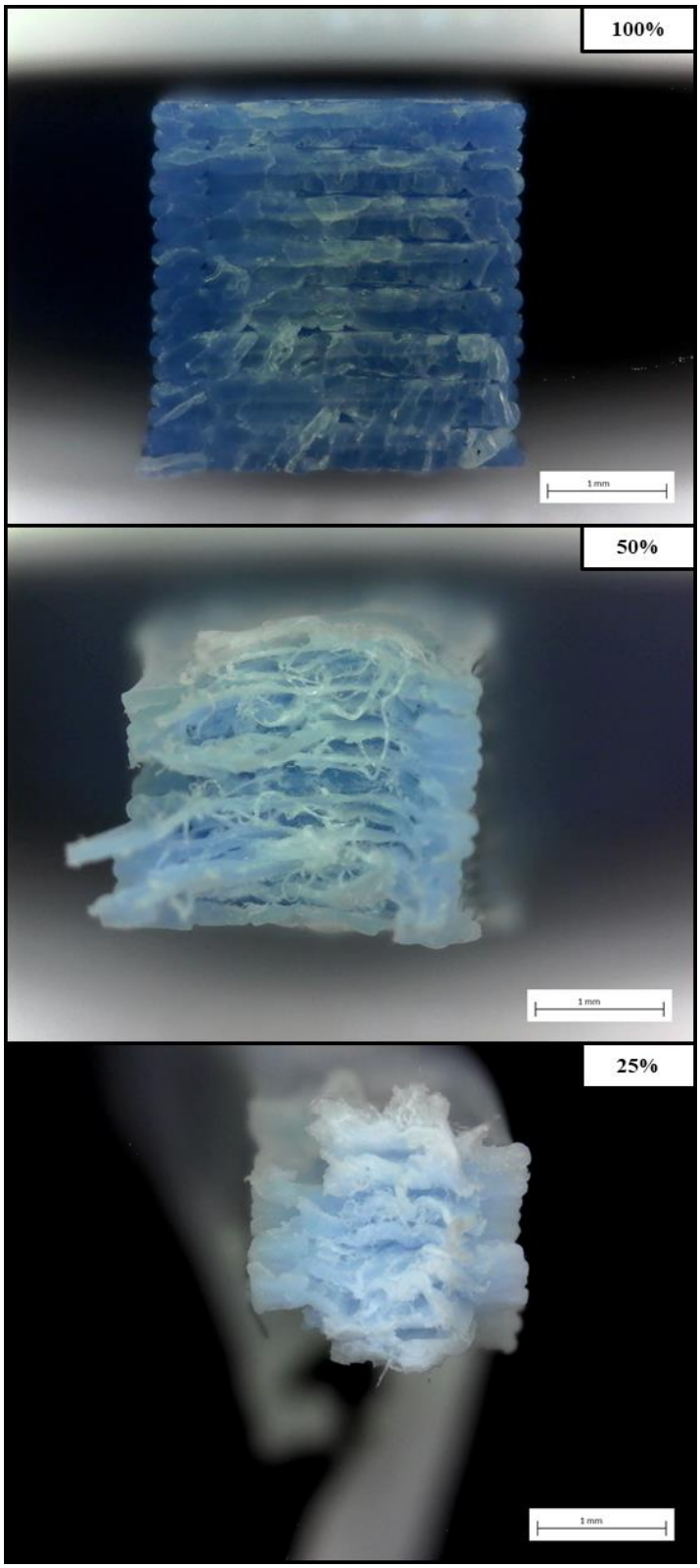

Figure 4.36: Representative fracture surfaces of tensile specimen with compositions 100%, 50%, and 25%. Necking on composition 50% is visible.

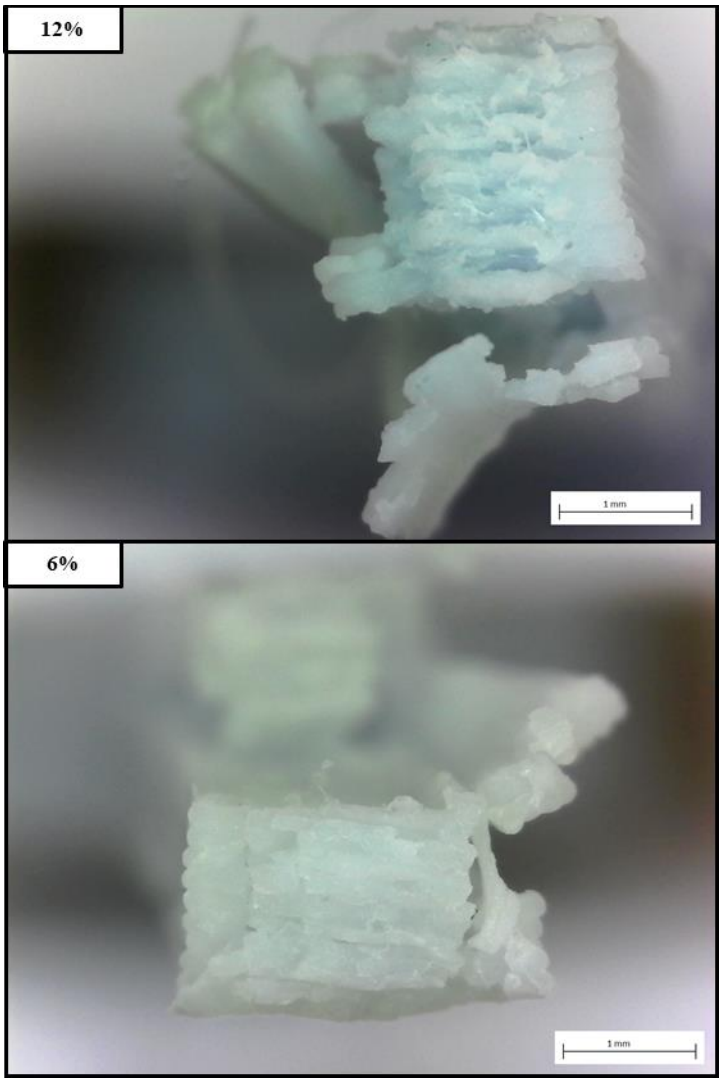

Figure 4.37: Representative fracture surfaces of tensile specimen with composition 12%. One specimen with 6% composition failed and during testing.

4.4.3 IBS Tensile Test Results

Results from tensile tests of IBS specimens are shown in *Table 4.6*. Mean maximum force by interface composition are shown in *Figure 4.38*. Graphs representative of force vs. elongation are shown in Figures *4.39-40*. Specimens with compositions 1.5v0, 3v1.5, 6v3, and 12v6 did not break during tensile testing, and specimens with compositions 25v12, 50v25, 100v50, and 100v0 did break during tensile testing. Representative top views of specimen interfaces that did not break are shown on *Figure 4.41*. Representative fracture surfaces of compositions 25v12, 50v25, 100v50, and 100v0 are shown on Figures 4.42-45.

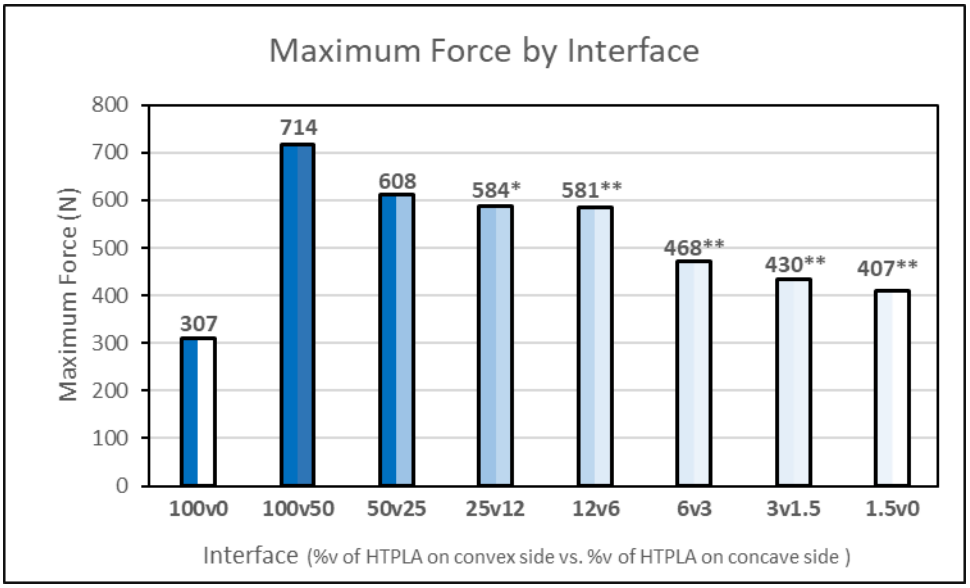

Figure 4.38: Average maximum force recorded during tensile tests of IBS specimen. Specimen with interfaces between 25% and 12% compositions as indicated by * did not fail at the interface. Interfaces between 12% and 6%, 6% and 3%, 3% and 1.5%, and 1.5% and 0% compositions as indicated by ** did not fail during tensile tests.

Table 4.6: Tensile test results for each IBS specimen tested for modulus of elasticity, yield stress, % elongation at yield, ultimate tensile stress, and % elongation at failure

Interface (Convex %v HTPLA vs. Concave %v HTPLA)	Specimen	Maximum Force (N)			Break	
		Specimen	Mean	SD	Y/N	Location
1.5v0	1	409	407	3.17	No	N/A
	2	403				
	3	409				
3v1.5	1	427	430	3.45	No	N/A
	2	434				
	3	430				
6v3	1	466	468	2.15	No	N/A
	2	467				
	3	470				
12v6	1	580	581	1.42	No	N/A
	2	582				
25v12	1	686	640	48.16	Yes	Within Concave Material
	2	644				
	3	590				
50v25	1	609	608	1.55	Yes	Interface
	2	608				
	3	606				
100v50	1	615	714	86.30	Yes	Interface
	2	775				
	3	752				
100v0	1	329	307	21.44	Yes	Interface
	2	286				
	3	307				

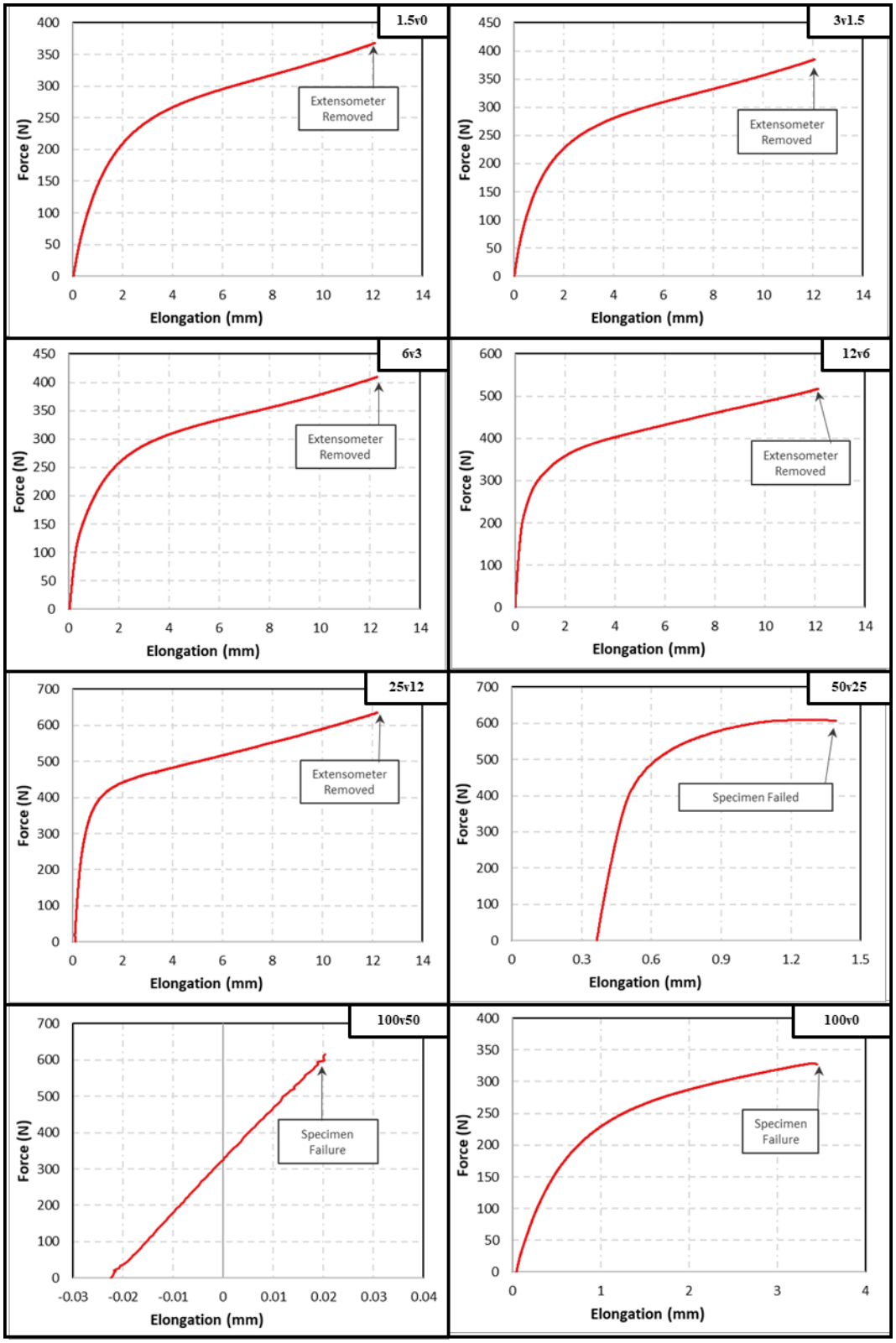

Figure 4.39: Force vs. elongation for specimen 1 of each interface type as determined using an axial extensometer.

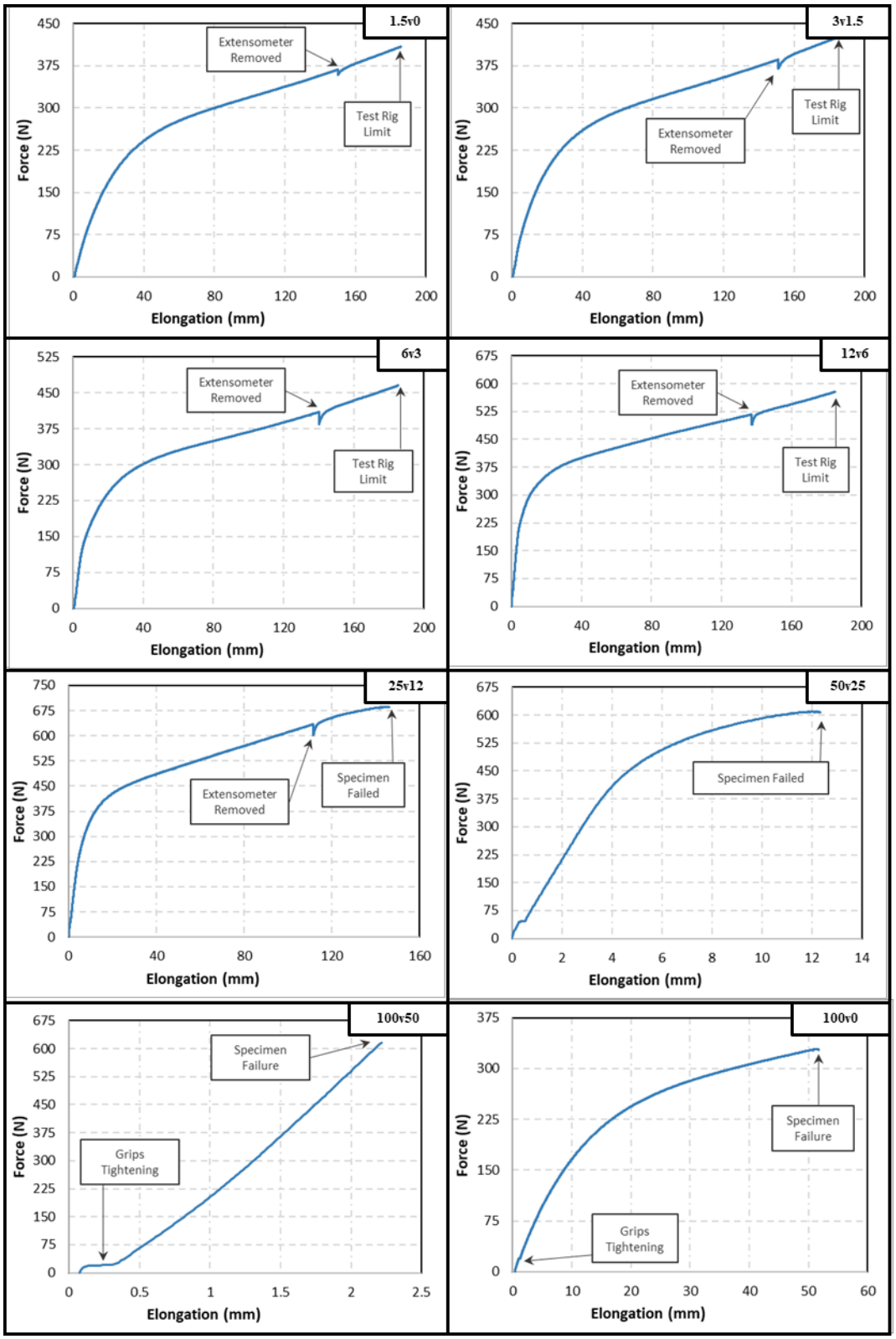

Figure 4.40: Force vs. elongation for specimen 1 of each interface type as recorded by the tensile test motor encoder.

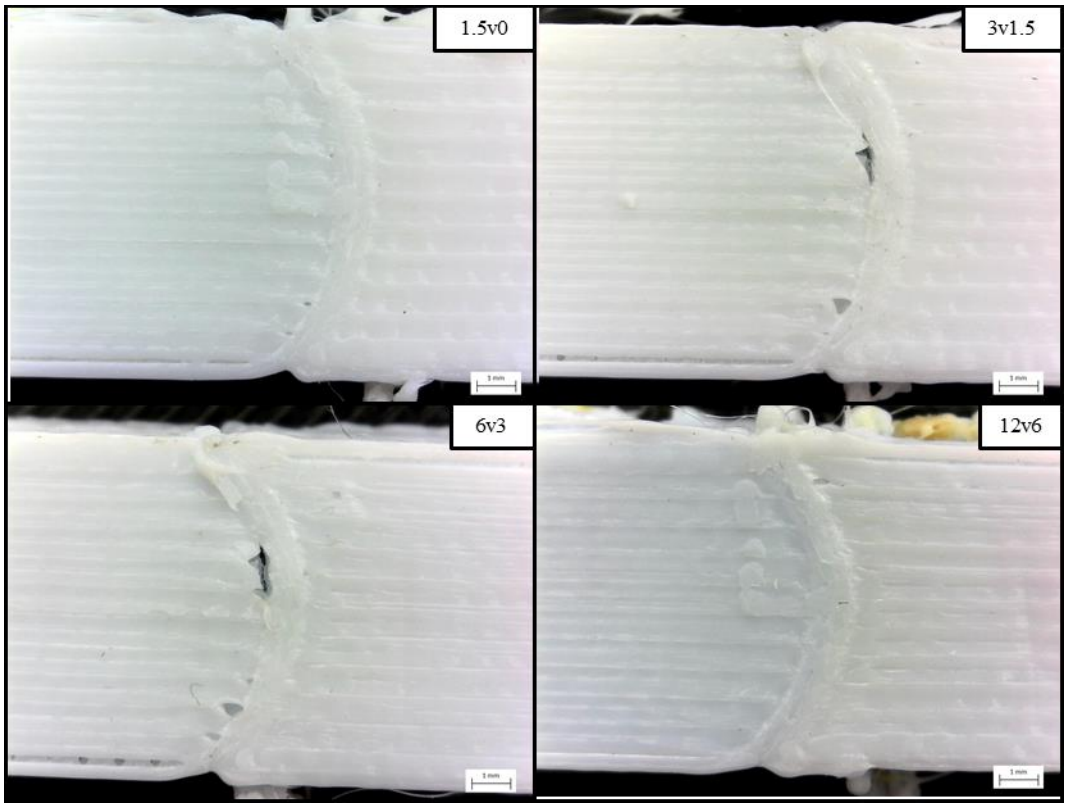

Figure 4.41: Top view of IBS specimens #1 for interfaces between compositions 1.5% and 0%, 3% and 1.5%, 6% and 3%, and 12% and 6% after testing. None of the specimen with these arrangements failed during testing. Some fractures are visible between infill and perimeter rasters, which may correspond to gaps present from fabrication.

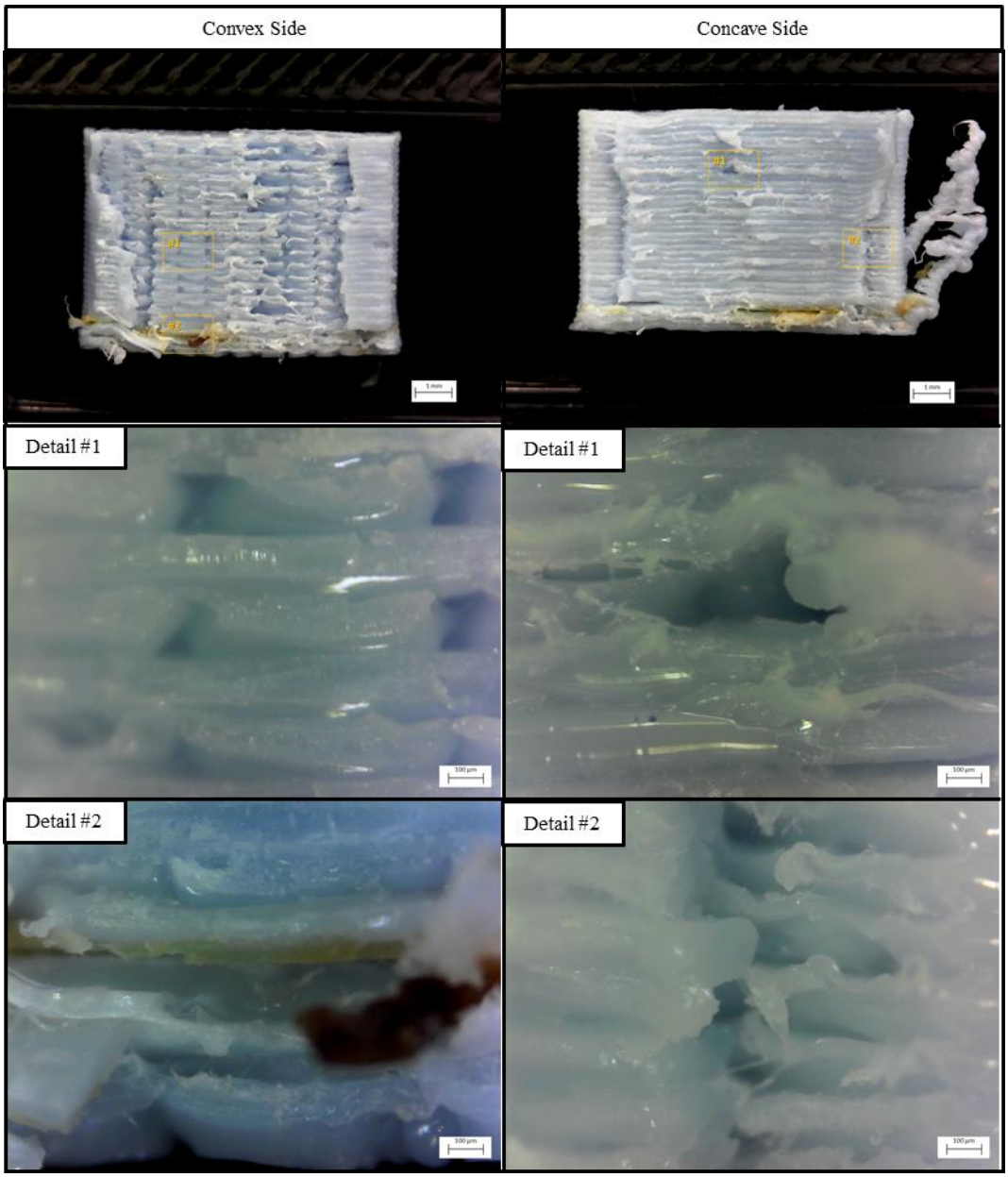

Figure 4.42: Fracture surfaces of IBS specimen 2 for interface between compositions 25% and 12%.

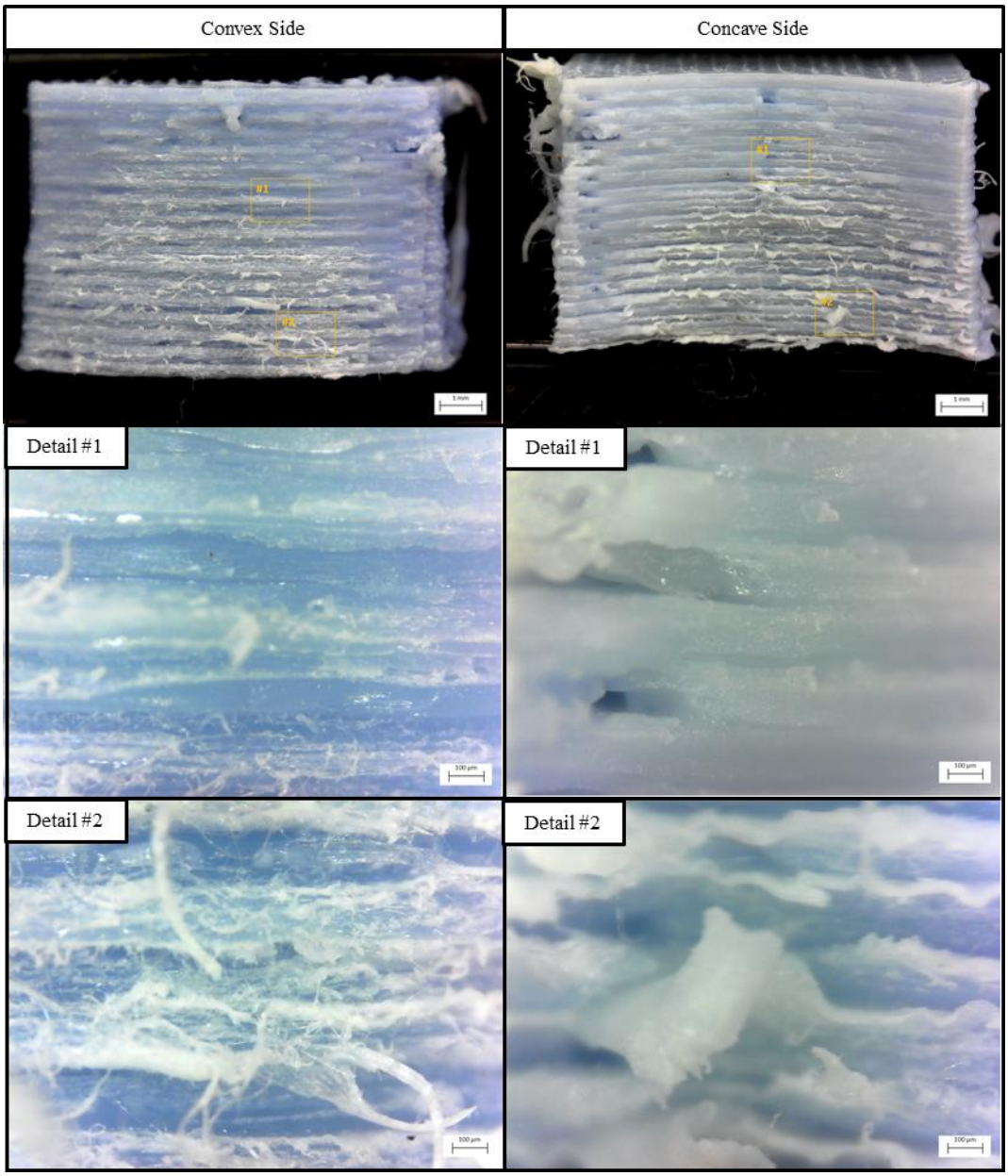

Figure 4.43: Fracture surfaces of IBS specimen 1 for interface between compositions 50% and 25%.

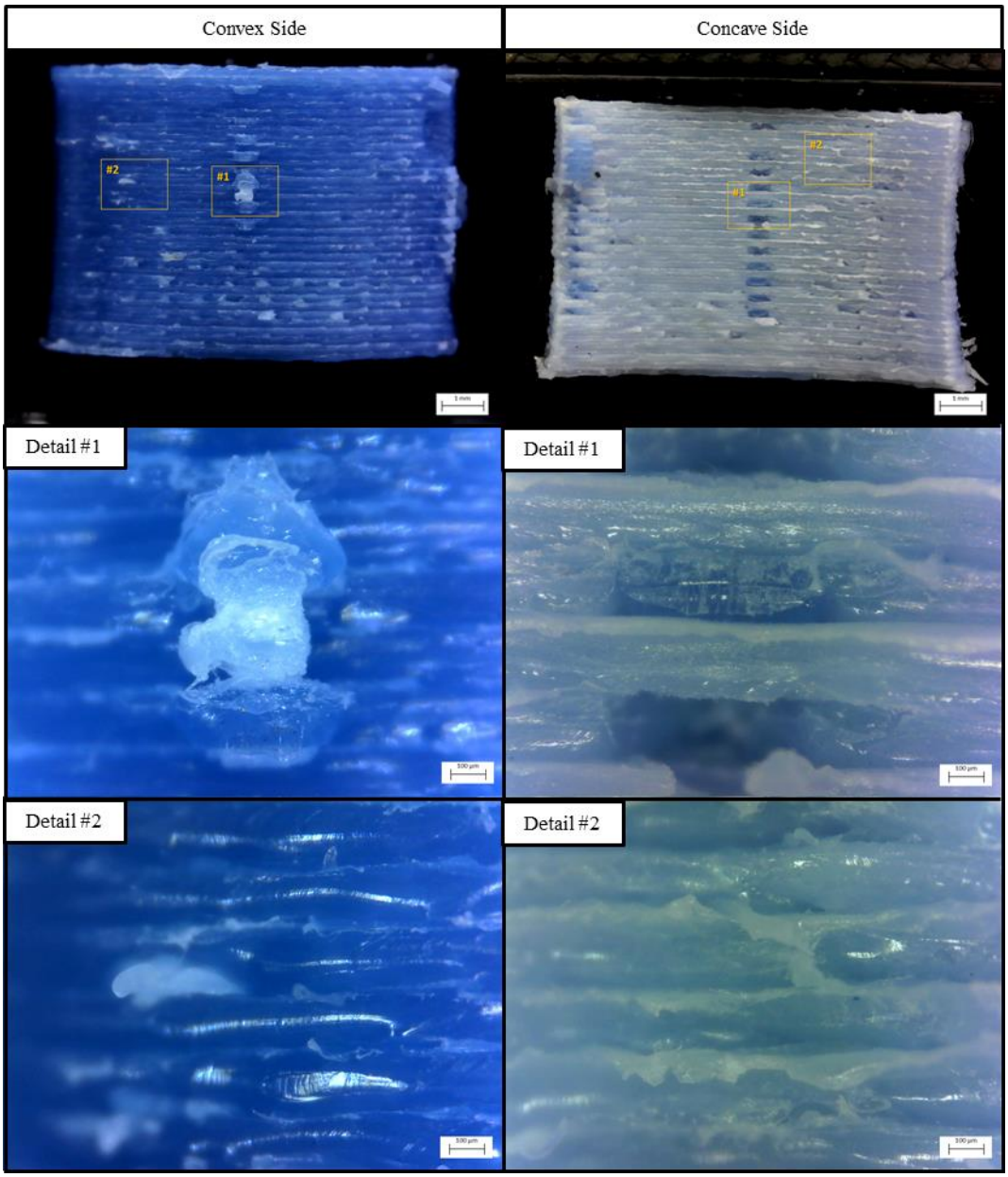

Figure 4.44: Fracture surfaces of IBS specimen 1 for interface between compositions 100% and 50%.

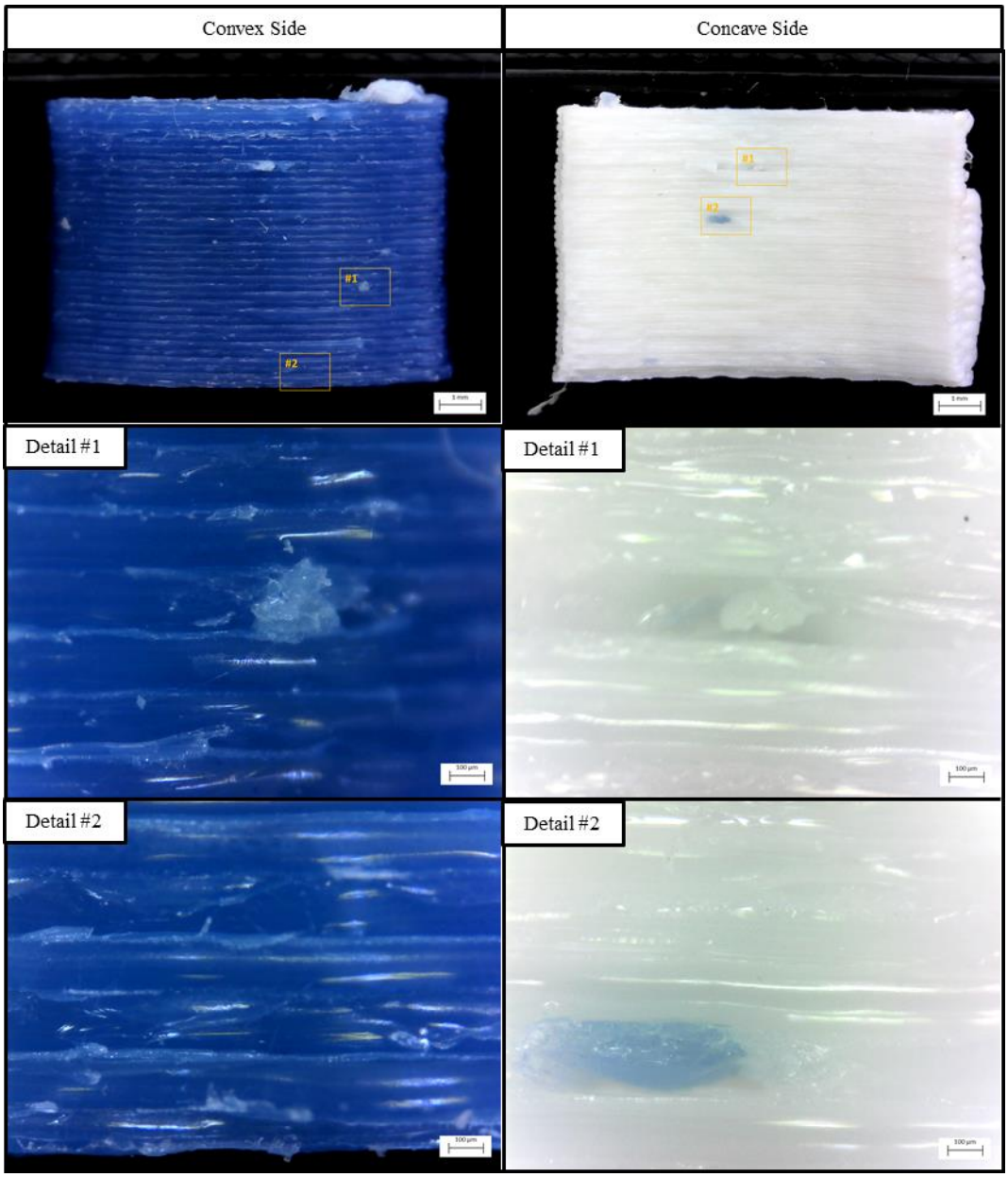

Figure 4.45: Fracture surfaces of IBS specimen 1 with compositions 100% and 0%.

4.4.4 2D FE Analysis

FE Model Verification

Results from FE model analysis to verify FE methods are provided in *Table 4.7* and graphed in *Figure 4.46*.

Table 4.7: Comparison to verify that methods of FE analysis match Lauke, Schüller, and Schneider 2012

Diameter divided by Width	Stress Concentration Factor at Center of Interface		Singularity at Edge
	Model Results	Lauke, Schüller, and Schneider 2012	
1.01	1.129	1.128	No
1.10	1.111	1.109	No
1.50	1.059	1.058	No
2.00	1.027	1.026	Yes

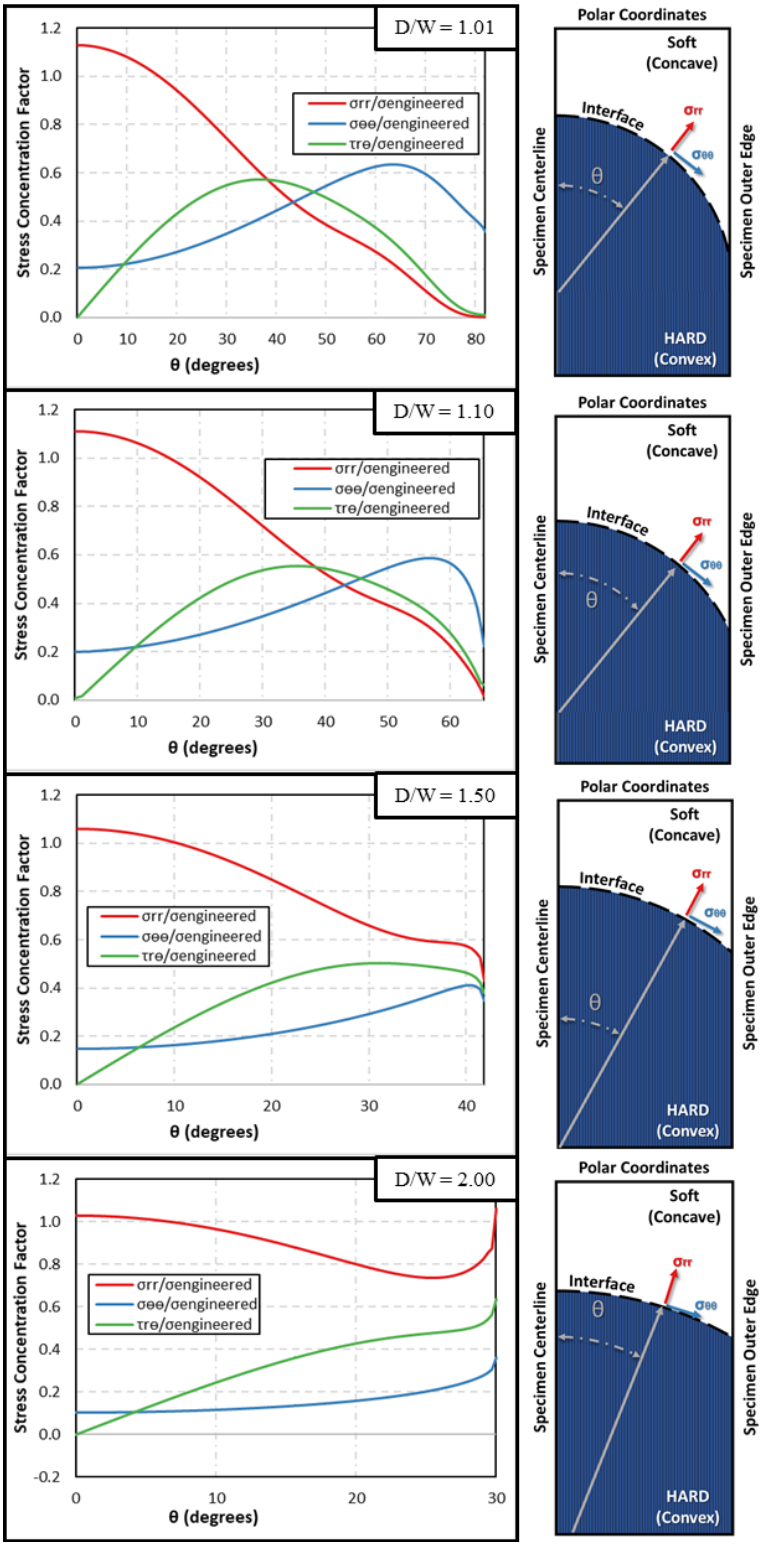

Figure 4.46: Stress concentration factors in polar coordinates across interfaces of varying geometries. D/W is the ratio of the interface curvature and the width of the specimen.

FE Analysis of IBS tensile tests

Results from FE analysis of experimental results gathered from IBS tensile tests are provided in *Figure 4.47* and graphed in polar coordinates in *Figure 4.48* and in cartesian coordinates in *Figure 4.49.*

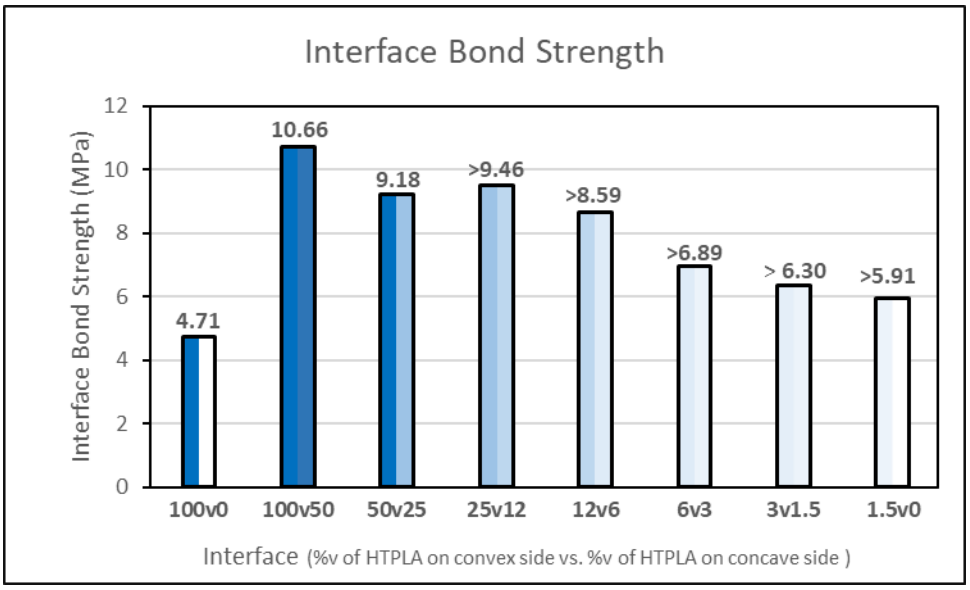

Figure 4.47: Peak radial stress as determined through FE analysis of IBS tensile test results for each interface composition.

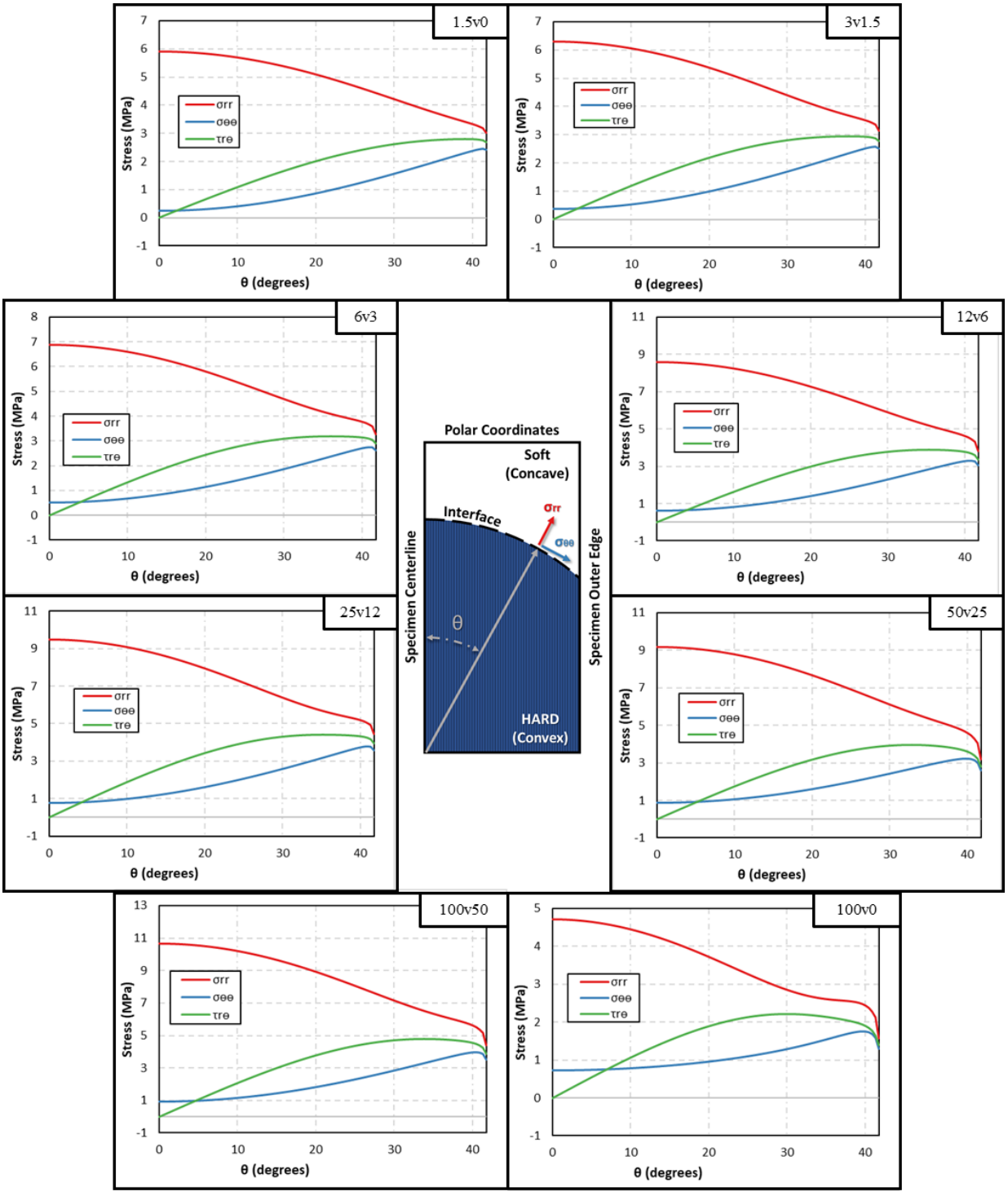

Figure 4.48: Normal and shear stress vs. interface path graphed in polar coordinates. Each graph provides results for each interface composition of IBS tensile test results.

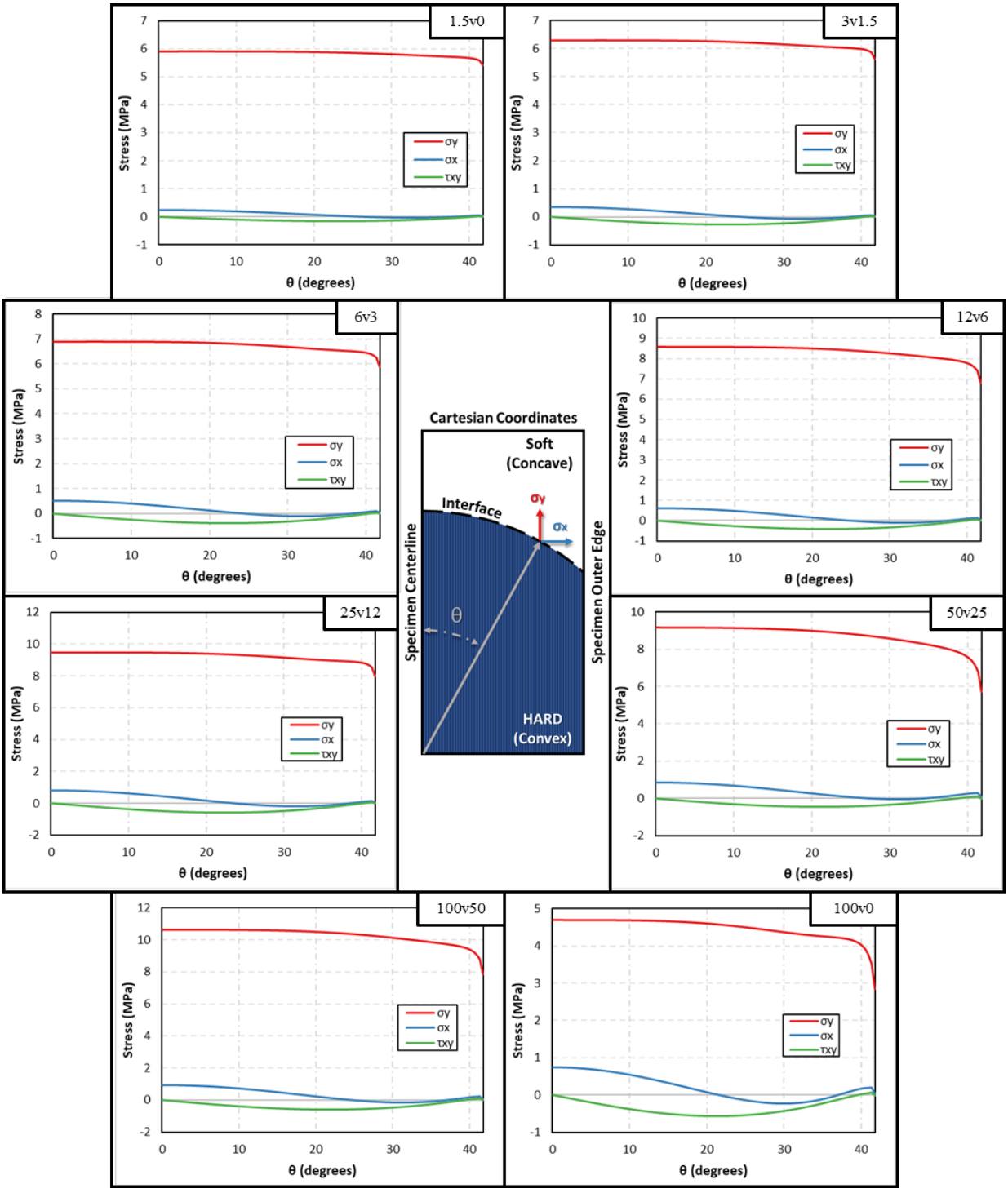

Figure 4.49: Normal and shear stress vs. interface path graphed in cartesian coordinates. Each graph provides results for each interface composition of IBS tensile test results.

4.5 Discussion

Aim 2 achieved many of the functions and capabilities desired for fabrication of synthetic tissue. Material composition can be varied throughout a continuous range of filament blends to achieve local variation in mechanical properties including incremental changes in composition to form functional gradients. Future use of these methods and materials can reference the mechanical properties presented in this study to inform design decisions.

Many of the compositions tested in this study have a minimal elastic region which in some applications may be desired but may be undesirable in others. Relative to modulus of elasticity, musculoskeletal tissues have a larger elastic region than these materials. As printed, these materials may not maintain their printed geometry after loading. A further limiting factor in applying this technology may be the relatively low UTS and σ_{IBS} as compared to musculoskeletal tissues.

This study did not determine the ultimate load of four interface compositions and was unable to consistently break four of the compositions tested. These results were further limited as they only characterized materials printed along the printer's X-axis.

4.5.1 Tensile Characteristics of HTPLA and NF Blends as Fabricated in an Active-mixing FFF Printer

Technology, methods, and materials utilized in this study demonstrated effective local composition control during FFF. Substantial changes in material properties was possible through variation of material composition. With the only exception being 1.5%, increased %v HTPLA corresponded with increased E and σ_Y.

Specimens with 50% composition have the lowest UTS and are the only specimens that prematurely necked during tensile testing. Necking was observed in fracture specimen, DIC results, and in the stress-strain diagram where the slope sharply transitioned to a negative slope from the elastic region.

4.5.2 Tensile Characteristics of HTPLA and NF Blends as Compared to a Human ACL

The filaments in this study were selected to enable simulation of human knee tissue. To better understand the potential application of these materials and methods for knee tissue simulation, it is appropriate to compare these tensile results to human ACL's tensile properties.

ACL Properties

The ACL exhibits four sequential phases of tensile load response including toe, linear, prefailure, and rupture. As load increases within the toe region, collagen molecules uncrimp, and the ACL's stiffness increases. Within the linear region, the ACL's collagenous tissues elongate, during which the ligaments stiffness reaches its maximum. The ACL's stiffness is defined as the peak stiffness observed in the linear region. The average moduli across the ACL's various bundles range from 284-155 MPa with a wide standard deviation ranging from 141-114 MPa (D. L. Butler et al. 1992; Peters et al. 2018). Rather than occur suddenly, failure of the ACL can progress gradually due to collagen rupture or slipping, which is described as prefailure and can be observed in load response as decreasing stiffness until rupture occurs. Average maximum stress and strain varied by bundle and range from 15-38 MPa and 15-19%, respectively (Takeda et al. 1994; Ochi et al. 2016; D. L. Butler et al. 1992).

ACL strain as determined in various studies may differ greatly due to subtle differences in measurement techniques. Factors contributing to these variations include techniques for measurement, methods for determining initial length, population diversity, and the ACL's non-uniform behavior. Despite measurement variability, it is worth noting reported ACL strains of common knee loading conditions.

ACL strain during passive knee flexion has been measured to be less than 2% between 10° and 110° but exceeding 8% strain in passive hyperextension and deep knee flexion (Dienst, Burks, and Greis 2002). During gait mid-stance and end-of-swing phase, ACL strain was estimated to be 10% or greater (Ochi et al. 2016; K. A. Taylor et al. 2013). ACL strain during squatting is estimated

to be 4.5% (Beynnon et al. 1997). Cycling is reported to have only 1.7% ACL strain (Dienst, Burks, and Greis 2002).

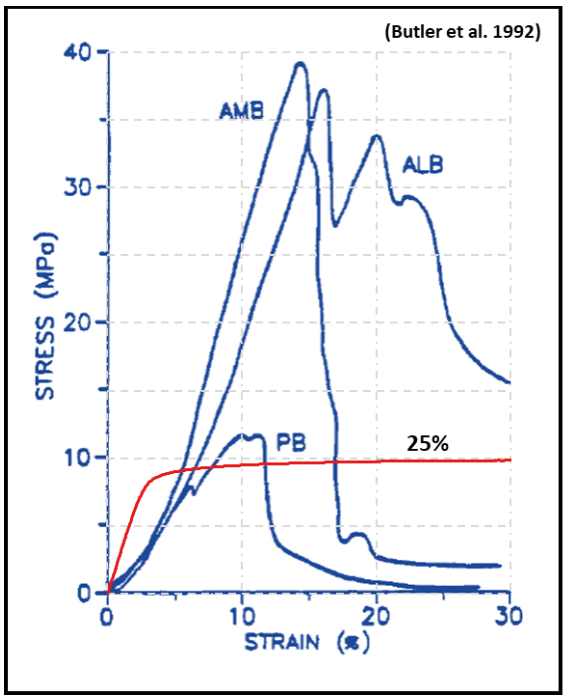

Figure 4.50: Typical ACL bundle stress-strain diagram extracted from Butler et al. 1992 (blue) with typical stress-strain curve of composition 25% cropped and overlaid to match axes (red). The three separate sections of the ACL tested by Butler et al. are the anteromedial band (AMB), posterior bundles (PB), and anterolateral band (ALB). Composition 25% reaches its maximum stiffness of 332 MPa at the start of loading and does not have a toe region as observed in the ACL stress-strain curves which average a maximum stiffness of 284 MPa. This difference in early strain behavior results in abrupt deviations in load response. Composition 25% loses its ability to simulate an ACL's stiffness near its yield point of 2.21% strain and 6.61 MPa of stress, which can be contrasted against the average ACL rupture that occurs at 38 MPa of stress and 15% strain. The 25% composition elongates beyond 30% strain and fails at 32.8 MPa indicating that improved simulation of the ACL may be possible through processing techniques like strain-hardening.

Comparison of ACL Properties to Composition Blends of 25%v HTPLA and 75%v NF

This study's methods provide a wide range of materials with stiffness above and below the stiffness of a human ACL. With its E equal to 332 MPa, composition 25% is closest to the ACL's stiffness of approximately 284 MPa. Its UTS of 32.8 MPa is also reasonably close to the ACL's maximum stress of 38 MPa; however, its $EL\%_F$ of greater than 165% exceeds the ACL's maximum

strain of 15% (S. L. Woo et al. 1991; Ochi et al. 2016; Peters et al. 2018). While the ACL includes a toe region with a low initial stiffness, the stiffness of the 25% composition is at its maximum at the start of tensile loading and begins to yield at only 2.21% strain (*Figure 4.50*). Most reported strains for physiological knee loading conditions far exceed the yield strength of composition 25%, but such comparisons are limited by the variation in strain measurements as described previously. A more comprehensive discussion on ACL simulation is provided in section 5.5.1.

4.5.3 Interface Bond Strength between Blends of HTPLA and NF as Fabricated in an Active-mixing FFF Printer

Fractography

Through fractography, three IBS compositions were determined to have failed at the interface as is desired for determination of bond strength, and one IBS composition that failed within the convex material at the interface between the infill and perimeter rasters. Because the print configuration extruded the convex materials of each layer before printing the concave materials, the convex materials solidified and formed a surface profile for which the concave materials were forced to conform. The resulting surface profile resembles a rectified sine wave as described in *Figure 4.51*. These features are known to increase the surface area of the interface, develop stress concentrators and were not included in the FE model. Although these features are common in FFF, the specific form of the feature will vary with certain changes made to slicer settings. Had these specimens not been processed through the custom "Sort by Tools" program, this profile would have alternated inflexion with each layer rather than maintain inflexion across layers.

Some fracture surfaces have rasters of convex material extending into the concave side of the interface (*Figure 4.52*). These rasters are not a result of extrusion commands but are the result of oozing during travel moves that cross the centerline of the specimen. The two specimens where these features are most prominent are specimen 2 of the 100v0 tests and specimen 1 of the 100v50

tests. Such features were not included in the FE model and are known to increase the surface area of the interface and act as stress concentrators.

Another defect observed in various fracture surfaces were deposits of thermally degraded thermoplastic (*Figure 4.42*). These deposits were developed when oozed material got caught on the nozzle and later wiped into the specimen.

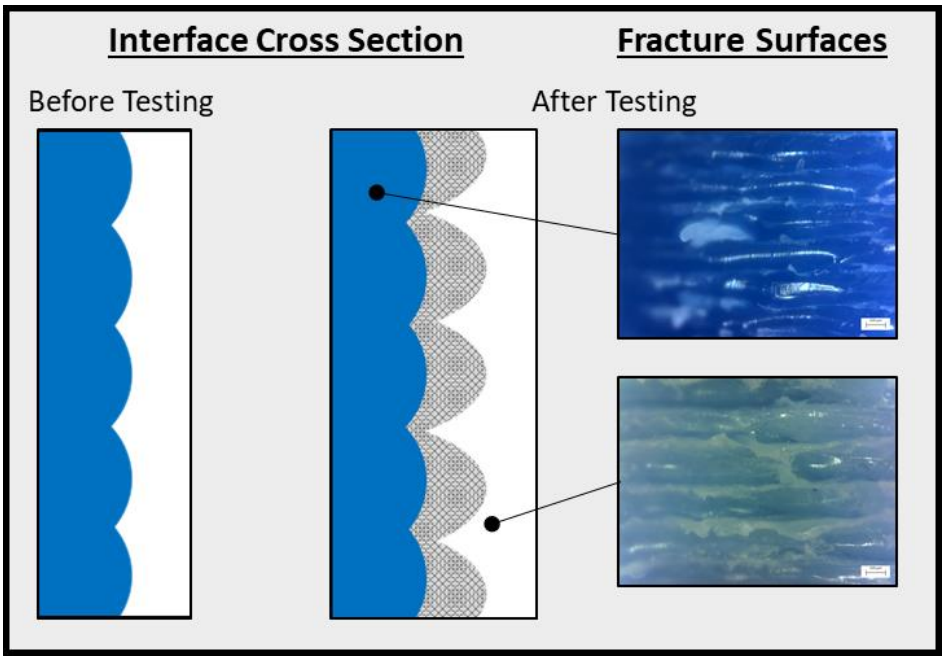

Figure 4.51: Diagram of interface cross section before and after tensile testing. Blue color at interface represents material printed on the convex side of interface, and white color indicates material printed on the concave side of the interface. Example fracture surfaces are from IBS specimen 1 with composition 100v50.

Each of the three IBS compositions that failed at the interface have fibrils extending from the bottom and top of each layer as are diagramed in *Figure 4.50* and are visible in *Figures 4.43-45*. Compositions 100v0, 100v50, and 50v25 have respectively increased fibril length and density.

Gaps formed between infill and perimeters in specimens with compositions 12v6, 6v3, 3v1.5, and 1.5v0 but did not break. Similar gaps were formed in 25v12 specimens which propagated into a fracture surface separating the infill from the perimeter of the concave side of

the specimen. Individual rasters that are oriented parallel to the specimen's tensile axis separated from each other and necked prior to failure.

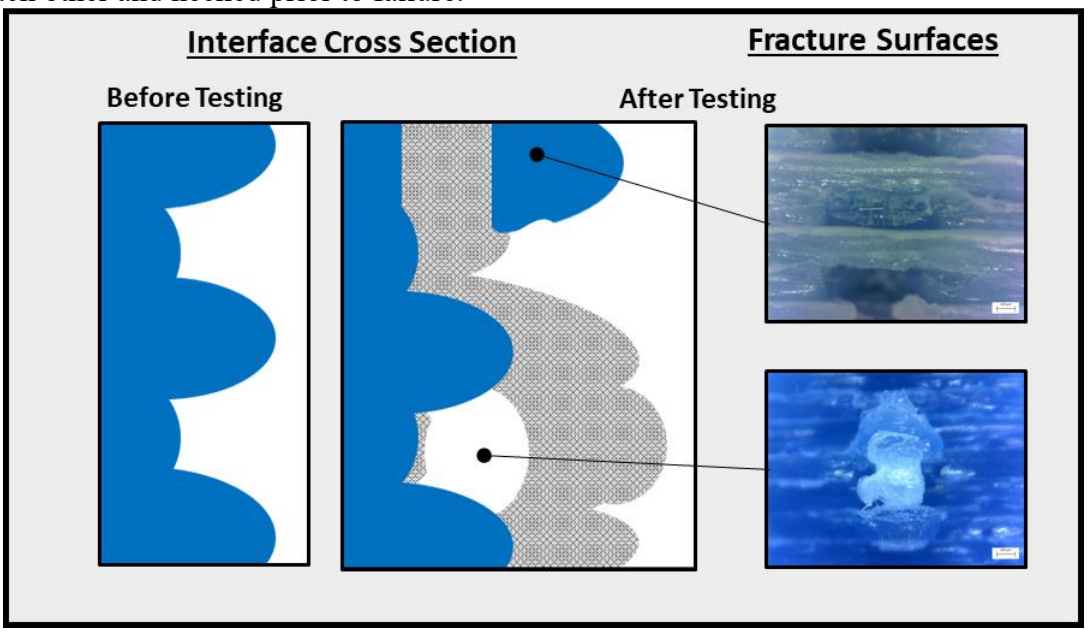

Figure 4.52: Diagram of interface cross section at the specimen's centerline before and after tensile testing. Blue color at interface represents material printed on the convex side of interface, and white color indicates material printed on the concave side of the interface. Example fracture surfaces are from IBS specimen 1 with composition 100v50.

Implications of Fractographic Observations on Printer Performance

The observations made during fractographic analysis were able to identify printer functions that notably influenced the characteristics of the IBS interfaces tested in this study. Tuning and techniques integrated into slicer software and printer firmware greatly decreased oozing observed during printing, but the remaining oozed material still resulted in defects due to unintended extrusion of one material into another and formation of thermally degraded materials that were deposited into the printed part. Although further development in hardware may provide potential solutions to oozing, improvements may be possible through integration of software features like pressure advance and further optimization of travel moves to decrease time spent traveling and minimize travel moves across the perimeters of other components. Another flaw identified through

fractography was the presence of gaps between infill and perimeters. A solution may be possible by increasing the infill/perimeter overlap setting in slicer software.

Tool order was selected in this study to benefit the procedure for priming the hotend, but the surface shape observed on IBS interfaces indicates that the tool order per layer should proceed from the hardest to softest materials that form interfaces requiring the greatest effective bond strength possible.

Bond Strength Compared to UTS

Results from this study identify the weakness of interfaces produced in FFF when compared to the mechanical properties of the printed materials. The measured bond strengths ranged from 4.71 MPa to 10.7 MPa and the UTS of the materials tested ranged from 23.7 MPa to 66.8 MPa. Comparing these results, it is evident that binary interfaces impose a substantial limitation to the mechanical performance of FFF printed parts, but it also identifies an opportunity to minimize this limitation through implementation of functional gradients.

Potential Benefits through Implementation of Functional Gradients

Blends of HTPLA and NF demonstrated a composition-dependent correlation with stiffness as is desired for relieving stress concentrators in a functional gradient. Other studies have highlighted the benefit of these structures due to stress relief resulting from gradual changes in material stiffness. If these functional gradients result in greatly decreased bond strengths, the implementation of a functional gradient may be ineffective in increasing mechanical properties despite reduced stress concentrations; however, bond strength as a material-specific property is rarely determined by current practices due to limitations in measuring these bonds without the influence of stress singularities (Chowdhuri and Xia 2013).

This study's analysis of bond strength was configured to reduce the influence of stress singularities at the interface edges by using a curved interface but may have not eliminated them. A 2D FE model was used to account for the stress concentrations resulting from the curved

interface but the model was unable to identify if stress singularities were present at the interface edges intersecting the bottom and top layer of the IBS specimens.

Results indicate that replacing binary interfaces with functional gradients in FFF printed parts can potentially produce a net increase in bond strength. Consider substitution of a binary interface between pure HTPLA and pure NF with a series of the seven other binary interface compositions tested in this study. The peak stresses achieved in these compositions indicate that net bond strength will increase by a minimum of 25%, based on the peak stress of 1.5v0, with a maximum increase in strength of 95%, based on IBS of 50v25. Additional benefits to the interface may exist due to stress relief from gradient stiffness across the interface, which in a similar configuration calculated a stress reduction of 30% (Bartlett et al. 2015).

FE Model Verification

Our FE models for determination of stress distribution along interfaces from four different geometries agreed with the results from Lauke et al. (Lauke, Schüller, and Schneider 2012). The largest deviation in results was an increase in stress concentration factor by 0.002. This minor difference in results can be attributed to the finer mesh density at our model's interface.

Limitations in Determining Bond Strength

This study does not account for anisotropy and only determined the mechanical properties of parts printed along the printer's X-axis with 100% rectilinear infill. Because four of the IBS compositions did not break during testing and one composition did not fail at the interface, this study's ability to determine IBS of five interfaces was limited. The curved interface of the IBS specimen was selected to provide the smoothest interface possible while minimize surface stress singularities, but it only eliminated stress singularities as determined by 2D analysis of the interface. The FE model was limited to calculating stress in 2-dimensions assuming a smooth interface, which did not include the interface features identified through fractography or account for stress singularities that were likely present at the top and bottom edges of the interface. The FE model is further limited by its assumption that the materials behave elastically. All interface

compositions tested in this study except for 100v50 exceeded the yield stress of at least one of its materials.

4.6 Conclusion

The technology and methods described in this study have advanced FFF by providing a continuous range of material compositions that can be printed within a single layer without user intervention during the printing process. These methods enable fabrication of printed components that were not previously possible. Results from this study indicate that increased strength of FFF printed parts with binary interfaces may be strengthened by integrating functional gradients into the designs and fabricated using these methods. In addition to characterization of specific materials, the technology of this study can be applied to other materials and has potential applications with variation of other material properties and other materials including those containing fiber and particle reinforcement.

Chapter 5: Aim 3 - Synthetic Knee Design and ACL Printed using Local Composition Control and Characterized during Tensile Testing

5.1 Introduction

Advancements in musculoskeletal biomechanics are constrained by a lack of a physical alternative to cadaver specimen and a lack of experimental measurement during physiological loading. Medical applications for synthetic, human tissue have been constrained by the ability to fabricate complex structures with local variations in mechanical properties.

With the ultimate goal of developing a synthetic knee offering a repeatable kinematic response to physiological loads, this study advanced the technology for fabrication of synthetic tissue through use of the advances in additive manufacturing from aim 2 to produce a synthetic FATC. This aim advances biomechanics through development of techniques to fabricate synthetic tissue and characterizes the result during tensile testing. Included in this effort is knee model development from MRI's, structural modification of the knee model, isolation of the FATC, grip section design, insoluble support model design, soluble support model design, slicer configuration, FATC fabrication, specimen post processing, and tensile testing. Tensile response of the specimen was compared to physiological response demonstrated by Woo et al. 1991. Tensile tests were performed at 30° knee flexion with load applied in parallel to the ACL anatomical axis and parallel to the tibia's mechanical axis.

To preserve an accurate anatomical appearance, geometry was not modified; however, the internal structure and local composition of the synthetic ACL composition was selected to be 300 MPa in order to match the reported modulus of elasticity of biological materials. With the goal of simulating knee kinetics and kinematics, the most important features of ligaments within the synthetic knee will be tensile stiffness, bending stiffness, and ultimate load.

The properties of thermoplastic polymers selected for this project do not themselves simulate the hierarchal structure of ligaments. Synthetic ligaments with uniform composition resisted bending and, in turn, joint rotation. Preliminary tests of synthetic ligaments printed with traditional FFF desktop printers failed prematurely at the insertion interface between bone and

ligament, but functionally graded interfaces were integrated into the design and failure occurred in the mid length of the synthetic ACL.

5.2 Background

5.2.1 Clinical Relevance

As the life expectancy of the human population continues to expand, prevalence of musculoskeletal injury and disease also increases. The technology investigated in this study is intended to contribute to development of synthetic analogs of human joints that can deliver an entirely new opportunities for investigation of fundamental biomechanics and improved methods for training orthopedic surgeons. The FATC was selected for this study because of this systems role in human knee biomechanics and for its clinical relevance. An estimated 80,000 to 250,000 ACL injuries occur annually in North America (Griffin 2006), which results in the ACL being the most commonly reconstructed ligament in the human body.

5.2.2 Synthetic Tissues and Knees

Existing synthetic knees fail to mechanically respond as cadaveric knee specimens, and as such, they are not effective for investigation of musculoskeletal biomechanics, quantification of orthopedic surgical methods, or controller optimization for joint load simulators.

5.2.3 Additive Manufacturing for Biological Applications

The general use of AM for biological applications should not be confused with bioprinting, which is 3D printing of materials containing viable living cells. Biological applications for AM include but are not limited to tissue engineering, tissue scaffolding, surgical preparation, pharmaceuticals, forensic science, and education. Nearly any 3D printing method can fabricate synthetic anatomy, but each has benefits and limitations (Fredieu et al. 2015). For fabricating synthetic musculoskeletal systems to simulate accurate joint kinetics and kinematics during physiological loads, three AM methods stand out. Polyjet printing is a commercially available method with a wide range of available material stiffness (hardness: shore 27A – 84 D), high

resolution, local color control, and local composition control. Extrusion based 3D printing can produce hydrogels with extremely low modulus for bioprinting and scaffolds due to its ability to extruder through a plunger (Hockaday et al. 2012)

5.2.4 Human Tissue Properties

General Attributes of Human Tissue

Mechanical characteristics of human tissues are highly variable and are dependent upon numerous factors including but not limited to microstructure, composition, conditioning, orientation, moisture, temperature, density, load rate, geometry, age, and sex. This variability among tissue properties and variability among measurement techniques can complicate attempts to predict the mechanical response of human tissue, much less the cumulative response of a musculoskeletal system like the human knee. For this study, it is necessary to estimate the stiffness of relevant biological tissues to assist with selecting local compositions of the synthetic knee.

Bone Properties

Cortical, trabecular, and subchondral bone are all present in the human knee (Reszka 2010). Each of these types of bone has unique properties and densities having elastic modulus ranging from 1,100 MPa up to 6,000 MPa (Choi et al. 1990).

Ligament Properties

Ligaments have three regions of stress-strain response. The toe region is at the beginning of the stress-strain curve and accounts for engagement of fibers as they unwind with increasing stiffness as the ligament elongates. The second region is the linear region where most fibers are engaged and elongate in response to ligament stress. The final region is the failure region where fibers progressively break as load increases. The elastic modulus of knee ligaments vary widely from 25 MPa to 447 MPa (Bonner et al. 2015; Peters et al. 2018). These material properties vary within the structure of each ligament. An example of this is the variation of ACL and PCL stiffness by bundles. Respectively, the anterior and posterior bundles of the ACL ligament have tangent

moduli of approximately 286 MPa and 150 MPa (S. L. Y. Woo et al. 2006; D. L. Butler et al. 1992; Peters et al. 2018).

Meniscus Properties

The meniscus, more than any other component of the knee, may require specific control over anisotropic properties to provide the desired physiological response. Unlike cartilage, which is constrained from movement, the meniscus may travel and expand within the joint. This movement is dependent upon loading conditions, radial and circumferential stiffness of the meniscus, and the stiffness of the meniscal horns connecting the meniscus to the tibial plateau (Vedi et al. 1999).

Meniscus is heavily influenced by its anisotropic properties. Axially, the meniscus is extremely compressible achieving a modulus less than 150kPa (Chia and Hull 2008), but the meniscus demonstrates a much stiffer response in radial (E = 48 MPa) and tangential (E = 198 MPa) directions (McDermott, Masouros, and Amis 2008; Makris, Hadidi, and Athanasiou 2011). The stiffness for the meniscal roots have been reported as 124 N/mm for the Anteromedial root, 123 N/mm for the Posteromedial root, 151 N/mm for the Anterolateral root, and 128 N/mm for the Posterolateral root (Ellman et al. 2014).

Articular Cartilage

Articular cartilage is composed of water, collagen, chondrocytes, proteoglycans, glycoproteins, calcium and other miscellaneous proteins. Articular cartilage contains zones organized in layers from the articular surface to the cancellous bone substrate. Each zone has distinct microstructural features. The superficial tangential zone is nearest to the articular surface, has dense collagen fibers parallel to the articulating surface, and provides much of the tensile properties necessary for physiological loads. Below this zone is the middle zone which contains randomly oriented collagen fibrils and bridges the gap between the superficial zone and the deep zone. The deep zone has the largest fibrils which are oriented as columns directed toward the

articulating surface. At the base of the deep zone is a calcified zone bonding the cartilage to the subchondral bone (Sophia Fox, Bedi, and Rodeo 2009).

5.2.5 Methods for Manipulating Mechanical Properties through Structural Design

Open Cell Foam

AM methods are ideal for geometric control of open-cell foam materials and are often implemented in printer settings to modify print times, material consumption, warping, density, mechanical properties, and more (Tsouknidas et al. 2016; Baich and Manogharan 2015). Generally, the young's modulus of an open-cell foam (E*) can be calculated using the equation:

$$E^* = C_1 * \left(\frac{\rho^*}{\rho_s}\right)^2 * E_s \quad (4)$$

$C_1$is a constant that is specific to cell geometry, ρ^*/ρ_s is the relative density of the cell structure, and E_s is the young's modulus of the material in bulk form (Harley et al. 2007). FFF printers can consistently print with 10% infill (Lužanin et al. 2014), which may be augmented with support material to form open-cell structures. Since C_1 is often equal to 1 (Harley et al. 2007; Murr et al. 2012), relative density and cell geometry can be tuned to theoretically reduce the effective modulus of elasticity by 99% or more; however, consideration must be made for buckling and densification when dealing with loading conditions that include compression (Harley et al. 2007).

The relative modulus of elasticity can also be controlled anisotropically. This can be accomplished by adjusting the relative length of longitudinal and transverse struts in an open-cell structure (Mathieu et al. 2006).

Co-continuous Multimaterial D-structure

Co-continuous composites structures have been recently developed to resemble an open cell foam embedded inside of another material to form a large composite structure. These have particular value in simulating synthetic tissue as they can be combined with hard and soft materials to develop super elasticity (Mansouri et al. 2018).

5.3 Methods

5.3.1 Preliminary Tests

Bi-material Print of Patella with Cartilage

This study was previously described in section 4.3.1 and 4.4.1.

Bi-material Print of Bony Islands with ACL and PCL ligaments using ABS and NF

This study was previously described in section 4.3.1 and 4.4.1. Catastrophic failure of the specimen was observed at the interface between the tibia and ACL. This mode of failure emphasizes the possible limitations resulting from a weak interface strength and the stress concentrators developed between soft and rigid materials.

5.3.2 Initial Anatomical Knee Model Development

The synthetic knee model was developed from magnetic resonance images (MRI) previously used for computational modeling by Wilson (Wilson 2015). The source for the knee model is the left knee of a 43-year-old male designated as specimen W, which was developed in Slicer 3D (Fedorov et al. 2012). The output from this program included undesirable artifacts, which were eliminated by custom MATLAB® (The Mathworks, Inc., Natick, MA) and Meshmixer (Autodesk Inc., San Rafael, CA) to smooth the resulting geometry and eliminate gaps between interfaces. The computer knee model was modified to account for deviations from known anatomical features and smoothed to decrease surface roughness. Components of the knee that were modelled included bones, cartilage, meniscus, ligaments, and tendons. The bones include distal end of the femur, proximal end of the tibia, and proximal end of the fibula. The three segments of cartilage were modelled including patellar, femoral, lateral tibial-compartment, and medial tibial-compartment. The four ligaments included are the ACL, PCL, LCL, and MCL. Both the medial and lateral meniscus were modelled.

Further knee model development emphasized a balance between physiological accuracy, printability, and structural performance. Gaps were placed between articulating surfaces to prevent bonding during printing, and the model's mesh was simplified to maintain geometric accuracy

while reducing surface triangle count. A block was added to secure the fibula to the tibia. In this form, the model is designated Knee_W and provides anatomical accuracy with minimal alteration to promote success in additive manufacturing (*Figure 5.1*). Further modifications were made to Knee_W to provide advanced features that potentially improve the physiological accuracy of a printed synthetic knee.

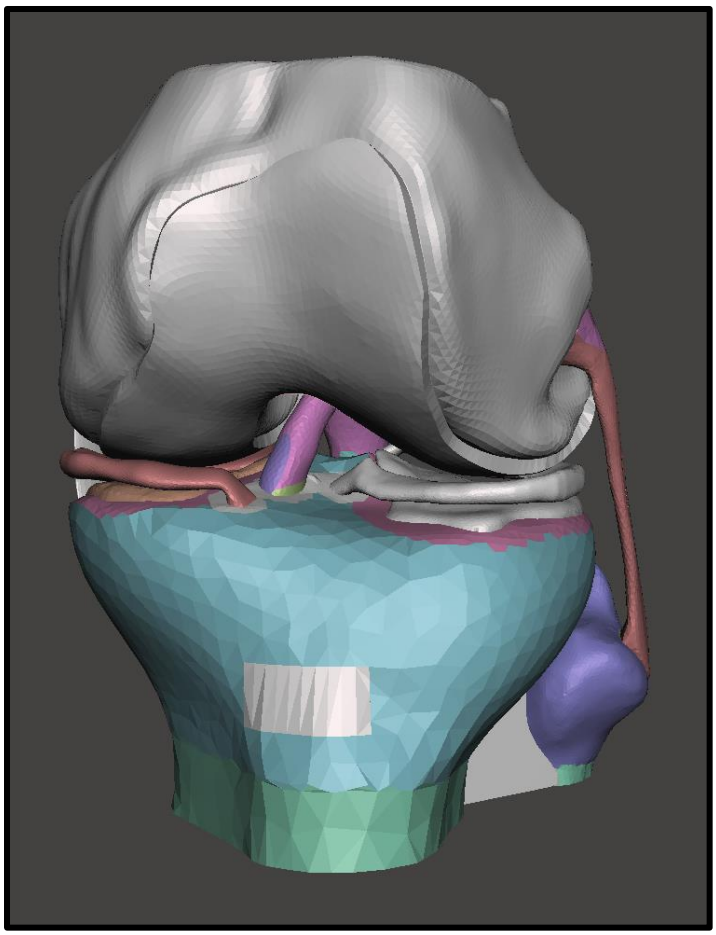

Figure 5.1: Computer model of Knee_W.

5.3.3 Knee Model Design Modification

Knee Model Development with Functional Gradients

Preliminary prints of the synthetic knee failed prematurely during manual articulation. These failures occurred at the interfaces between synthetic ligaments and synthetic bone. To overcome this limitation, functional gradients (FG), which generally increase the strength of an

interface when compared to a binary interface, were integrated within the bones at interfaces connecting to ligaments and meniscus. These modifications were applied to increase the strength of the printed interface and better simulate human tissue by avoiding premature failure due to interface debonding. This model is designated Knee_W_vG (*Figure 5.2*).

Knee Model Development with Ligament Cores

Another challenge for simulating human tissue is coordination of multiple mechanical properties for the same component. A specific challenge for this application is simultaneously matching tensile stiffness and bending stiffness. Material selection alone may not be capable of simultaneously matching these two properties. One approach to overcome this limitation is geometric modification of the design. To provide a potential solution to this challenge, the Knee_W_vG model was modified to combine the outer half of the FGs at each end of the ACL and PCL ligaments with a modified version of the ligament having a reduced cross-sectional area. Effectively, the ligaments were split into a core and shell. With this feature, the user is now capable of altering two compositions within the model to better match the tissue's properties. This model is designated Knee_W_vC (*Figure 5.3*).

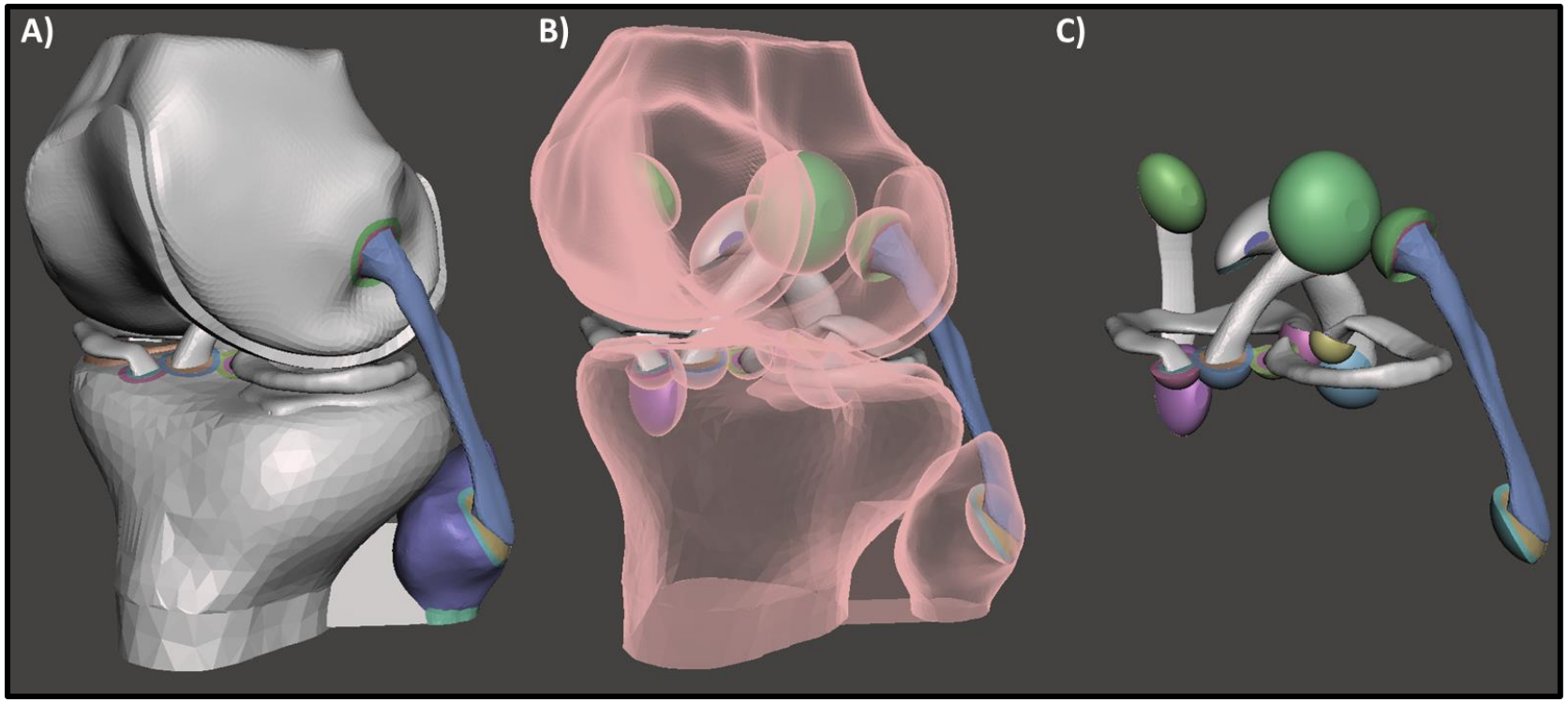

Figure 5.2: Computer model of Knee_W_vG. A) Model with all components intact. B) Model with partially highlighted bones and cartilage. C) Bone and cartilage models hidden to provide a view of functional gradients at the insertion sites of ligaments and meniscus.

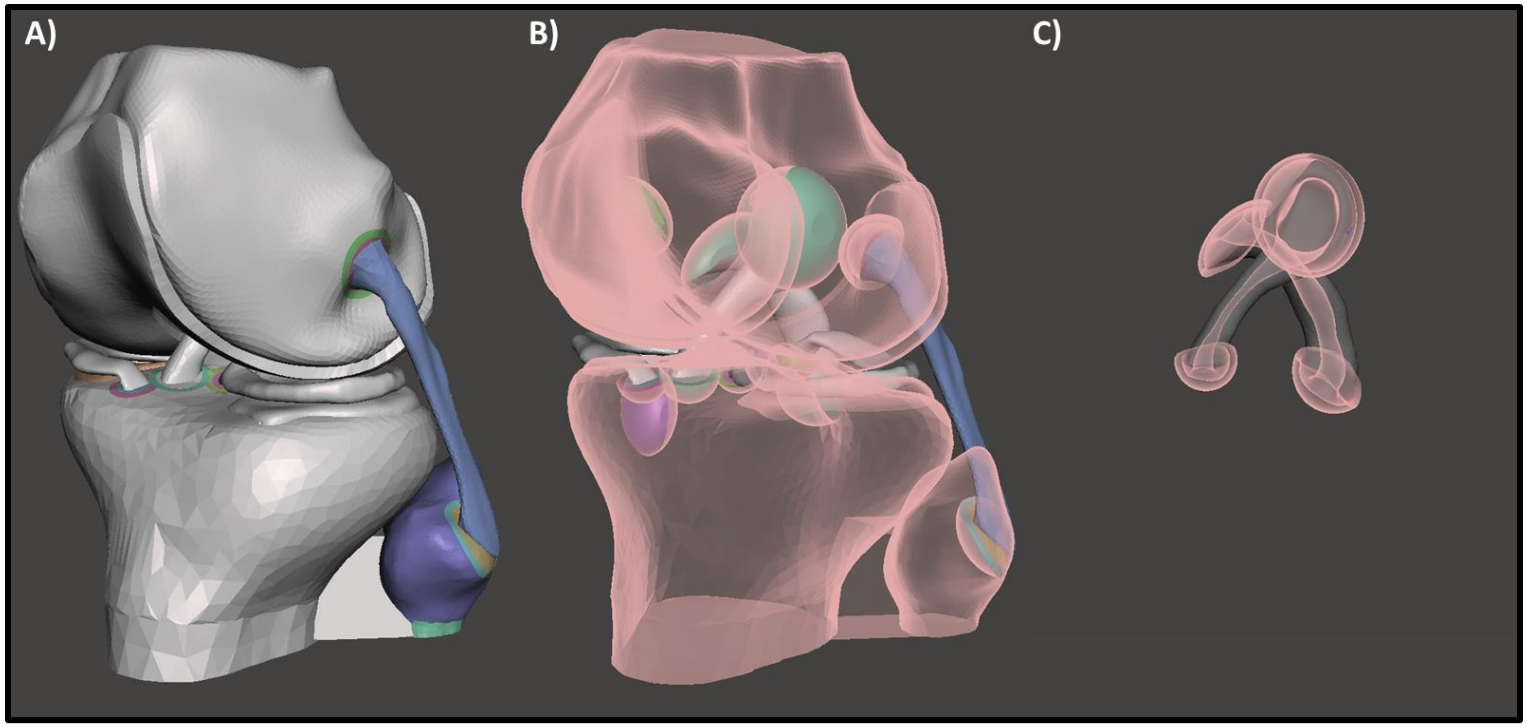

Figure 5.3: Computer model of Knee_W_vC. A) Model with all components intact. B) Model with partially transparent bones and cartilage. C) ACL and PCL isolated with core components of the ligaments highlighted.

5.3.4 FATC Model Development

The femur, ACL, and tibia along with relevant gradient geometries were extracted from Knee_W_vG to be used as the basis for the FATC models. Two versions of the FATC models were developed for tensile testing. The first FATC model supports loading the ACL along its own anatomical axis with the knee flexed at 30 degrees and is designated ACL_A. The second FATC model supports loading the ACL parallel to the Tibia's mechanical axis with the knee flexed at 30 degrees and is designated ACL_T. Both models are accompanied by manually developed soluble and insoluble support structures.

Grip Section Design

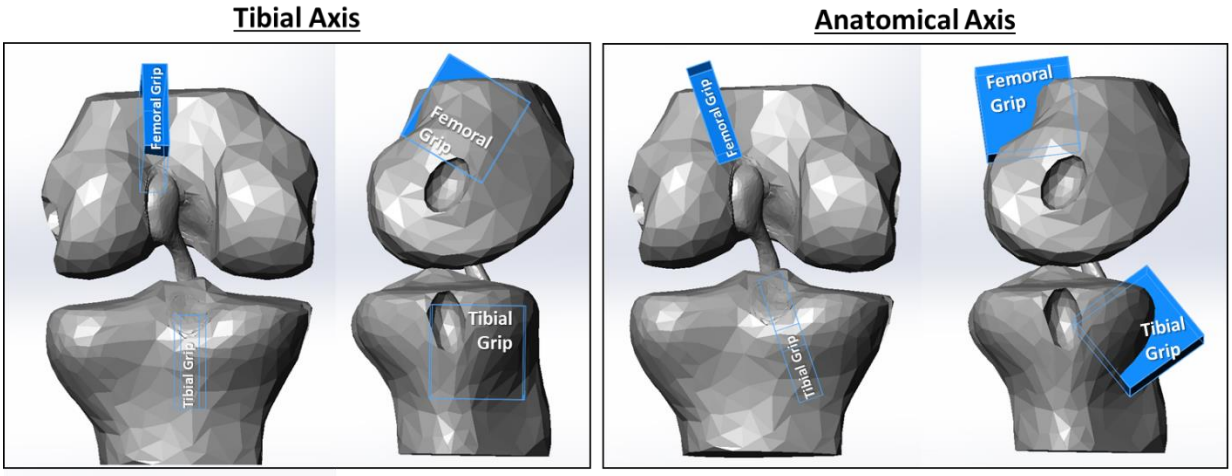

Figure 5.4: Grip section placement in SOLIDWORKS relative to femoral, tibial, and ACL models.

Anatomical components of the FATC were imported into SOLIDWORKS where grip section blocks (H: 30mm, W: 30mm, and D: 8mm) were extruded for mounting and alignment in the tensile test equipment. ACL_T grip sections were centered along the ACL's insertion site, rotated to facilitate 30 degrees of knee flexion, and extruded parallel to the respective bone's sagittal plane. ACL_A grip sections were centered along the ACL's insertion sites, rotated to facilitate 30 degrees of knee flexion, and extruded from a plane containing the ACL's anatomical line of action and the knee's anterior/posterior axis (*Figure 5.4*).

Component Isolation

STL models of the femur, tibia, ACL, respective gradients, and grip sections were imported into Meshmixer. Plane cuts were made to the femur and tibia models to isolate the FATC and avoid interference with the grip sections. The plane cuts were parallel to the grip section faces and positioned to avoid the gradient models (*Figure 5.5*).

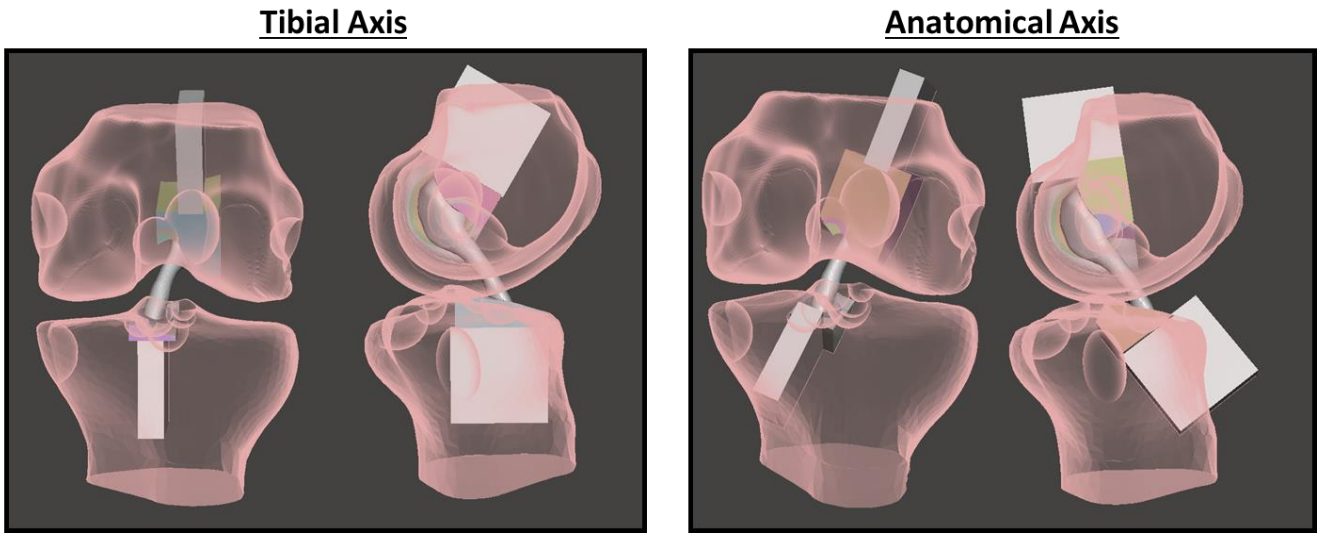

Figure 5.5: FATC models after plane cutting the femur and tibia. Transparent image of femur and tibia provided for reference.

Insoluble Support Structure Development

The combined FATC models were imported into SOLIDWORKS, where a raft and zigzag support structure were custom designed to intersect the combined model. The raft and support structure was exported as an STL file and imported into Meshmixer. A combined FATC model with surface normals flipped and offset by 0.4 mm was imported with the support structure. The models were combined and Meshmixer's "make solid" function was applied to create the desired intersection. Manual operations were performed to fine tune the insoluble support structure. Sections of the model that did not provide support to overhangs were removed and gaps were added in locations that are not easily accessibly or surround a component of the FATC (e.g. support structures that surround the ACL were cut into two pieces to allow them to be removed).

Soluble Support Structure Development

For each FATC design, isolated components of the knee and grip sections were imported into Meshmixer to form two separate surfaces. To form the first surface, all the models for the respective FATC design were combined and the surface normals were flipped. The second model was composed of all the FATC components with surfaces offset by 0.5 mm. Cumulatively, these two surfaces form a thin solid shell around the FATC model, which was then modified to only cover overhangs and locations where the insoluble support may otherwise contact the FATC model (*Figure 5.6*). These processes require extensive mesh modification to enable the necessary program operations.

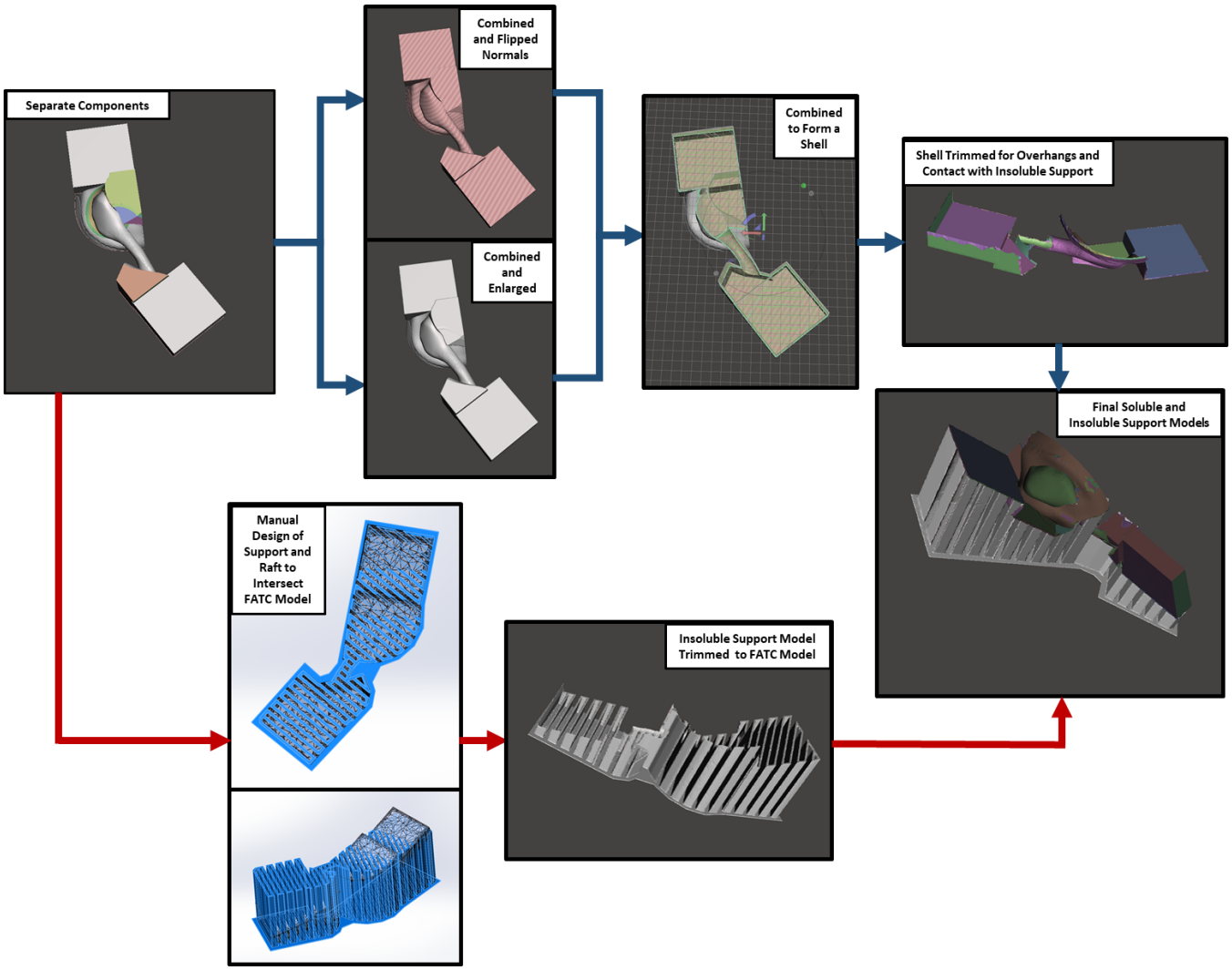

Figure 5.6: Block diagram describing process to create custom insoluble zigzag and soluble support models to assist with FATC printing. Red lines indicate process to make insoluble support, and blue lines indicate process to make soluble support. Blocks with a white background were operation performed in SOLIDWORKS, and blocks with dark backgrounds were performed in Meshmixer.

5.3.5 FATC Slicing and Fabrication

Six FATC specimens were prepared for tensile testing including one set of three ACL_A specimens and one set of three ACL_T specimens. Each set was sliced using the methods described in section 4.3.1, processed through the custom software described in section 4.3.3, printed on the MP2_R, and post-processed to remove the support structure.

Software Processing

Each set of FATC models was imported along with their respective support models into Repetier-Host. Models were arranged near one another to reduce length of travel moves. Nearly identical Repetier-Host settings (*Table 4.1-2*) were used for both sets but deviated in bone composition and soluble support composition. Each file was sliced into G-code commands and modified by the two custom programs described in section 4.3.3. The first custom program sorted the print commands by tool, which is synonymous with composition for this configuration, and the second program inserted priming towers into each layer. These files were loaded on an SD card for use in the printer.

Assignment of ACL Composition

By linearly interpolating the E of the 12% and 25% compositions, the synthetic ACL's composition was selected to be 22% in order to best match the biological ACL's average elastic modulus of 278-310 MPa (D. Butler 1986; Peters et al. 2018; D. L. Butler et al. 1992). The 22% composition is estimated to have an E of 290 MPa. Additional discussion on the material properties of the ACL is provided in section 4.5.2.

Differing Assignment of Composition

During printing, a series of filament jams were noted due to the addition of SC to the hotend. SC filament jammed during printing of the ACL_T specimen due to water absorption from the air. After dehydrating the SC filament, the printer then experienced NF filament jams due to thermally degraded SC filament working its way into the NF filament's heat break. To prevent

material from backflowing into the NF heat break, bone and support compositions were modified to maintain 5%v flow of NF into the hotend (*Figure 5.7*).

Fabrication

Both sets of specimens were printed on the MP2_R printer with HTPLA, NF, and SC filament in their respective extruders. The ACLs and the first half of the associated FGs, the ACL side of the gradient, were composed of 22% HTPLA blended with 78% NF. The second half of these FG's, the bone side of the gradient, were composed of 44% HTPLA blended with 56% NF. Bones, insoluble support, and grip sections were printed with compositions of pure HTPLA for the ACL_T specimens and 95% HTPLA blended with 5% NF for the ACL_A specimens. Soluble support models were printed with 100% SC for ACL_T specimen and 95% SC and 5% NF for ACL_A. ACL_T specimens were printed at 100% speed, and ACL_A specimens were printed at 90% speed (*Figure 5.8*).

Filament Hygroscopy

SC filament was mounted in the printer and ran successfully without issue for more than a day of continuous operation; however, despite a dry environment, the filament absorbed enough water from the air to swell and jam in the SC filament inlet. These jams occurred during ACL_T printing and were unable to be resolved during printing. Before ACL_A printing, the SC filament was dried in a PrintDry Filament Dryer (PrintDry, Windsor, ON, CA) set to 45°C and fed from a plastic bag. Despite preventing any further SC filament jams, SC filament dehydration increased the rate of NF filament jams, which was successfully addressed by maintaining 5%v flow of NF into the hotend throughout all print moves (*Figure 5.7*).

Post Processing

FATC specimens were removed from the printbed and processed to remove support material. The zigzag support was manually removed with needle nose pliers, and the specimen were soaked and run under warm water while being scrubbed by a soft bristle brush. This process

took approximately 45 minutes. The specimens were then dehydrated in a PrintDry Filament Dryer (PrintDry, Windsor, ON, CA) set to 50°C for 12 hours.

5.3.6 FATC Tensile Testing

A/P and M/L thickness at ACL center of FATC tensile specimens were measured using calipers. Specimen were painted with spray paint to produce a speckle pattern to assist with measurement from a DIC system running Vic-Gauge Image Correlation Software before being mounted in GW-XT wedge grips within the eXpert 5603 universal testing machine configured for tensile testing and controlled by MTEST Quattro software running on a desktop computer. Grip length was set by fully seating each side of the specimen and adjusting grip position until zero load was achieved (*Figure 5.9*). Loading parameters were configured to match those described by Woo et al (S. L. Woo et al. 1991). Specimen conditioning consisted of ten oscillations between 0 and 2 mm extension at a rate of 20 mm motor displacement per minute, which was immediately followed by load to failure at a load rate of 200 mm motor displacement per minute (*Figure 5.10*). Data was collected at a rate of 100 Hz including tensile force recorded by the SM-1000 load cell and position recorded by the eXpert 5603's motor encoder and the VIC software.

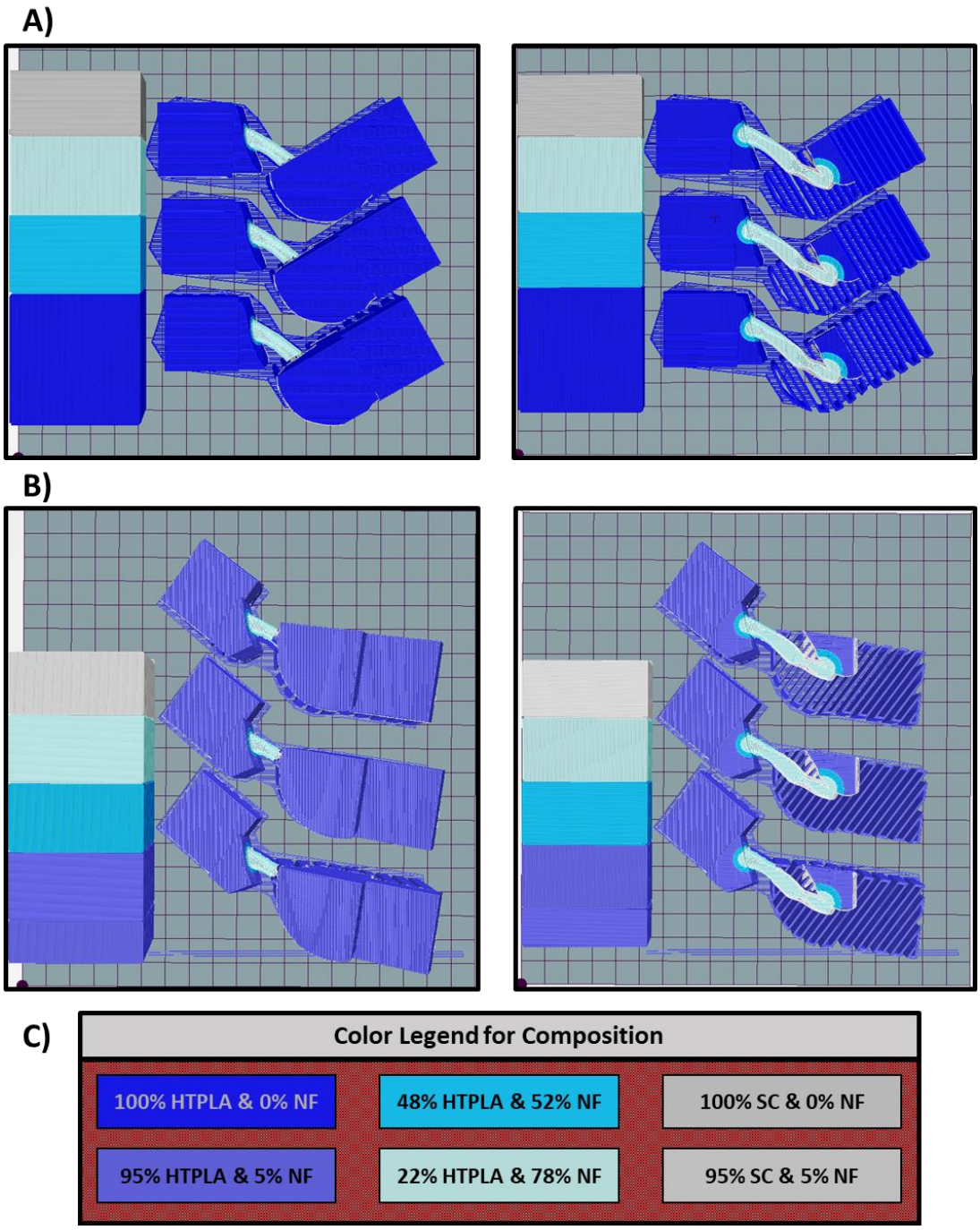

Figure 5.7: Print previews of FATC specimens. A) ACL_T specimens with priming blocks. Whole print is shown on the left. Cross section is shown intersecting the ACL on the right. B) ACL_A specimens with priming blocks. Whole print is shown on the left. Cross section is shown intersecting the ACL on the right. C) Colors on print previews match the composition to be printed.

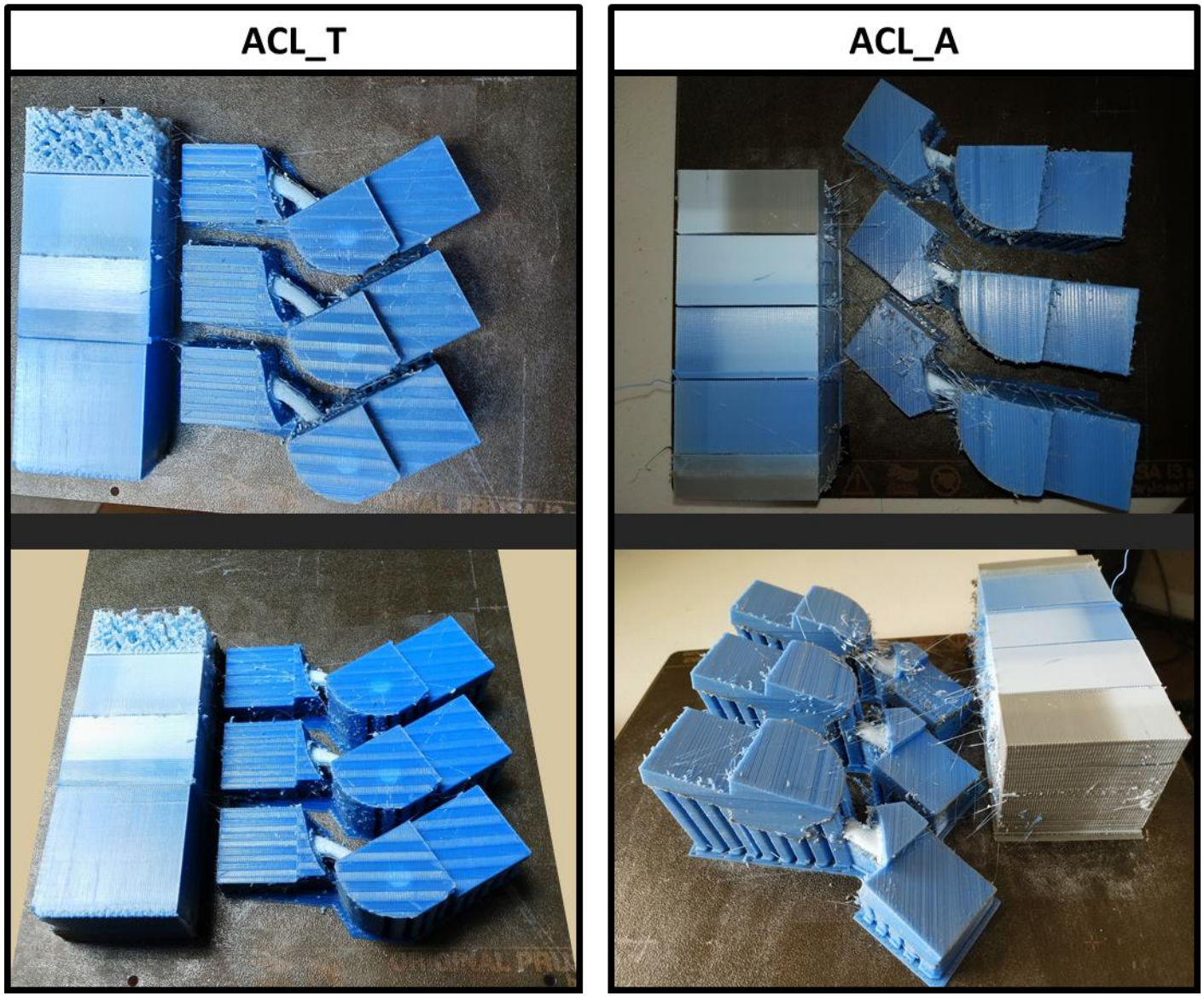

Figure 5.8: Printed FATC specimens on removable print bed.

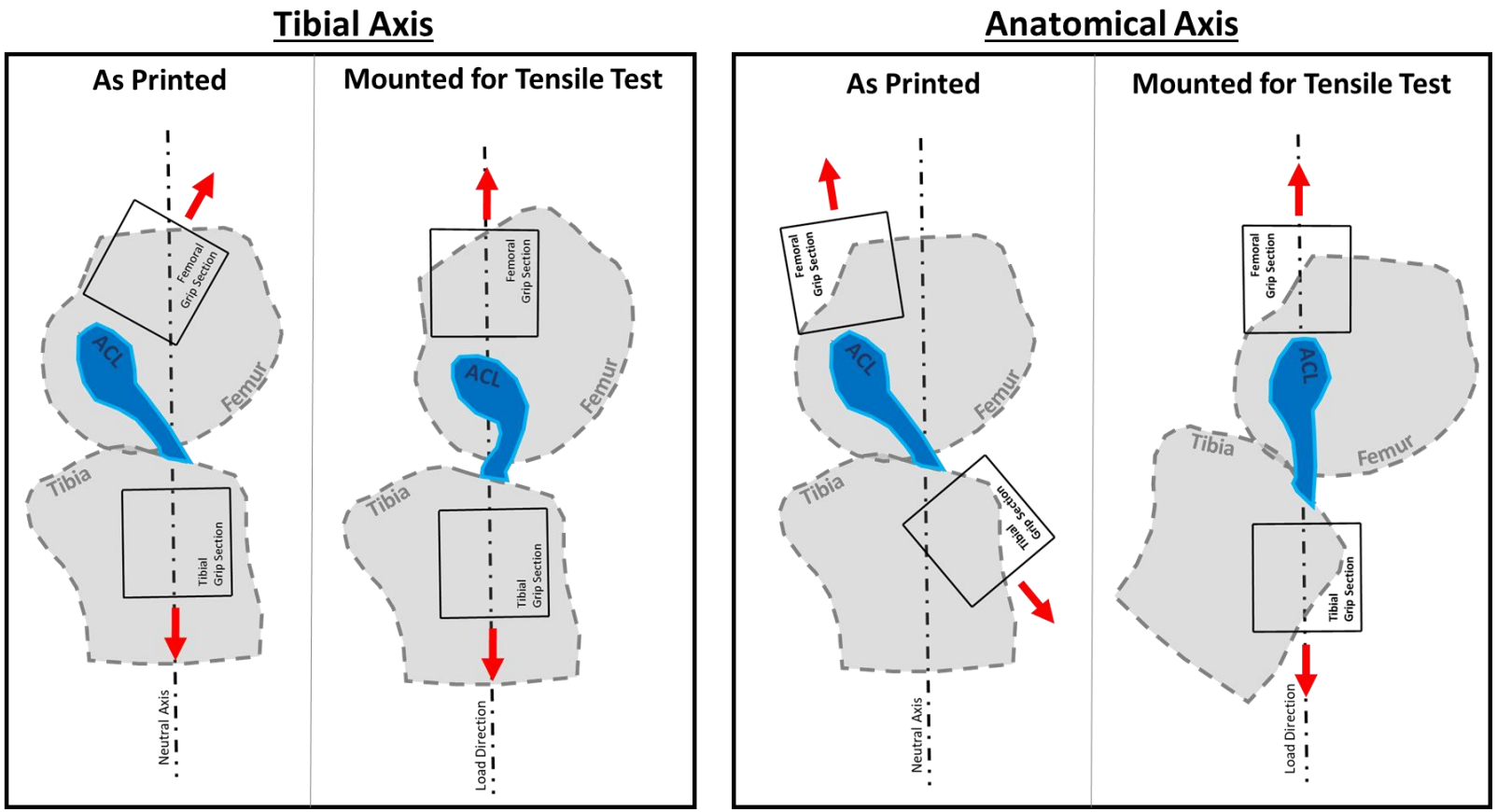

Figure 5.9: Diagrammatic representation of femoral and tibial rotation for mounting FATC specimens for tensile testing.

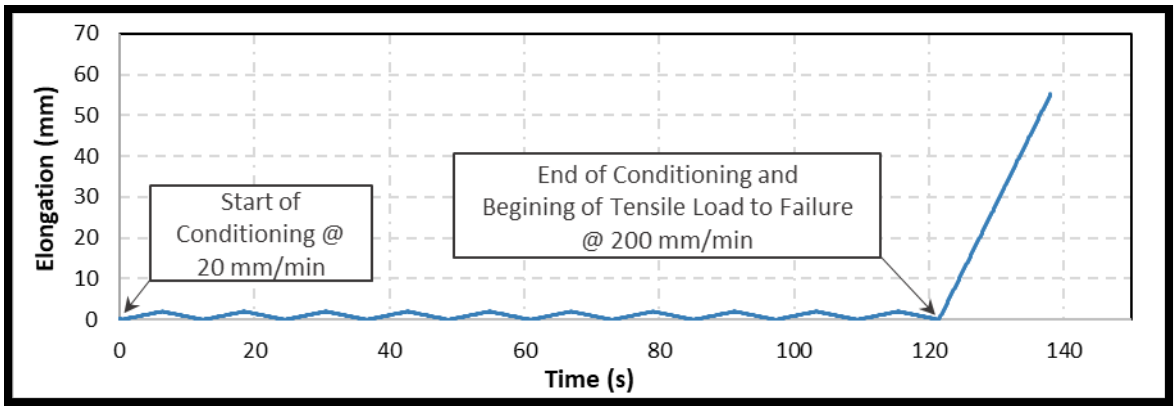

Figure 5.10: Tensile test load profile with 2 mm oscillations for conditioning followed by tensile load to failure.

5.4 Results

5.4.1 Knee Model Design

Three computer knee models with varying structural design were produced by the methods described in sections 5.3.2 and 5.3.3 (*Figures 5.1-3*).

5.4.2 FATC Tensile Test Results

Results from FATC tensile tests are provided in *Table 5.1*. Graphs of tensile force and ACL elongation as measured by DIC are provided in *Figure 5.11*. Graphs of tensile force and ACL elongation as measured by motor position are provided in *Figure 5.12*. Representative fractographic images of ACL_A specimens are provided in *Figures 5.13-14*. Representative fractographic images of ACL_T specimens are provided in *Figures 5.15-18*.

Table 5.1: Synthetic ACL Tensile Test Results

FATC ID	Load Direction	Specimen	Ultimate Load (N)			Stiffness (N/mm)		
			Specimen	Mean	SD	Specimen	Mean	SD
ACL_A	ACL Anatomical Axis	1	265	287	37.0	>45.9	62.8	10.9
		2	267			55.1		
		3	330			70.5		
ACL_T	Tibial Mechanical Axis	1	312	312	6.5	41	43.5	3.4
		2	319			47.4		
		3	306			42.1		

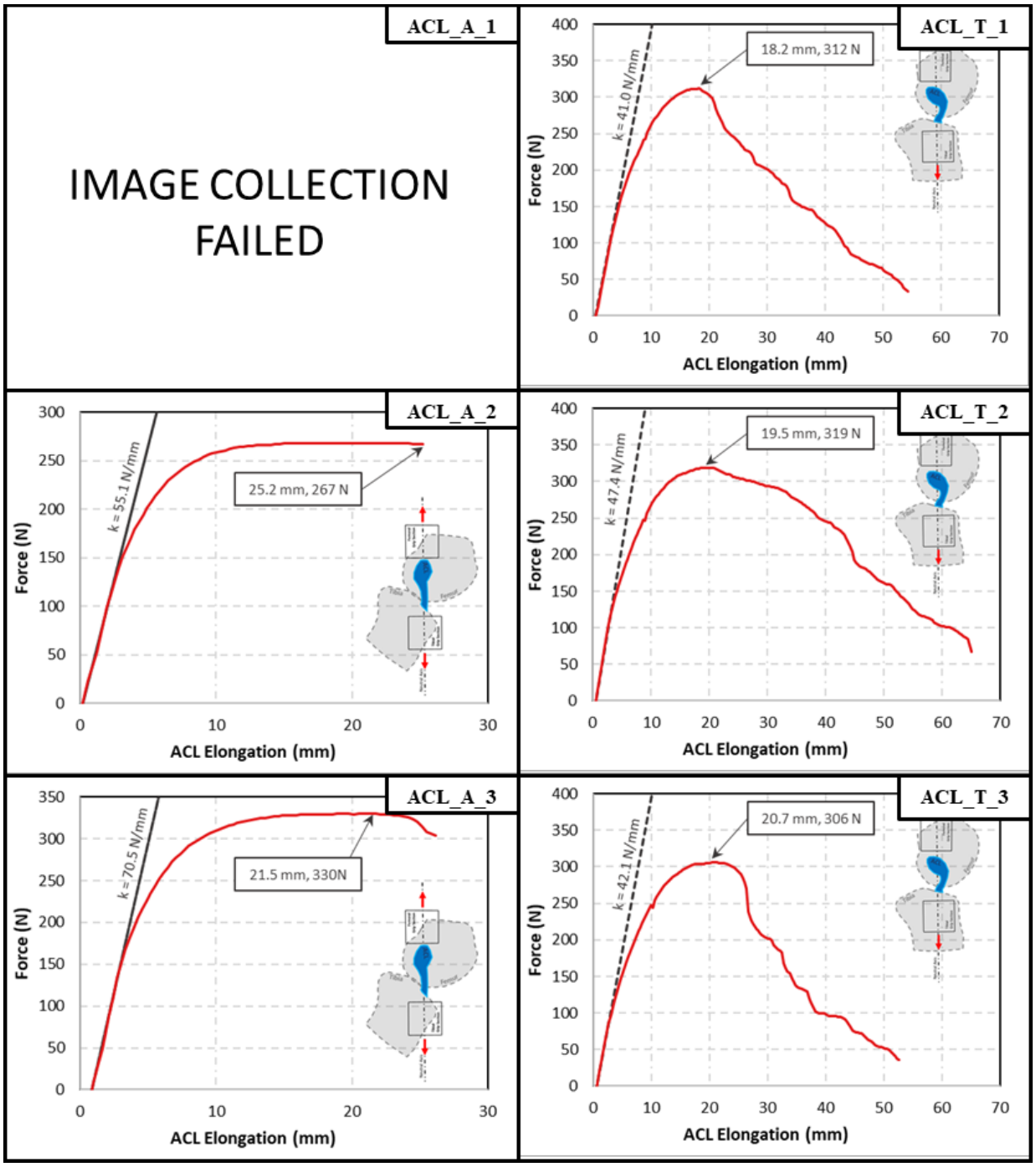

Figure 5.11: Force vs. ACL elongation as measured by DIC.

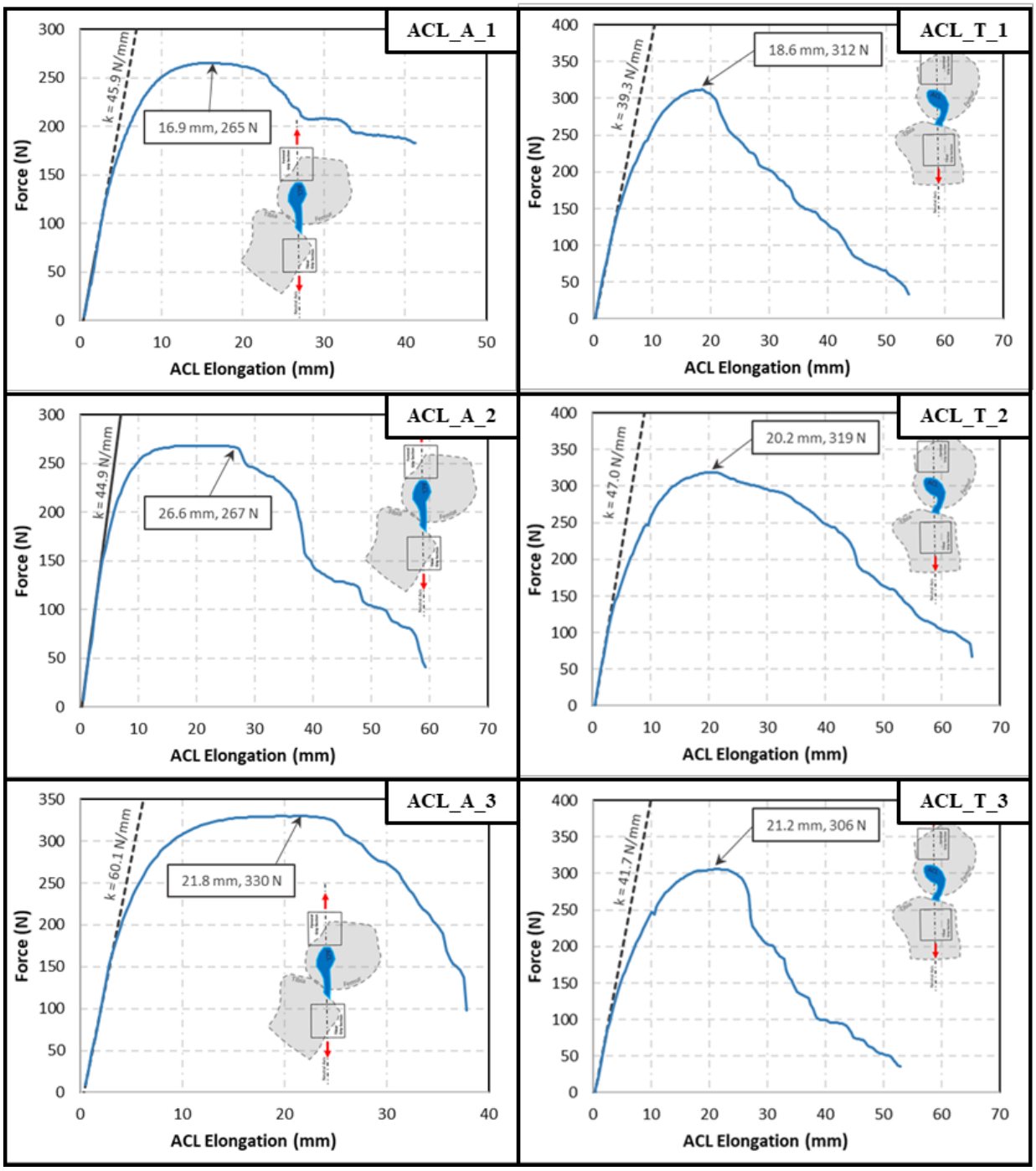

Figure 5.12: Force vs. ACL elongation as measured by motor position.

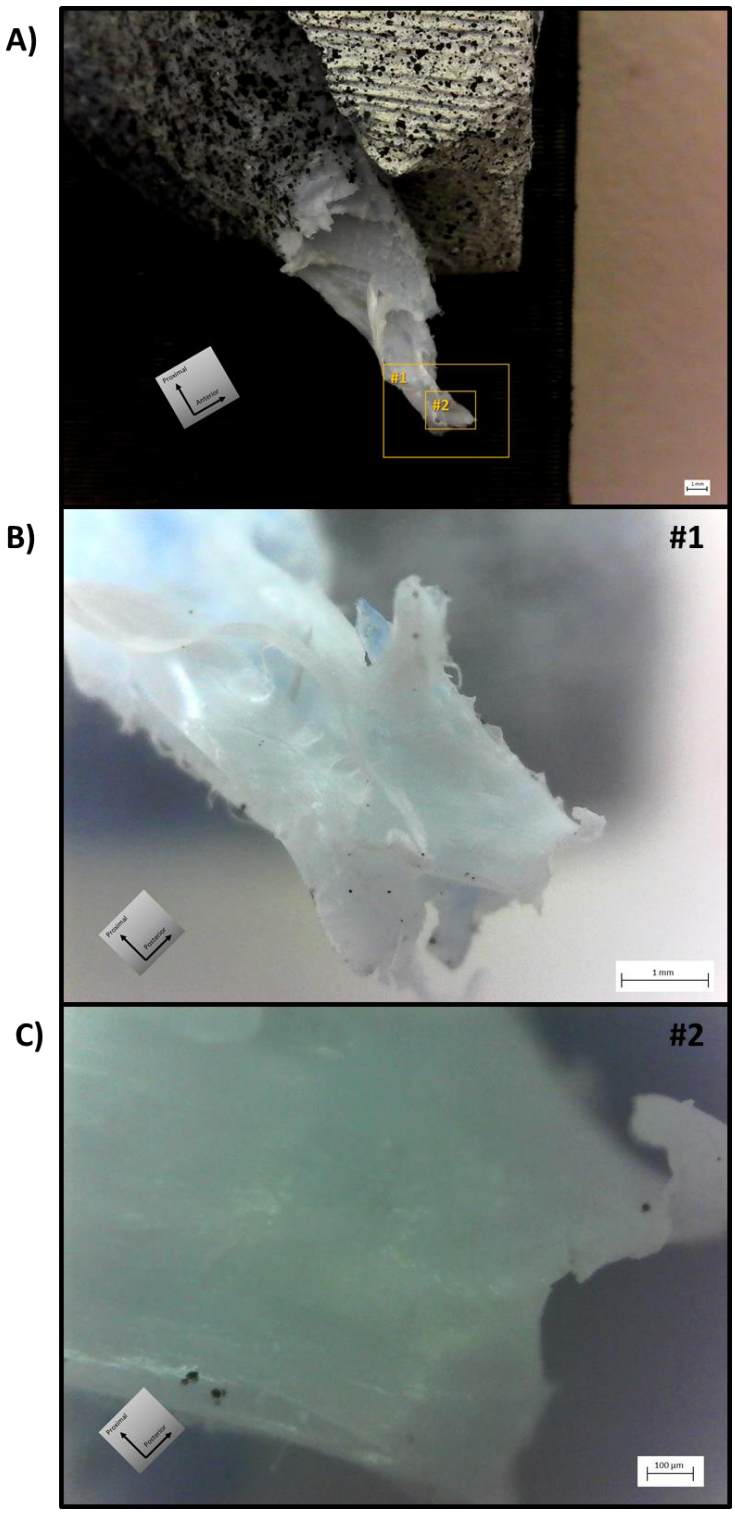

Figure 5.13: Femoral side of fracture surface for ACL_A specimen 1. A) Macroscopic view of femoral fracture surface with detail callouts. B) Detail #1 of the fracture surface. Fibrils and lamellae are visible. Black dots are spray paint particles from speckle pattern applied for DIC. C) Detail #2 of a fractured lamellae Black dots are spray paint particles from speckle pattern applied for DIC.

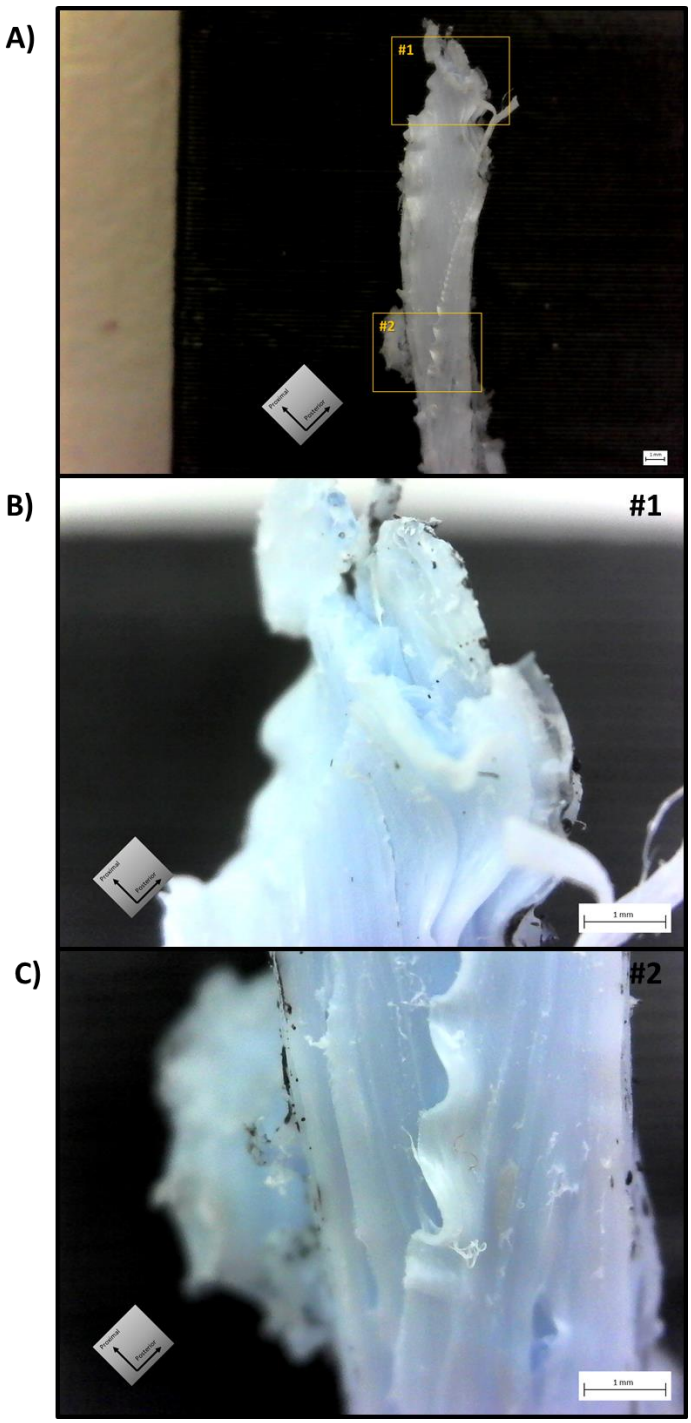

Figure 5.14: Tibial side of fracture surface for ACL_A specimen 1. A) Macroscopic view of tibial fracture surface with detail callouts. B) Detail #1 of the fracture surface. Raster and layer separation are visible. Black dots are spray paint particles from speckle pattern applied for DIC. C) Detail #2 of tibial fracture surface. Infill raster pattern, which was originally perpendicular between layers, is nearly aligned due to plastic deformation and layer separation. Black dots are spray paint particles from speckle pattern applied for DIC.

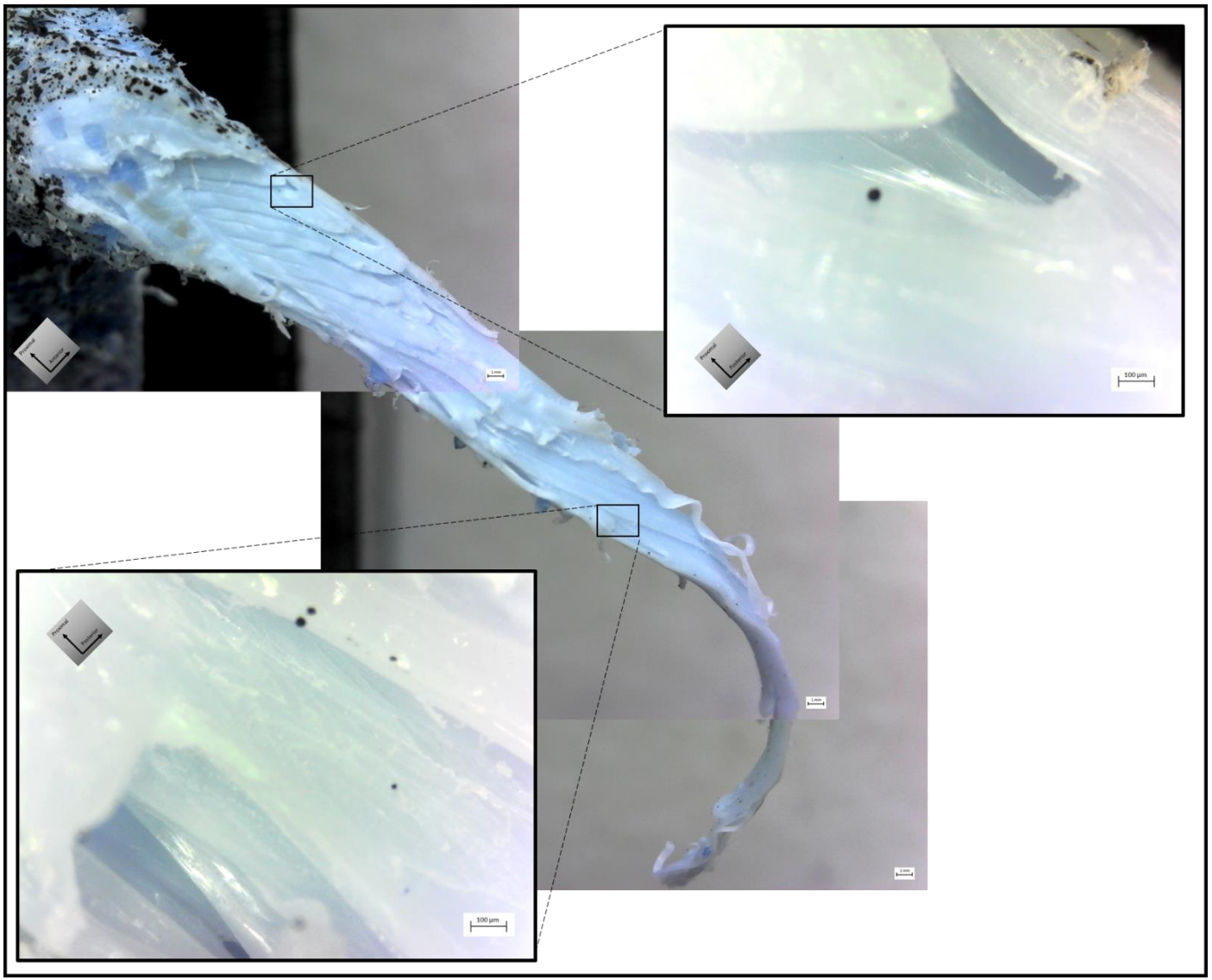

Figure 5.15: Femoral side of fracture surface for ACL_T specimen 3. Layer and raster separation is present throughout the fracture surface. HTPLA deposits from support structure embedded in the ACL are visible in the macroscopic images.

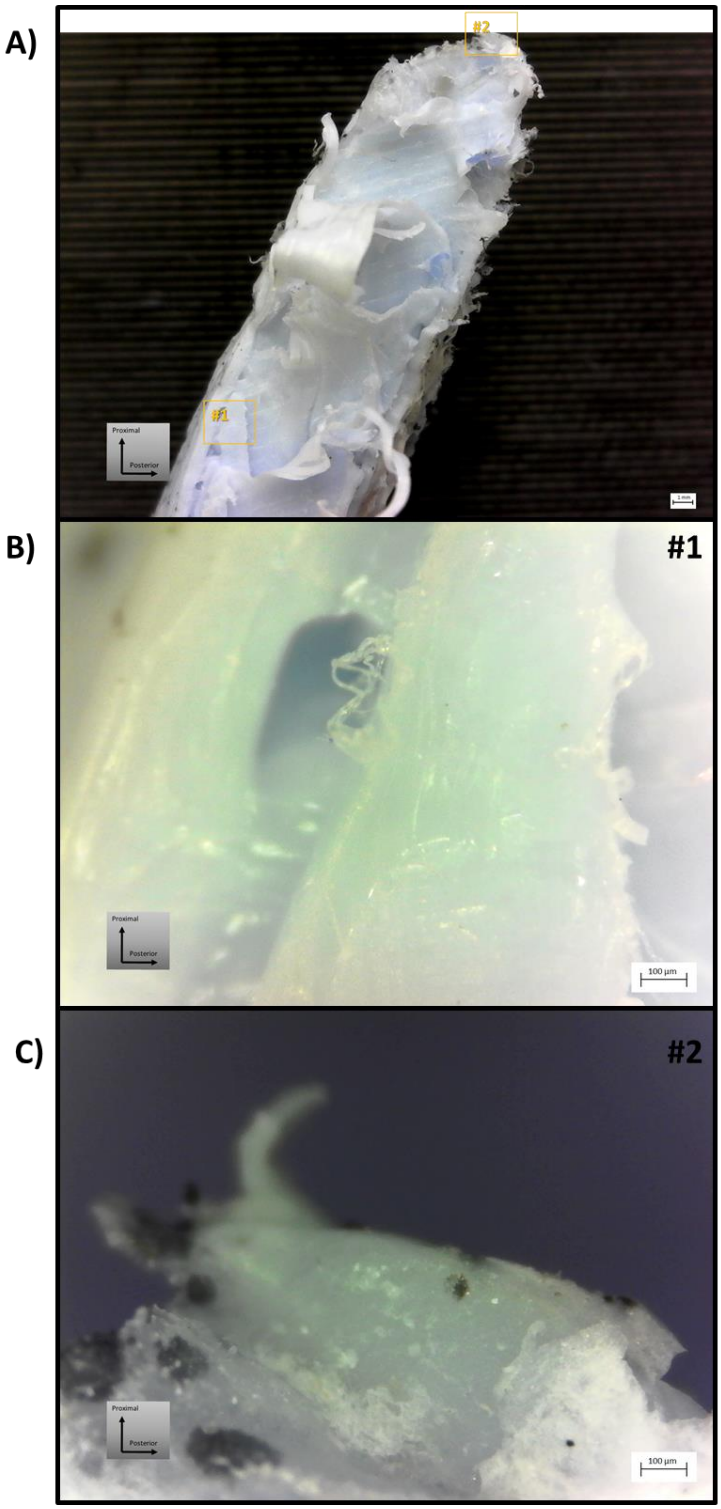

Figure 5.16: Tibial side of fracture surface for ACL_T specimen 3. A) Macroscopic view of tibial fracture surface with detail callouts. B) Detail #1 of the fracture surface. Fibrils and separation of rasters and layers are visible. Black dots are spray paint particles from speckle pattern applied for DIC. C) Detail #2 of tibial fracture surface. Black dots are spray paint particles from speckle pattern applied for DIC.

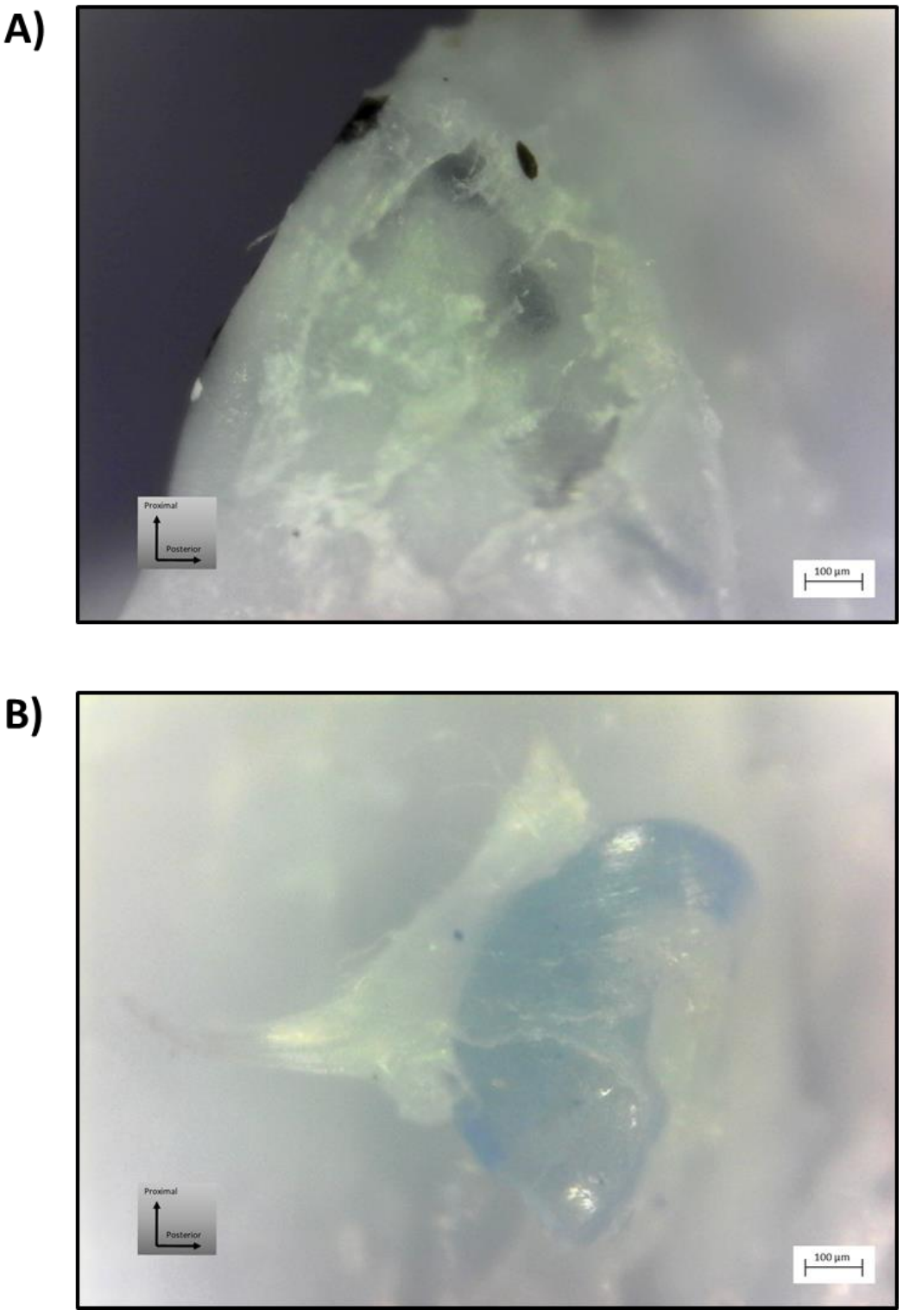

Figure 5.17: Tibial side of fracture surface for specimen 3 of ACL_T. A) PLA particle was pulled out from synthetic ACL. Black dots are spray paint particles from speckle pattern applied for DIC. B) HTPLA particle on surface of fracture surface surrounded by formation of fibrils.

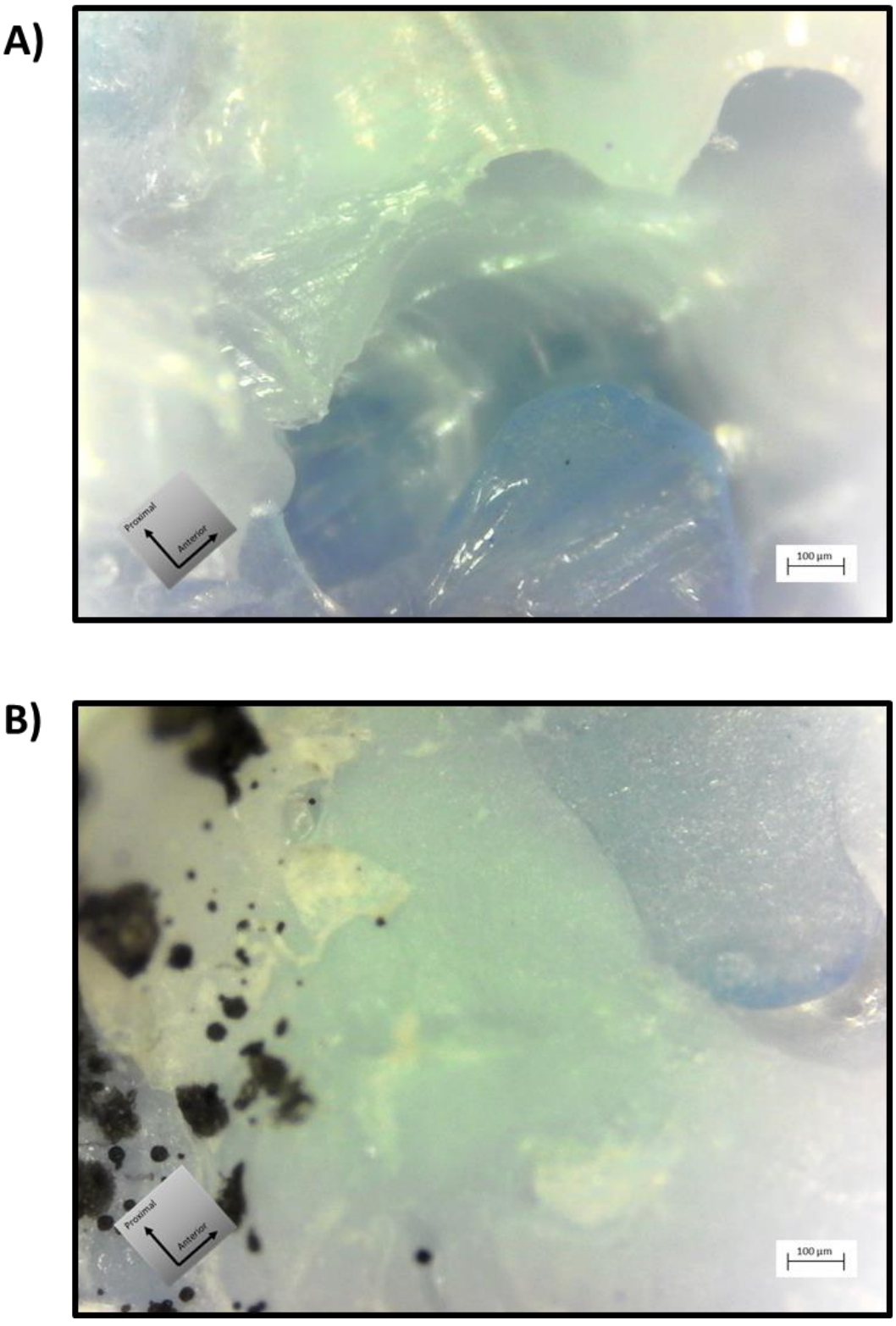

Figure 5.18: Femoral side of fracture surface for specimen 3 of ACL_T. A) HTPLA particle is pulled out from synthetic ACL. B) Synthetic ACL is pulled away from HTPLA particle. Black dots are spray paint particles from speckle pattern applied for DIC.

5.5 Discussion

5.5.1 ACL Tensile Test

Structural Comparison of the Synthetic FATC to a Human FATC

The ACL is a ligamentous structure forming fiber groups usually described as two or more bundles. These bundles vary in properties and do not strain in unison throughout a knee's range of motion. The synthetic ACL of this study does not simulate this fibrous structure, nor does it operate with these same characteristics. While fibers in the human ACL can locally vary from taught to slack and twist around one another during rotation, the synthetic ACL acts as a solid structure by which bending stiffness is affected by characteristics like its area moment of inertia (Dargel et al. 2007).

Stiffness and Ultimate Load

The stiffness and ultimate loads reported by Woo et al. ranged from 124 to 242 N/mm and from 495 to 2160 N, respectively. The specimen tested in this study did not achieve the same stiffness and ultimate loads, which ranged from 41 N/mm to 70.5 N/mm and 265 N to 330 N. Explanations for this deviation in properties include but are not limited to improper assignment of material composition for the geometry of Knee_W, presence of stress concentrators, contamination from SC, material underextrusion, anisotropy due to load direction, anisotropy due to infill pattern, complex loading specific to the synthetic as compared to a human FATC, and yield of materials before tensile load is introduced.

Mechanics of Materials for the Synthetic FATC

Based on linear interpolation of aim 2's results from compositions 12% and 25%, material properties of composition 22%, the composition assigned to the ACL, were estimated to be as follows: E = 290 MPa, σ_Y = 5.87 MPa, $EL\%_Y$ = 2.26%, and UTS = 33.7 MPa. The minimum cross-sectional area of the FATC's ACL design is 40 mm^2, and the length measured from the most anterior point to the most posterior point on the ACL is 45 mm. The length between closest attachment points on the ACL design is 26.9 mm. This geometry is consistent with the mean ACL

length of 32 mm and cross-sections ranging from 34 to 42 mm^2 as reported by Duthon et al. (Duthon et al. 2006).

Using the ACL's minimum cross section and UTS, the synthetic ACL is estimated to have an ultimate load of 1,350 N in pure tension, but all FATC specimen failed at 330 N or less. By treating the ACL as a cylinder with the estimated material properties, a cross-sectional area of 40 mm^2, and length of 45 mm, the ACL would have been estimated to have a minimum tensile stiffness of 255 N/mm before exceeding yield stress.

The synthetic FATC specimens were not nearly as stiff or strong as these basic calculations would predict. This difference between experimental results and theoretical performance can be partly attributed to the complex loading introduced by flexing the specimen 30° and, for the ACL-T specimen, applying a non-axial load.

Bending stress was not analytically determined for this study but the general mechanics of materials for beam deflection and stress provide insight into the performance of the synthetic FATC during these tensile tests. Bending stresses were introduced by forcing the specimen to flex 30°. For an elastic material with this materials E and UTS, the specimen would have failed before it was installed for testing, but because of the low yield stress of this material, flexing the specimen 30° caused local yielding and elongation, which relieved some of the bending load introduced by these constraints. These regions that have yielded have decreased stiffness before any tensile load has been applied (*Figure 5.19*). It is unknown to what extent these effects influenced the results of this study, but these mechanical properties and loading parameters are known to have decreased the effective stiffness and strength of the synthetic FATC as compared to what is expected from pure tensile loads.

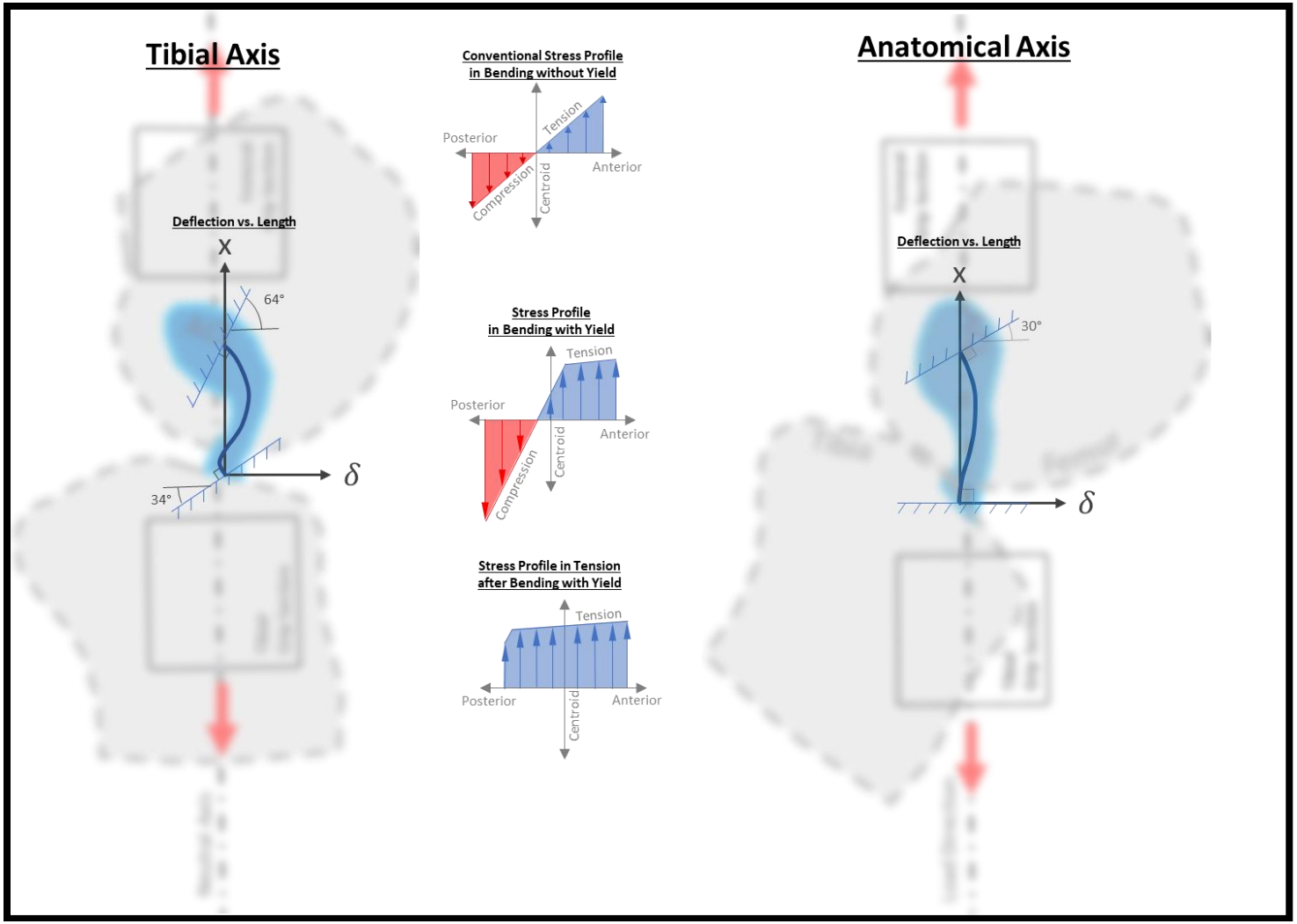

Figure 5.19: Diagram of beam deflection (δ) along the tensile axis (x) and stress profiles at ACL center as mounted for tensile tests. Stress and deflection profiles are representative of bending during installation and are not to scale. Yield due to bending potentially decreases specimen stiffness by decreasing the regions of the ACL that provide a stiff, elastic response to load.

Synthetic FATC Performance Compared to a Human FATC

Despite assigning a composition with an elastic modulus and UTS similar to an ACL, the maximum stiffness and the maximum ultimate loads of the synthetic FATCs were notably less than were recorded in human FATCs. The maximum stiffness observed in the synthetic FATCs was 70.5 N/mm during anatomical loading and is notably less than the average stiffness of younger specimen and even older specimen under the same tensile conditions, which was reported by Woo et al. to be 242 and 180 N/mm, respectively. The ultimate load of the synthetic FATCs did not exceed 330 N and is notably less than the averages of 2,160 N for younger specimen and 658 N for the older specimen as reported by Woo et al. (S. L. Woo et al. 1991). The lower stiffness of the synthetic ACL may alter the kinetics and kinematics of a synthetic knee under physiological loads, but the lower ultimate load may not prevent simulation of some physiological loads with low ACL force and strain. A discussion regarding ACL strain during physiological loads was provided in section 4.5.2. More likely to limit the application of this design for simulating knee kinetics and kinematics is the mechanics of materials related to bending and low yield stress of the materials assigned to the ACL. Under such conditions, permanent deformation of the synthetic ACL will occur during flexion and extension, which will alter the geometry of the ACL and lend it to further plastic deformation if the ACL is synchronously loaded in tension (*Figure 5.20*).

Failure Analysis

Failure did not occur at the tibial insertion site of the ACL, which was the intention for including functional gradients in this design. It is unclear if failure would have occurred at the insertion site without these FGs since no specimen were tested without them. The HTPLA particles that were observed in the ACL_T specimens were not observed in the ACL_A specimens, which can be attributed to the presence of the soluble support in the ACL_A specimens which acted as a barrier between the insoluble support and the ACL (*Figure 5.13-18*). No SC filament was identified in the ACL_A specimens during fractographic analysis though its presence was not able to be ruled out.

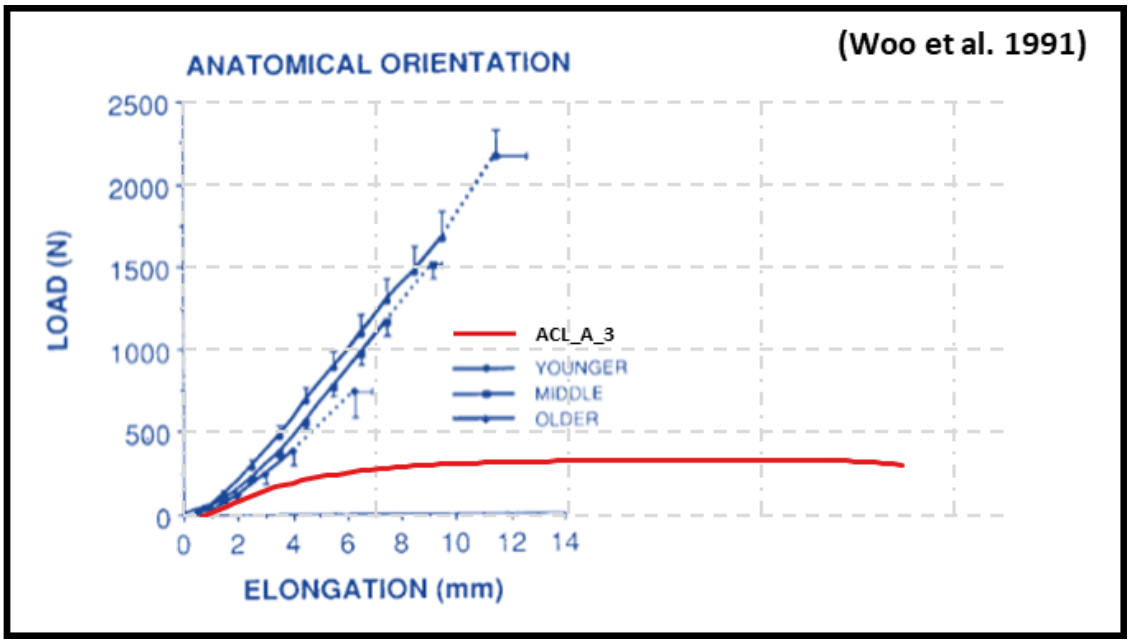

Figure 5.20: Load-elongation graphs of human FATCs loaded in tension along their anatomical axes as extracted from Woo et al. 1991 (blue) with a load-elongation curve of ACL_A specimen 3 (ACL_A_3) overlaid (red). ACL_A_3 does not have a toe region and reached its maximum stiffness of 70.5 N/mm at the start of loading. ACL_A_3 was the stiffest of the synthetic FATCs tested in this study but was not as stiff as the human ACLs tested by Woo et al., which is 242 N/mm for young specimens, 220 N/mm for middle-aged specimens, and 180 N/mm for older specimens. The young, middle-aged, and older specimen tested by Woo et al. reached ultimate loads of 2160 N, 1503 N, and 658 N, respectively. ACL_A_3 had an ultimate load of 330 N which was notably less than the response from human ACL's.

5.5.2 Future Work

An extensive investigation into this technology and methods should be pursued to enable fabrication of a synthetic joint that accurately responds to physiological loads. Future work should include investigation of a synthetic knee during physiological loads, methods to improve accuracy during composition assignment, alternative structural materials, alternative support materials, potential improvements to printer priming and speed through printer design, slicer performance, tribology between simulated articulating surfaces, improved properties through structural design, improved properties through work hardening, and other musculoskeletal joints.

Synthetic Knee and Physiological Load Testing

A knee model has been designed and is ready for fabrication and testing. Some effort to improve the methods described in this study may be desired before fabricating a synthetic knee, but the knee design is ready to be implemented and characterized in the UTJLS. Initial characterization should be performed using a well characterized motion. The squat study described in chapter 3 is an excellent candidate for this work as the UTJLS is configured to apply these loads and two research papers have been published based on the results from these tests. Beyond this proposed initial knee study, other synthetic knees should be designed to match cadaver specimen and undergo identical testing in the UTJLS for a comparative analysis.

Composition Assignment

Composition assignment by only matching modulus of elasticity of a material blend to the modulus of elasticity of a respective biological tissue did not sufficiently simulate the tissue stiffness as desired. Future work may be able to improve upon this method by assimilating a more advanced approach like use of a FE model using the same geometry as the synthetic knee.

Alternative Materials

The materials in this study demonstrated potential but were selected from testing of a limited number of commercially available filaments. Other materials should be investigated for potentially improved performance. Following the results of this study, a combination of material blends with a similar range of stiffness and an increased yield stress would be expected to better match the performance of materials without changing the method of composition assignment. Another potential improvement to material selection may be a revision to the selection of soluble support such that the mixing printer does not jam.

Printer Design

Print speed and reliability are two necessary features for successful printing of a synthetic knee. Three synthetic ACLs took nearly four days to print. Much of this time was spent priming

the printer's nozzle during changes in composition. Improvements made by the printer to improve reliability and decreased priming could significantly decrease the time spent printing.

Slicing

Features like infill raster patterns in this study followed a conventional approach used for general FFF. Individual components of the knee may benefit from infill optimized for its individual function. Future studies should further customize slicer software to provide features like tissue specific infill patterns.

Tribology

As this method is intended to fabricate a synthetic joint including articulating surfaces, future work should investigate tribological properties between those surfaces during physiological loads including an investigation into lubricants to simulate synovial fluid.

Structural Design

Modifications can be made to the internal structure of each tissue to modify its performance. Given that assignment of a stiffer material may be the primary means of increasing ligament stiffness, it may become necessary to introduce structural designs like the core ligament design of section 5.3.1 to decrease the relative bending stiffness of the material.

Improved Properties through Strain Hardening

The heavily plastic behavior observed in this study may be overcome through strain hardening. By loading a polymer beyond its yield stress, the polymer can be hardened and can operate with a larger elastic region upon subsequent loading as is desired for simulation of human tissue. This approach has its limitations since materials are not extruded out of an FFF printer's nozzle in a strain hardened form, and geometric accuracy after strain hardening can be difficult to achieve in a completed part. One future approach may be to alter the geometry of ligaments such that work hardening a ligament may deform the it back into the original geometry.

Other Musculoskeletal Joints

The technology and methods are intended to be applied to all musculoskeletal joints. No aspect of this technology limits its application to human knees alone. Expanded application of this technology to other joints can increase its clinical relevance and broader impacts.

5.6 Conclusion

The methods developed in this study have great potential for advancing synthetic tissue performance and technology; however, limited to the fabrication methods developed in chapter 4, blends of HTPLA and NF with %v HTPLA equal to or less than 25% are limited by a minimal elastic region. Even after adjusting composition assignments to better simulate a tissue's stiffness, the mechanical performance of the synthetic tissue may be easily altered by even simple movements like passive flexion and extension. This challenge may not be insurmountable as the fabrication methods of chapter 4 offer many opportunities for customization and improvement to be investigated in future work.

Chapter 6: Conclusion

6.1 Introduction

The work presented in this dissertation advanced musculoskeletal joint-load simulation, capabilities of LCC during FFF, and techniques for fabrication of synthetic tissue, which collectively are enabling a new branch of biomechanics attempting to invent a synthetic knee that approaches a cadaveric response to physiological loads. This has the potential to revolutionize biomechanics and orthopedic surgery as this work offers an alternative to traditional methods (e.g. *in vivo*, *in vitro*, and computational studies) for investigating knee biomechanics. Unlike anything before, the synthetic knee may be used to practice surgical procedures and receive quantified feedback of changes to joint kinetics and kinematics.

6.2 Aim 1

The UTJLS can simulate physiological loads via *in vitro* musculoskeletal testing including real-time, synchronous application of musculotendon forces and GRF's during multiplanar kinematics. Being the first design of its kind, our simulator utilizes two separate robotic manipulators that contain a total of eight musculotendon actuators and two 6-axis load cells. By adjusting the control scheme configuration, the UTJLS can match the constraints of traditional testing rigs (e.g. oxford rig or robotic arm), recreate absolute motion to reproduce gravitational and inertial loads, and uniquely investigate joint moment contributions from GRF's as demonstrated in this study. With the necessary DOF's, ROM, and speed, the UTJLS is suitable for future testing of faster maneuvers, a variety of human joints, and a kinetic chain of two connected joints (e.g. hip and knee).

6.3 Aim 2

The technology and methods described in this study have advanced FFF by providing a continuous range of material compositions that can be printed within a single layer without user intervention during the printing process. These methods enable fabrication of printed components that were not previously possible. Results from this study indicate that increased strength of FFF

printed parts with binary interfaces may be strengthened by integrating functional gradients into the designs and fabricated using these methods. In addition to characterization of specific materials, the technology of this study can be applied to other materials and has potential applications with variation of other material properties and other materials including those containing fiber and particle reinforcement.

6.4 Aim 3

The methods developed in this study have great potential for advancing synthetic tissue performance and technology; however, limited to the fabrication methods developed in chapter 4, blends of HTPLA and NF with %v HTPLA equal to or less than 25% are limited by a minimal elastic region. Even after adjusting composition assignments to better simulate a tissue's stiffness, the mechanical performance of the synthetic tissue may be easily altered by even simple movements like passive flexion and extension. This challenge may not be insurmountable as the fabrication methods of chapter 4 offer many opportunities for customization and improvement to be investigated in future work.

References

Anderson, Michael C., Nicholas A T Brown, Kent N. Bachus, and Bruce A. MacWilliams. 2009. "A Cadaver Knee Simulator to Evaluate the Biomechanics of Rectus Femoris Transfer." *Gait and Posture* 30 (1): 87–92. doi:10.1016/j.gaitpost.2009.03.007.

Arami, Arash, Matteo Simoncini, Oguz Atasoy, Willyan Hasenkamp, Shafqat Ali, Arnaud Bertsch, Eric Meurville, et al. 2011. "Instrumented Prosthesis for Knee Implants Monitoring." In *IEEE International Conference on Automation Science and Engineering*, 828–35. doi:10.1109/CASE.2011.6042490.

ASTM International. ASTM D2095-96(2015) Standard Test Method for Tensile Strength of Adhesives by Means of Bar and Rod Specimens. West Conshohocken, PA; ASTM International, 2015. doi: https://doi.org/10.1520/D2095-96R15

ASTM International. ASTM D3528-96(2016) Standard Test Method for Strength Properties of Double Lap Shear Adhesive Joints by Tension Loading. West Conshohocken, PA; ASTM International, 2016. doi: https://doi.org/10.1520/D3528-96R16

ASTM International. ASTM D638-14 Standard Test Method for Tensile Properties of Plastics. West Conshohocken, PA; ASTM International, 2014. doi: https://doi.org/10.1520/D0638-14

Bagge, E., A. Bjelle, H. A. Valkenburg, and A. Svanborg. 1992. "Prevalence of Radiographic Osteoarthritis in Two Elderly European Populations." *Rheumatology International* 12 (1): 33–38. doi:10.1007/BF00246874.

Baich, Liseli, and Guha Manogharan. 2015. "Study of Infill Print Parameters on Mechanical Strength and Production Cost-Time of 3D Printed ABS Parts," 209–18.

Bartlett, Nicholas W, Michael T Tolley, Johannes T B Overvelde, James C Weaver, Bobak Mosadegh, Katia Bertoldi, George M Whitesides, and Robert J Wood. 2015. "Robot Powered By Combustion," no. May 2015.

Bates, Nathaniel A., Kevin R. Ford, Gregory D. Myer, and Timothy E. Hewett. 2013. "Impact Differences in Ground Reaction Force and Center of Mass between the First and Second Landing Phases of a Drop Vertical Jump and Their Implications for Injury Risk Assessment." *Journal of Biomechanics* 46 (7): 1237–41. doi:10.1016/j.jbiomech.2013.02.024.

Bates, Nathaniel A., Gregory D. Myer, Jason T. Shearn, and Timothy E. Hewett. 2015. "Anterior Cruciate Ligament Biomechanics during Robotic and Mechanical Simulations of Physiologic and Clinical Motion Tasks: A Systematic Review and Meta-Analysis." *Clinical Biomechanics* 30 (1). Elsevier Ltd: 1–13. doi:10.1016/j.clinbiomech.2014.12.006.

Bates, Nathaniel A., Rebecca J. Nesbitt, Jason T. Shearn, Gregory D. Myer, and Timothy E. Hewett. 2015. "A Novel Methodology for the Simulation of Athletic Tasks on Cadaveric Knee Joints with Respect to In Vivo Kinematics." *Annals of Biomedical Engineering* 43 (10): 2456–66. doi:10.1007/s10439-015-1285-8.

Becke, Mark, and Thomas Schlegl. 2011. "Toward an Experimental Method for Evaluation of Biomechanical Joint Behavior under High Variable Load Conditions." In *Proceedings* -

IEEE International Conference on Robotics and Automation, 3370–75. doi:10.1109/ICRA.2011.5979598.

Bellini, Anna, and Selçuk Güçeri. 2003. "Mechanical Characterization of Parts Fabricated Using Fused Deposition Modeling." *Rapid Prototyping Journal* 9 (4): 252–64. doi:10.1108/13552540310489631.

Bergmann, Georg, Alwina Bender, Friedmar Graichen, J??rn Dymke, Antonius Rohlmann, Adam Trepczynski, Markus O Heller, and Ines Kutzner. 2014. "Standardized Loads Acting in Knee Implants." *PLoS ONE* 9 (1). doi:10.1371/journal.pone.0086035.

Beynnon, Bruce D., Robert J. Johnson, Braden C. Fleming, Charles J. Stankewich, Per A. Renstrom, and Claude E. Nichols. 1997. "The Strain Behavior of the Anterior Cruciate Ligament During Squatting and Active Flexion-Extension." *Sports Medicine* 25 (6): 823–29.

BIPM, IEC, ILAC IFCC, and IUPAC ISO. IUPAP, and OIML, 2008,"Evaluation of Measurement Data—Guide to the Expression of Uncertainty in Measurement," Joint Committee for Guides in Metrology. Technical Report No. JCGM 100, 2008.

Bonner, Timothy J., Nicolas Newell, Angelo Karunaratne, Andy D. Pullen, Andrew A. Amis, Anthony M.J. Bull, and Spyros D. Masouros. 2015. "Strain-Rate Sensitivity of the Lateral Collateral Ligament of the Knee." *Journal of the Mechanical Behavior of Biomedical Materials* 41. Elsevier: 261–70. doi:10.1016/j.jmbbm.2014.07.004.

Burr, David B., C. Milgrom, D. Fyhrie, M. Forwood, M. Nyska, A. Finestone, S. Hoshaw, E. Saiag, and A. Simkin. 1996. "In Vivo Measurement of Human Tibial Strains during Vigorous Activity." *Bone* 18 (5): 405–10. doi:10.1016/8756-3282(96)00028-2.

Butler, David L., Yuning Guan, Matthew D. Kay, John F. Cummings, Seth M. Feder, and Martin S. Levy. 1992. "Location-Dependent Variations in the Material Properties of the Anterior Cruciate Ligament." *Journal of Biomechanics* 25 (5): 511–18. doi:10.1016/0021-9290(92)90091-E.

Butler, DL. 1986. "Fascicle-Bone Units From Human Patellar Tendon and Knee Ligaments." *Journal of Biomechanics* 19 (6): 425–32. doi:https://doi.org/10.1016/0021-9290(86)90019-9.

Cassidy, Karla, Gajendra Hangalur, Preet Sabharwal, and Naveen Chandrashekar. 2013. "Combined in Vivo/in Vitro Method to Study Anteriomedial Bundle Strain in the Anterior Cruciate Ligament Using a Dynamic Knee Simulator." *Journal of Biomechanical Engineering* 135 (3): 35001. doi:10.1115/1.4023520.

Chia, Helena N., and M. L. Hull. 2008. "Compressive Moduli of the Human Medial Meniscus in the Axial and Radial Directions at Equilibrium and at a Physiological Strain Rate." *Journal of Orthopaedic Research* 26 (7): 951–56. doi:10.1002/jor.20573.

Choi, K., J. L. Kuhn, M. J. Ciarelli, and S. A. Goldstein. 1990. "The Elastic Moduli of Human Subchondral, Trabecular, and Cortical Bone Tissue and the Size-Dependency of Cortical Bone Modulus." *Journal of Biomechanics* 23 (11): 1103–13. doi:10.1016/0021-9290(90)90003-L.

Chowdhuri, M. A K, and Z. Xia. 2013. “Interface Bonding Strength Measurement of a Joint between Elastic and Viscoelastic Materials.” *Composites Part B: Engineering* 44 (1). Elsevier Ltd: 253–59. doi:10.1016/j.compositesb.2012.05.027.

Corbett, James. 2012. “Reprap Colour Mixing Project” 3: 122. http://www.reprap.org/mediawiki/images/0/05/RepRapColourMixingReport-jmc.pdf.

Coward, Cameron. 2015. “3D Printing.” *Penguin*. https://books.google.com/books?hl=en&lr=&id=N1cpBgAAQBAJ&oi=fnd&pg=PT18&dq=fdm+ghosting+printer&ots=TzDvhi5TiL&sig=zH9A4zyv87kFezSL2GX-UsUPQL8#v=onepage&q&f=false.

Dargel, J., M. Gotter, K. Mader, D. Pennig, J. Koebke, and R. Schmidt-Wiethoff. 2007. “Biomechanics of the Anterior Cruciate Ligament and Implications for Surgical Reconstruction.” *Strategies in Trauma and Limb Reconstruction* 2 (1): 1–12. doi:10.1007/s11751-007-0016-6.

Dienst, Michael, Robert T. Burks, and Patrick E. Greis. 2002. “Anatomy and Biomechanics of the Anterior Cruciate Ligament.” *Orthopedic Clinics of North America* 33 (4): 605–20. doi:10.1016/S0030-5898(02)00010-X.

Dunning, Cynthia E., Karen D. Gordon, Graham J W King, and James A. Johnson. 2003. “Development of a Motion-Controlled in Vitro Elbow Testing System.” *Journal of Orthopaedic Research* 21 (3): 405–11. doi:10.1016/S0736-0266(02)00233-4.

Durairaj, R.B, M Sivasankar, and A Krishnamoorthy. 2014. “Modelling and Simulation of Knee Simulator Testing Machine Using Lab View.” *International Journal of Current Engineering and Technology*.

Duthon, V. B., C. Barea, S. Abrassart, J. H. Fasel, D. Fritschy, and J. Ménétrey. 2006. “Anatomy of the Anterior Cruciate Ligament.” *Knee Surgery, Sports Traumatology, Arthroscopy* 14 (3): 204–13. doi:10.1007/s00167-005-0679-9.

Ellman, Michael B, Christopher M LaPrade, Sean D Smith, Matthew T Rasmussen, Lars Engebretsen, Coen A Wijdicks, and Robert F LaPrade. 2014. “Structural Properties of the Meniscal Roots.” *The American Journal of Sports Medicine* 42 (8): 1881–87. doi:10.1177/0363546514531730.

Fedorov, Andriy, Reinhard Beichel, Jayashree Kalpathy-Cramer, Julien Finet, Jean Christophe Fillion-Robin, Sonia Pujol, Christian Bauer, et al. 2012. “3D Slicer as an Image Computing Platform for the Quantitative Imaging Network.” *Magnetic Resonance Imaging* 30 (9). Elsevier Inc.: 1323–41. doi:10.1016/j.mri.2012.05.001.

Fredieu, John R., Jennifer Kerbo, Mark Herron, Ryan Klatte, and Malcolm Cooke. 2015. “Anatomical Models: A Digital Revolution.” *Medical Science Educator* 25 (2): 183–94. doi:10.1007/s40670-015-0115-9.

Fujie, Hiromichi, Takeshi Sekito, and Akiyuki Orita. 2004. “A Novel Robotic System for Joint Biomechanical Tests: Application to the Human Knee Joint.” *Journal of Biomechanical Engineering* 126 (1): 54–61. doi:10.1115/1.1644567.

Gibson, Ian, David Rosen, and Brent Stucker. 2015. “Development of Additive Manufacturing Technology.” In *Additive Manufacturing Technologies*, 19–42. New York, NY: Springer New York. doi:10.1007/978-1-4939-2113-3_2.

Gillam, M. H., S. A. Lie, A. Salter, O. Furnes, S. E. Graves, L. I. Havelin, and P. Ryan. 2013. “The Progression of End-Stage Osteoarthritis: Analysis of Data from the Australian and Norwegian Joint Replacement Registries Using a Multi-State Model.” *Osteoarthritis and Cartilage* 21 (3). Elsevier Ltd: 405–12. doi:10.1016/j.joca.2012.12.008.

Glüer, C. C., G. Blake, Y. Lu, B. A. Blunt1, M. Jergas1, and H. K. Genant1. 1995. “Accurate Assessment of Precision Errors: How to Measure the Reproducibility of Bone Densitometry Techniques.” *Osteoporosis International* 5 (4): 262–70. doi:10.1007/BF01774016.

Goldsmith, Mary T., Sean D. Smith, Kyle S. Jansson, Robert F. LaPrade, and Coen A. Wijdicks. 2014. “Characterization of Robotic System Passive Path Repeatability during Specimen Removal and Reinstallation for in Vitro Knee Joint Testing.” *Medical Engineering and Physics* 36 (10). Institute of Physics and Engineering in Medicine: 1331–37. doi:10.1016/j.medengphy.2014.06.022.

Green, Joshua T, Rena F Hale, Jerome Hausselle, and Roger V Gonzalez. 2017. “A Reconfigurable Multiplanar in Vitro Simulator for Real-Time Absolute Motion with External and Musculotendon Forces.” *Journal of Biomechanical Engineering*, no. c. doi:10.1115/1.4037853.

Griffin, L. Y. 2006. “Understanding and Preventing Noncontact Anterior Cruciate Ligament Injuries: A Review of the Hunt Valley II Meeting, January 2005.” *American Journal of Sports Medicine* 34 (9): 1512–32. doi:10.1177/0363546506286866.

Grood, E S, and W J Suntay. 1983. “A Joint Coordinate System for the Clinical Description of Three-Dimensional Motions: Application to the Knee.” *Journal of Biomechanical Engineering*. doi:10.1115/1.3138397.

Hale, Rena, Joshua Green, Jerome Hausselle, David Saxby, and Roger V. Gonzalez. 2018. “Quantified in Vitro Tibiofemoral Contact during Bodyweight Back Squats.” *Journal of Biomechanics* 79. Elsevier Ltd: 21–30. doi:10.1016/j.jbiomech.2018.07.002.

Han, Shanling, Yu Xiao, Tao Qi, Zhiyong Li, and Qingliang Zeng. 2017. “Design and Analysis of Fused Deposition Modeling 3D Printer Nozzle for Color Mixing.” *Advances in Materials Science and Engineering* 2017. doi:10.1155/2017/2095137.

Harley, Brendan A., Janet H. Leung, Emilio C C M Silva, and Lorna J. Gibson. 2007. “Mechanical Characterization of Collagen-Glycosaminoglycan Scaffolds.” *Acta Biomaterialia* 3 (4): 463–74. doi:10.1016/j.actbio.2006.12.009.

Hausselle, J, Aa Assi, A El Helou, E Jolivet, H Pillet, E Dion, D Bonneau, and W Skalli. 2012. “Subject-Specific Musculoskeletal Model of the Lower Limb in a Lying and Standing Position.” *Computer Methods in Biomechanics and Biomedical Engineering* 17 (November 2014): 37–41. doi:10.1080/10255842.2012.693173.

Hergel, Jean, and Sylvain Lefebvre. 2014. “Clean Color: Improving Multi-Filament 3D Prints.” *Computer Graphics Forum* 33 (2): 469–78. doi:10.1111/cgf.12318.

Hockaday, L A, K H Kang, N W Colangelo, P Y C Cheung, B Duan, E Malone, J Wu, et al. 2012. “Rapid 3D Printing of Anatomically Accurate and Mechanically Heterogeneous Aortic Valve Hydrogel Scaffolds.” *Biofabrication* 4 (3): 035005. doi:10.1088/1758-5082/4/3/035005.

Hortobágyi, Tibor, Lenna Westerkamp, Stacey Beam, Jill Moody, Joseph Garry, Donald Holbert, and Paul DeVita. 2005. “Altered Hamstring-Quadriceps Muscle Balance in Patients with Knee Osteoarthritis.” *Clinical Biomechanics* 20 (1): 97–104. doi:10.1016/j.clinbiomech.2004.08.004.

Howard, Ryan A, Joshua M Rosvold, Shon P Darcy, David T Corr, Janet E Tapper, Canada Tn, Jillian E Beveridge, and Cyril B Frank. 2007. “Reproduction of In Vivo Motion Using a Parallel Robot.” *Journal of Biomechanical Engineering* 129 (October): 743–49. doi:10.1115/1.2768983.

Lan, Hongbo. 2017. “Active Mixing Nozzle for Multi-Material and Multi-Scale 3D Printing.” In *Volume 2: Additive Manufacturing; Materials*, V002T01A024. ASME. doi:10.1115/MSEC2017-2779.

Lanyon, L E, W G Hampson, a E Goodship, and J S Shah. 1975. “Bone Deformation Recorded in Vivo from Strain Gauges Attached to the Human Tibial Shaft.” *Acta Orthopaedica Scandinavica* 46 (2): 256–68. doi:10.3109/17453677508989216.

Lauke, Bernd. 2007. “Stress Concentration along Curved Interfaces as Basis for Adhesion Tests.” *Composite Interfaces* 14 (4): 307–20. doi:10.1163/156855407780452887.

Lauke, Bernd, Tobias Schüller, and Konrad Schneider. 2012. “Determination of the Interface Strength between Two Polymer Materials by a New Curved Interface Tensile Test : Preliminary Experimental Results” 5543 (June): 37–41. doi:10.1163/156855403322667287.

Lee, C. S., S. G. Kim, H. J. Kim, and S. H. Ahn. 2007. “Measurement of Anisotropic Compressive Strength of Rapid Prototyping Parts.” *Journal of Materials Processing Technology* 187–188: 627–30. doi:10.1016/j.jmatprotec.2006.11.095.

Leichtle, Ulf G., Markus Wünschel, Carmen I. Leichtle, Otto Müller, Philipp Kohler, Nikolaus Wülker, and Andrea Lorenz. 2014. “Increased Patellofemoral Pressure after TKA: An in Vitro Study.” *Knee Surgery, Sports Traumatology, Arthroscopy* 22 (3): 500–508. doi:10.1007/s00167-013-2372-8.

Lužanin, Ognjan, Dejan Movrin, and Miroslav Plan. 2014. “Effect of Layer Thickness , Deposition Angle , and Infill on Maximum Flexural Force in Fdm-Built Specimens.” *Journal for Technology of Plasticity* 39 (1): 49–58. http://www.dpm.ftn.uns.ac.rs/jtp/download/2014/1/Article6.pdf.

Mahamood, Rasheedat Modupe, and Esther Titilayo Akinlabi. 2017. *Types of Functionally Graded Materials and Their Areas of Application*. *Functionally Graded Materials*. Vol. 2–2. doi:10.1007/978-3-319-53756-6.

Maker Geeks, “HTPLA Raptor - High Performance PLA 3D Filament - HD Blue Steel - 1.75 – Maker Geeks 3D Printing Filaments.” makergeeks.com. Accessed November 18, 2018. https://www.makergeeks.com/products/raptor-series-pla-high-performance-3d-filament-hd-blue-steel-175mm-1kg.

Makris, Eleftherios A., Pasha Hadidi, and Kyriacos A. Athanasiou. 2011. “The Knee Meniscus: Structure-Function, Pathophysiology, Current Repair Techniques, and Prospects for Regeneration.” *Biomaterials* 32 (30). Elsevier Ltd: 7411–31. doi:10.1016/j.biomaterials.2011.06.037.

Maletsky, Lorin P., and Ben M. Hillberry. 2005a. “Simulating Dynamic Activities Using a Five-Axis Knee Simulator.” *Journal of Biomechanical Engineering* 127 (1): 123. doi:10.1115/1.1846070.

Maletsky, Lorin P, and Ben M Hillberry. 2005b. “Simulating Dynamic Activities Using a Five-Axis Knee Simulator.” *Journal of Biomechanical Engineering* 127 (1): 123–33. doi:10.1115/1.1846070.

Mansouri, M. R., H. Montazerian, S. Schmauder, and J. Kadkhodapour. 2018. “3D-Printed Multimaterial Composites Tailored for Compliancy and Strain Recovery.” *Composite Structures* 184 (December 2016). Elsevier: 11–17. doi:10.1016/j.compstruct.2017.09.049.

Mathieu, Laurence Marcelle, Thomas L Mueller, Pierre-Etienne Bourban, Dominique P Pioletti, Ralph Müller, and Jan-Anders E Månson. 2006. “Architecture and Properties of Anisotropic Polymer Composite Scaffolds for Bone Tissue Engineering.” *Biomaterials* 27 (6): 905–16. doi:10.1016/j.biomaterials.2005.07.015.

McDermott, Ian D., Spyridon D. Masouros, and Andrew A. Amis. 2008. “Biomechanics of the Menisci of the Knee.” *Current Orthopaedics* 22 (3): 193–201. doi:10.1016/j.cuor.2008.04.005.

Miller, Emily J., Rose F. Riemer, Tammy L. Haut Donahue, and Kenton R. Kaufman. 2009. “Experimental Validation of a Tibiofemoral Model for Analyzing Joint Force Distribution.” *Journal of Biomechanics* 42 (9): 1355–59. doi:10.1016/j.jbiomech.2009.03.019.

Mills, Kathryn, Blayne A. Hettinga, Michael B. Pohl, and Reed Ferber. 2013. “Between-Limb Kinematic Asymmetry during Gait in Unilateral and Bilateral Mild to Moderate Knee Osteoarthritis.” *Archives of Physical Medicine and Rehabilitation* 94 (11). Elsevier: 2241–47. doi:10.1016/j.apmr.2013.05.010.

Murr, Lawrence E., Sara M. Gaytan, Edwin Martinez, Frank Medina, and Ryan B. Wicker. 2012. “Next Generation Orthopaedic Implants by Additive Manufacturing Using Electron Beam Melting.” *International Journal of Biomaterials* 2012. doi:10.1155/2012/245727.

Neogi, Tuhina. 2013. “Epidemiology of Osteoarthritis Osteoarthritis Epidemiology Risk Factors Pain.” *Rheumatic Disease Clinics of NA* 39 (1): 1–19. doi:10.1016/j.rdc.2012.10.004.

“NinjaFlex 3D Printing Filament.” 2018. Accessed November 1. https://ninjatek.com/wp-content/uploads/2016/05/NinjaFlex-TDS.pdf.

Noble, Lawrence D, Robb W Colbrunn, Dong-gil Lee, Antonie J van den Bogert, and Brian L Davis. 2010. “Design and Validation of a General Purpose Robotic Testing System for Musculoskeletal Applications.” *Journal of Biomechanical Engineering* 132 (2): 025001. doi:10.1115/1.4000851.

Ochi, Mitsuo, Konsei Shino, Kazunori Yasuda, and Masahiro Kurosaka. 2016. *ACL Injury and Its Treatment*. *ACL Injury and Its Treatment*. doi:10.1007/978-4-431-55858-3.

Pandey, Pulak M., N. Venkata Reddy, and Sanjay G. Dhande. 2003. “Improvement of Surface Finish by Staircase Machining in Fused Deposition Modeling.” *Journal of Materials Processing Technology* 132 (1–3): 323–31. doi:10.1016/S0924-0136(02)00953-6.

Peters, Abby E., Riaz Akhtar, Eithne J. Comerford, and Karl T. Bates. 2018. “Tissue Material Properties and Computational Modelling of the Human Tibiofemoral Joint: A Critical Review.” *PeerJ* 6: e4298. doi:10.7717/peerj.4298.

Prakash, K. Satish, T. Nancharaih, and V. V.Subba Rao. 2018. “Additive Manufacturing Techniques in Manufacturing -An Overview.” *Materials Today: Proceedings* 5 (2): 3873–82. doi:10.1016/j.matpr.2017.11.642.

Reiner, Tim, Nathan Carr, Radomír Měch, Ondřej Šťava, Carsten Dachsbacher, and Gavin Miller. 2014. “Dual-Color Mixing for Fused Deposition Modeling Printers.” *Computer Graphics Forum* 33 (2): 479–86. doi:10.1111/cgf.12319.

RepRap contributors, "RepRap," *RepRap.org*, Accessed November 18, 2018. https://reprap.org/mediawiki/index.php?title=RepRap&oldid=182586 (accessed November 19, 2018)

Reszka, Alfred A. 2010. “Bisphosphonate Mechanisms of Action.” In *Contemporary Endocrinology: Osteoporosis: Pathophysiology and Clinical Management*, edited by Robert A. Adler, 443–68. Humana Press. doi:10.1007/978-1-59745-459-9.

Rocha, Carmen R, Angel R Torrado Perez, and David a Roberson. 2014. “Novel ABS-Based Binary and Ternary Polymer Blends for Material Extrusion 3D Printing.” *J. Mater. Res.* 29 (17): 1859–66. doi:10.1557/jmr.2014.158.

Sartori, Massimo, Monica Reggiani, Dario Farina, and David G. Lloyd. 2012. “EMG-Driven Forward-Dynamic Estimation of Muscle Force and Joint Moment about Multiple Degrees of Freedom in the Human Lower Extremity.” *PLoS ONE* 7 (12). doi:10.1371/journal.pone.0052618.

Sharkey, Neil A., Tait S. Smith, and David C. Lundmark. 1995. “Freeze Clamping Musculo-Tendinous Junctions for in Vitro Simulation of Joint Mechanics.” *Journal of Biomechanics* 28 (5): 631–35. doi:10.1016/0021-9290(94)00100-I.

Sitthi-amorn, Pitchaya, Justin Lan, and Wenshou Wang. 2015. “MultiFab : A Machine Vision Assisted Platform for Multi-Material 3D Printing.” *ACM Transactions on Graphics*, no. 34: 11. doi:10.1145/2766962.

Song, Haichuan, and Sylvain Lefebvre. 2017. “Colored Fused Filament Fabrication.” http://arxiv.org/abs/1709.09689.

Sophia Fox, Alice J, Asheesh Bedi, and Scott A Rodeo. 2009. “The Basic Science of Articular Cartilage: Structure, Composition, and Function.” *Sports Health* 1 (6): 461–68. doi:10.1177/1941738109350438.

Stiles, Victoria H., Igor N. Guisasola, Iain T. James, and Sharon J. Dixon. 2011. “Biomechanical Response to Changes in Natural Turf during Running and Turning.” *Journal of Applied Biomechanics* 27 (1): 54–63.

Suri, Pradeep, David C Morgenroth, C Kent Kwoh, Jonathan F Bean, Leonid Kalichman, and David J Hunter. 2010. “Low Back Pain and Other Musculoskeletal Pain Comorbidities in

Individuals with Symptomatic Osteoarthritis of the Knee: Data from the Osteoarthritis Initiative." *Arthritis Care & Research* 62 (12): 1715–23. doi:10.1002/acr.20324.

Takeda, Yoshitsugu, John W. Xerogeanes, Glen A. Livesay, Freddie H. Fu, and Savio L.Y. Woo. 1994. "Biomechanical Function of the Human Anterior Cruciate Ligament." *Arthroscopy* 10 (2): 140–47. doi:10.1016/S0749-8063(05)80081-7.

Taubert, Pia. 2012. "Continuously-Variable Material Properties in RepRap 3D Printing." University of Bath. http://reprap.org/mediawiki/images/a/a5/Pia-taubert-material-mixing-report.pdf.

Taylor, K. A., H. C. Cutcliffe, R. M. Queen, G. M. Utturkar, C. E. Spritzer, W. E. Garrett, and L. E. DeFrate. 2013. "In Vivo Measurement of ACL Length and Relative Strain during Walking." *Journal of Biomechanics* 46 (3). Elsevier: 478–83. doi:10.1016/j.jbiomech.2012.10.031.

Taylor, S. J G, P. S. Walker, J. S. Perry, S. R. Cannon, and R. Woledge. 1998. "The Forces in the Distal Femur and the Knee during Walking and Other Activities Measured by Telemetry." *Journal of Arthroplasty* 13 (4): 428–35. doi:10.1016/S0883-5403(98)90009-2.

Torrado, Angel R., and David A. Roberson. 2016. "Failure Analysis and Anisotropy Evaluation of 3D-Printed Tensile Test Specimens of Different Geometries and Print Raster Patterns." *Journal of Failure Analysis and Prevention* 16 (1). Springer US: 154–64. doi:10.1007/s11668-016-0067-4.

Torrado Perez, Angel R., "Defeating anisotropy in material extrusion 3D printing via materials development." PhD diss., The University of Texas at El Paso, 2015.

Torrado Perez, Angel R., David A. Roberson, and Ryan B. Wicker. 2014. "Fracture Surface Analysis of 3D-Printed Tensile Specimens of Novel ABS-Based Materials." *Journal of Failure Analysis and Prevention* 14 (3): 343–53. doi:10.1007/s11668-014-9803-9.

Tsouknidas, A., M. Pantazopoulos, I. Katsoulis, D. Fasnakis, S. Maropoulos, and N. Michailidis. 2016. "Impact Absorption Capacity of 3D-Printed Components Fabricated by Fused Deposition Modelling." *Materials and Design* 102. Elsevier Ltd: 41–44. doi:10.1016/j.matdes.2016.03.154.

Vedi, V, a Williams, S J Tennant, E Spouse, D M Hunt, and W M Gedroyc. 1999. "Meniscal Movement. An in-Vivo Study Using Dynamic MRI." *The Journal of Bone and Joint Surgery. British Volume* 81 (1): 37–41. doi:10.1302/0301-620X.81B1.8928.

Wang, Li I. 2011. "The Lower Extremity Biomechanics of Single- and Double-Leg Stop-Jump Tasks." *Journal of Sports Science and Medicine* 10 (1): 151–56.

Webb, Joshua D, Silvia S Blemker, and Scott L Delp. 2014. "3D Finite Element Models of Shoulder Muscles for Computing Lines of Actions and Moment Arms." *Computer Methods in Biomechanics and Biomedical Engineering* 17 (8): 829–37. doi:10.1080/10255842.2012.719605.

Werner, Frederick W., David C. Ayers, Lorin P. Maletsky, and Paul J. Rullkoetter. 2005. "The Effect of Valgus/Varus Malalignment on Load Distribution in Total Knee

Replacements." *Journal of Biomechanics* 38 (2): 349–55. doi:10.1016/j.jbiomech.2004.02.024.

Wilson, Stephen P. "A methodology for physically-based contact and meniscus properties in rigid-body computational knee modeling." Master's thesis, The University of Texas at El Paso, 2015.

Woo, S L, J M Hollis, D J Adams, R M Lyon, and S Takai. 1991. "Tensile Properties of the Human Femur-Anterior Cruciate Ligament-Tibia Complex. The Effects of Specimen Age and Orientation." *The American Journal of Sports Medicine* 19 (July): 217–25. doi:10.1177/036354659101900303.

Woo, Savio L-Y, and Matthew B Fisher. 2009. "Evaluation of Knee Stability with Use of a Robotic System." *The Journal of Bone and Joint Surgery. American Volume* 91 Suppl 1: 78–84. doi:10.2106/JBJS.H.01371.

Woo, Savio L Y, Steven D. Abramowitch, Robert Kilger, and Rui Liang. 2006. "Biomechanics of Knee Ligaments: Injury, Healing, and Repair." *Journal of Biomechanics* 39 (1): 1–20. doi:10.1016/j.jbiomech.2004.10.025.

Wünschel, Markus, Ulf Leichtle, Christian Obloh, Nikolaus Wülker, and Otto Müller. 2011. "The Effect of Different Quadriceps Loading Patterns on Tibiofemoral Joint Kinematics and Patellofemoral Contact Pressure during Simulated Partial Weight-Bearing Knee Flexion." *Knee Surgery, Sports Traumatology, Arthroscopy* 19 (7): 1099–1106. doi:10.1007/s00167-010-1359-y.

Xia, Zihui, Mohammad Al Amin Khan Chowdhuri, and Feng Ju. 2013. "A New Test Method for the Measurement of Normal-Shear Bonding Strength at Bi-Material Interface." *Mechanics of Advanced Materials and Structures* 20 (7): 571–79. doi:10.1080/15376494.2011.643278.

Zhang, Binbin, Prakhar Jaiswal, Rahul Rai, and Saigopal Nelaturi. 2016. "Additive Manufacturing of Functionally Graded Objects: A Review." *Volume 1A: 36th Computers and Information in Engineering Conference* 18 (December): V01AT02A045. doi:10.1115/DETC2016-60320.

Vita

Joshua Taylor Green was born August 10, 1987 in Las Vegas, Nevada to Donald Wayne Green and Pamela Grace Green. Following graduation from Mountain View Christian School, he enrolled at LeTourneau University where he received a Bachelor of Science in Engineering with a Mechanical concentration in 2009. During his time spent at LeTourneau University, he led a variety of engineering projects including a human-powered water-distilling machine, a wind-powered walking machine, and an *in vitro* knee load simulator. After working at LeTourneau University as an engineering consultant for the summer of 2009, he moved back to Las Vegas, Nevada where he was employed by Harris Consulting Engineers LLC as a mechanical designer. In 2012, he enrolled in the Materials Science and Engineering doctoral program at The University of Texas at El Paso. At UTEP, he helped start the Joint Lab where he led development of The University of Texas at El Paso Joint Load Simulator, a fused filament fabrication printer for local composition control, and methodology for synthetic tissue development.

Contact Information: joshtgreen@gmail.com

This thesis/dissertation was typed by Joshua Taylor Green.